Università Politecnica delle Marche
Scuola di Dottorato di Ricerca in Scienze dell'Ingegneria
Curriculum Meccanica

Inspection and characterization of birefringent materials: development of methods and systems for scintillating anisotropic crystals

Ph.D. Dissertation of:

Luigi Montalto

Advisor:

Prof. Nicola Paone

Curriculum supervisor:

Prof. Daniele Rinaldi

Dr. Paul Lecoq

XV edition - new series

Università Politecnica delle Marche
Dipartimento di Ingegneria Industriale e Scienze Matematiche
Via Brecce Bianche — 60131 - Ancona, Italy

Abstract

A scintillating material has the peculiar capability to convert in visible light the energy of a radiating particle that interact within its volume.
The excitation can derive from different kinds of radioactivity or energy interaction that is able to excite electrons so to make them jump to a higher energy band and turn back to their equilibrium state. This mechanism leads to a release of photons in the visible (or near-visible) range.
The light produced by the scintillating material is usually monochromatic and represents the output of the conversion of the incident energy in the energy of a group of photons each of much lower energy than one absorbed, as it happens for all kinds of energy conversion.
The quality of light emitted by these materials has, also, great quality in terms of wavelength stability, coherence and polarization.
They are involved in fields like the nuclear and high energy physics (for instance, CERN-Geneva), medical and general bio-imaging (PET-positron emission tomography for cancer diagnosis), geologic research, security and laser technology.
Performances of the scintillators rule the behavior of the instruments and the systems exploited in those fields; moreover, the quality of the material itself and the production efficiency, determine the cost and the feasibility of the above-mentioned activities.
In depth knowledge and characterization of the material is crucial to predict the behavior of the crystals from mechanical and optical viewpoint. Since the production process is quite complex, delicate and time consuming, industry needs tools to improve the efficiency and efficacy of the larger and larger production of these crystalline scintillators
The work presented in this thesis aims to the development of non-invasive methods and systems to assess the crystal quality through the determination of the residual stress state that can be the signature of the whole quality degradation due to different origins.
The developed methods are based on photoelasticity and optical crystallography; they allow to a very detailed analysis providing sensitivity and spatial resolution.
The possibility to have a complete characterization of the materials has been improved by the measuring in different direction with respect to the crystal optic axes.
The set of developed methods is completed by a new technique named Sphenoscopy, which provides reliable inspection of the crystal in a faster and simplified way whatever orientation of the crystallographic and optic axes.
Since they are based on the acquisition of fringe images, -the systems have been provided of dedicated algorithms to process and analyze accurately the fringe patterns carried out by the methods.
The information carried out by these methods are useful for both research bodies and industries, crystal producers and users, since they are crucial feedbacks to better understand the material behavior, develop predictive math models and set properly the production parameters.

Abstract

Un cristallo scintillatore ha la peculiare capacità di convertire, in luce visibile, l'energia di una particella radiante che interagisce con il suo volume.
L'eccitazione può derivare da diversi tipi di radioattività o interazione energetica che è in grado di eccitare gli elettroni in modo da farli saltare ad una banda di energia più alta e tornare indietro al loro stato di equilibrio. Questo meccanismo porta ad un rilascio di fotoni nel visibile (e vicino visibile).
La luce prodotta dal cristallo è solitamente monocromatica e rappresenta il prodotto della conversione dell'energia incidente in energia di un gruppo di fotoni di energia molto inferiore quelli assorbiti, come avviene per tutti i tipi di conversione di energia.
La qualità della luce emessa da questi materiali, in termini di stabilità di lunghezza d'onda, coerenza e polarizzazione, è estremamente elevata.
Essi sono coinvolti in campi come la fisica nucleare e la fisica delle alte energie (ad esempio, CERN-Ginevra), in campo medico nell'ambito del bio-immaging (tomografia ad emissione di positroni PET-per la diagnosi del cancro), la ricerca geologica, la sicurezza e la tecnologia laser.
Le prestazioni degli scintillatori incide sul comportamento degli strumenti e dei sistemi sfruttati in tali settori; Inoltre, la qualità del materiale stesso e l'efficienza di produzione, determinano il costo e la fattibilità delle suddette attività.
Una conoscenza approfondita e una buona caratterizzazione del materiale è fondamentale per prevedere il comportamento dei cristalli dal punto di vista sia meccanico che ottico. Poiché il processo di produzione è piuttosto complesso, delicato e lungo, l'industria ha bisogno di strumenti per migliorare l'efficienza e l'efficacia della produzione di questi scintillatori cristallini
Il lavoro presentato in questa tesi mira allo sviluppo di metodi e sistemi non invasivi per valutare la qualità dei cristalli attraverso la determinazione dello stato di stress residuo, che può essere una firma del grado di qualità.
I metodi sviluppati sono basati sulla fotoelasticità e la cristallografia ottica; permettono un'analisi molto dettagliata con elevata sensibilità e risoluzione spaziale.
La possibilità di avere una caratterizzazione completa dei materiali è stata migliorata riuscendo a misurare in direzione diversa rispetto agli assi ottici del cristallo.
L'insieme di metodi sviluppati è completata da una nuova tecnica denominata Sfenoscopia, che fornisce controlli affidabili del cristallo in un modo più veloce e semplificato ed in qualunque orientamento rispetto agli assi ottici.
Dal momento che i metodi si basano sulla acquisizione di immagini di frange, i sistemi sono stati forniti di algoritmi dedicati per elaborare e analizzare accuratamente le immagini acquisite.
Le informazioni ottenute con questi metodi sono utili sia per gli enti di ricerca che per le industrie, produttori e utenti finali.
Esse sono fondamentali per avere la possibilità di comprendere meglio il comportamento del materiale, sviluppando modelli matematici predittivi, per impostare correttamente i parametri di produzione

Contents

Chapter 1

1 Introduction

A scintillating material has the peculiar capability to convert in visible light the energy of a radiating particle that interact within its volume.
The excitation can derive from different kinds of radioactivity or energy interaction that is able to excite electrons so to make them jump to a higher energy band and turn back to their equilibrium state. This mechanism leads to a release of photons in the visible (or near-visible) range.
Basically, the same phenomenon governs phosphorescence, luminescence and scintillation, differing by the internal mechanisms involved and by their decreasing time scales [1].
Light Yield (LY), rise and decay time (τ), wavelength and energy resolution (ER) are some of the main characteristic parameters of the phenomenon [2].
Briefly: LY is the number of photons (light intensity) produced with respect to the energy interaction, rise time and decay describe the duration of the scintillation phenomenon (the rise of intensity and the decay), ER describe how narrow is the peak in the emission energy spectra (narrower the peak, better the capability to discriminate the incoming energy of the radiation.) [2].
The light produced by the scintillating material represents the output of the conversion of the incident energy in the energy of a group of photons each of much lower energy than one absorbed, as it happens for all kinds of energy conversion.
The quality of light emitted by these materials has, also, great quality in terms of wavelength stability, coherence and polarization.
It is obvious that these objects find place in number of applications as primary transducers of sophisticated and complex systems.
They are involved in fields like the nuclear and high energy physics (for instance, CERN-Geneva), medical and general bio-imaging (PET-positron emission tomography for cancer diagnosis), geologic research, security and laser technology.
Performances of the scintillators rule the behavior of the instruments and the systems exploited in those fields; moreover, the quality of the material itself and the production efficiency, determine the cost and the feasibility of the above-mentioned activities.
Applications, by their growing demand in space and time resolution, light production, sensitivity and general improvement of the quality, prompted the increased performance of the Scintillators.
Synthetic mineral crystalline scintillators still represent the best performing material; therefore, more and more efforts are aimed in this direction.
This generation of materials is characterized by an excellent time resolution, with a steep rise and short persistence (no afterglow) of the luminescence, due to a chemical structure that gives high properties and reliable performance over time and a resistance to working conditions (no aging, radiation resistance) [3]. By choosing high atomic number, Z, chemicals, high density crystals can be synthesized, ensuring the tight containment of deposited energy -thus reducing the instrument dimensions [2].
In depth knowledge and characterization of the material is crucial to predict the behavior of the crystals from mechanical and optical viewpoint. Since the production process is quite complex, delicate and time consuming, industry needs tools to improve the efficiency and efficacy of the larger and larger production of these crystalline scintillators [4].
The work presented in this thesis aims to the development of non-invasive methods and systems to assess the crystal quality through the determination of the residual stress state that can be the signature of the whole quality degradation due to different origins.

The information carried out by these methods are useful for both research bodies and industries, crystal producers and users, since they are crucial feedbacks to better understand the material behavior, developing predictive math models, and to set properly the production parameters.
The conceptual process will be presented starting from the state of the art which is the base of the developed methods, with a dedicated section about the impact of this research.
Hereafter, some paragraphs will outline briefly the main fields in which scintillating crystals are involved, their principal production techniques and criticalities.

1.1 Context of the research activity

1.1.1 Outline of the main production procedures

Scintillating crystal production evolves from the chemical laboratory to the industrial scale. Crystals are produced by growth methods specific (optimal) for every chemical compound, part size and quantity [1].
A variety of techniques is used to grow scintillating inorganic crystals. They are all derived
by two main methods, which are named Czochralsky and Bridgman [5].
Upstream, the preparation of raw materials is a mandatory prerequisite for crystal quality. Purity must be controlled, affecting scintillation (afterglow, light yield) transparency (color centers) radiation resistance and built-in stress level (cell distortion).
Dopant species and quantity are responsible for the lightning performances and production. The dopant fraction is usually of a few percent. They should be chosen to match the lattice properties to the best (crystal symmetry, lattice parameters). Two obstacles must be faced: segregation, that makes light production uneven over the crystal volume, and lattice distortion, that may induce mechanical stress and be detrimental to the production yield.

1.1.1.1 Czochralsky method

In Czochralsky method (Fig. 1.1), raw materials are molten in a metallic crucible and kept slightly above fusion point. A small crystal of the same material (seed) is put in contact with that molten bath and pulled up to lift a small meniscus of liquid by capillarity. Solidification occurs at a position and at a rate ruled by several parameters [6].

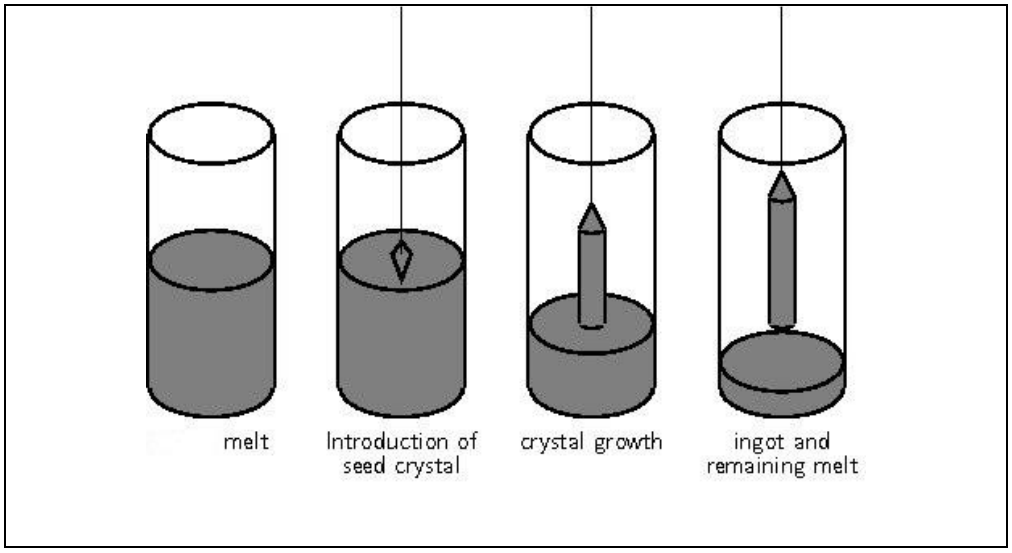

Fig. 1. 1 A schematic representation of the Czochraski growth method; a hot melt of raw material is put in contact with a pure crystalline seed (slightly colder), generating a meniscus where the melt starts to solidify. Then the growth crystalline part is pulled up (or down) slowly so to produce the boule.

The thermal gradient is regulated by an induction loop heating the melt with the help of the crucible mass. The melt temperature is homogenized by crucible regulation. The rising solidified bulk takes the shape of the desired ingot (or boule). The pulling rate gives the ingot its conical top and bottom ends and its cylindrical overall shape. Optimal conditions result in turning the full melt into the ingot volume. The growth of a 1kg PWO ingot take a time of the order of 1 day. The ingot shape may be facetted or oval, depending on the crystal lattice and on the seed orientation. The latter is a critical parameter.

1.1.1.2 Bridgman method

A scheme is presented in (Fig. 1.2a). This method is an evolution of the fusion zone refining method [6]; the hot zone moves along the length of the furnace while the crystal growths. The raw (in powder form) material is shaped to the final part proportions with extra thickness for the mechanical processing to follow. The shape is usually an elongated prism (Fig. 1.2b). A monocrystalline seed is placed at one end. This assembly is contained in a thin (a few tenths of a mm) metallic envelope, usually made of platinum.

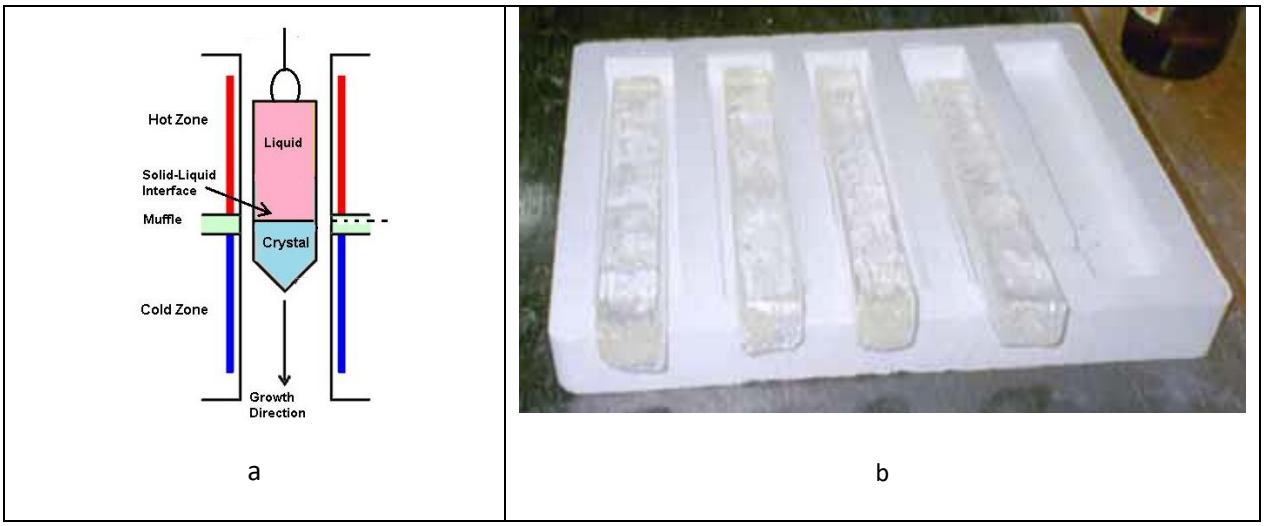

Fig. 1. 2 A scheme of a possible Bridgman setup (left). In this case, it is the heater that moves along the crucible length. The seed is placed at a side of the crucible and the powder of raw material first melts and then crystallizes while the heater goes back and forth several times. The technique allows to prepare a multiple crucible shaped more or less like the requested final geometry.

One or several of these assemblies are positioned in the furnace enclosure. The fusion zone (thermal gradient) moves from the seed interface along the ingot length by combining several induction loops. The gradient displacement velocity is comparable to the Czochralsky growth rate, but the operation must be repeated several times (at the week scale) to reach monocrystallinity and purity at the required level. The Bridgman process competes with the Czochralsky method only using multiple ingot furnaces, so to have a parallel production.

1.1.1.3 Annealing

The solidification process results in thermally-induced stresses. They are supposed to have the conventional parabolic profile, with moderate compression in the core, and higher tension at the periphery. The latter is a matter of concern as crystals are especially prone to breaking in tension (crack opening). Annealing is necessary to reduce these tensions. The annealing temperature is very close to the melting point to ease dislocation movements and elimination. The thermal effect is sometimes combined with the presence of a chemical element in a controlled atmosphere, as a chemical correction is expected to restore the crystal lattice equilibrium. In that case, annealing time is governed by diffusion and may take several days.

The annealing furnace is therefore a complex temperature controlled device and annealing is a costly operation in time and money.

Moreover, the annealing step is performed to recover the radiation damage too; since in this process the thermal time gradient could be faster, the distribution of the eventual residual stress can be critical.

1.1.1.4 Machining

Cut and shape the crystals according to the needs is a delicate part. This is a key activity to avoid material wasting or induce stress and bad surface condition. Ingots are the base material for expensive parts tightly specified in shape and dimensions. Mechanical processing is designed to achieve these two goals.

1) For calorimeters, ingots are usually dimensioned for the yield of one piece. Attempts were made to get two and even four pieces out of an ingot.

2) The tiny pixels for medical imaging are either obtained by the many from a single ingot, or cut from fibers.

1.1.2 A touch upon the main fields of applications

Two of the main fields are briefly reported; nuclear and high energy physics and medical imaging. The basic principles are described outlining the criticalities.

1.1.2.1 Nuclear and high energy Physics

Scintillating crystals, in the High-Energy Physics, are used to build calorimeters (Fig. 1.3) with the scope of measuring the effect of elementary particles generated during particle (e.g. electrons) collisions in accelerators.
The spatial energy distribution (intensity, frequency) due to collisions allows physicists to detect the kind of generated particles, the decay time and many others information.

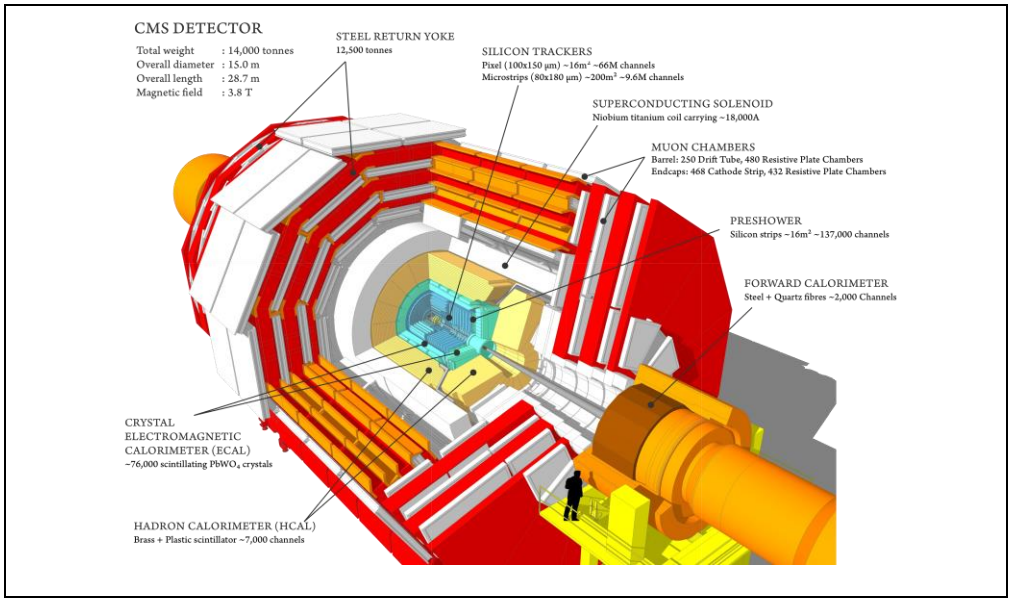

Fig. 1. 3 The huge dimensions of the CMS detector are shown in this figure. It is possible to note them with respect to the human height (in black). About 80000 PWO crystals are mounted into the device, coupled with sophisticated photodetectors [7] and electronics.

About 80000 large sized Yttrium doped PWO ($PbWO_4$) crystals are installed on the CMS calorimeter [7].
The extreme speed of response, together with specific spectral sensitivity, high light yield and good radiation absorption capacity are the discriminating parameters for the choice. The critical working environment requires highly performing and quality crystals. In fact, the high radiation rate and the heavy radiating particles (e.g. hadrons) could degrade the scintillation efficiency, radiation hardness [3] is therefore one of the main characteristic to consider.
High density is mandatory to increase the stopping power [2], ensuring the capability to stop high energized particles.
In this case, PWO crystals have a low light yield [3], therefore light extraction became crucial to the good behavior of the CMS system; crystal geometry and homogeneity of the refractive indices need attention too.
The large size required for these dense and brittle material poses some issues for the production and the behavior during function.

Increasing size means a much more complex thermal and motion control during the growth and could heighten the development of a thermal residual stress distribution. This is a crucial problem during the cutting and assembly of the crystals; the risk of unwanted fractures during function, due to thermal shock (due to the light production mechanism or during the annealing process used to recover from the radiation damage) or the instauration of non-predicted stress in the CMS modules, is linked to that stress condition.
Finally, the stress could dramatically change the distribution of the refractive indices, influencing the light extraction.

1.1.2.2 Medical bio-imaging (PET/SPECT)

The knowledge of elementary particles allowed, in the last decades, the development of technological devices for Medical diagnosis based on the detection of high energy photons. One of the most promising techniques in the field of cancer diagnosis and cerebral activity monitoring is the Positron Emission Tomography (Fig. 1.4).

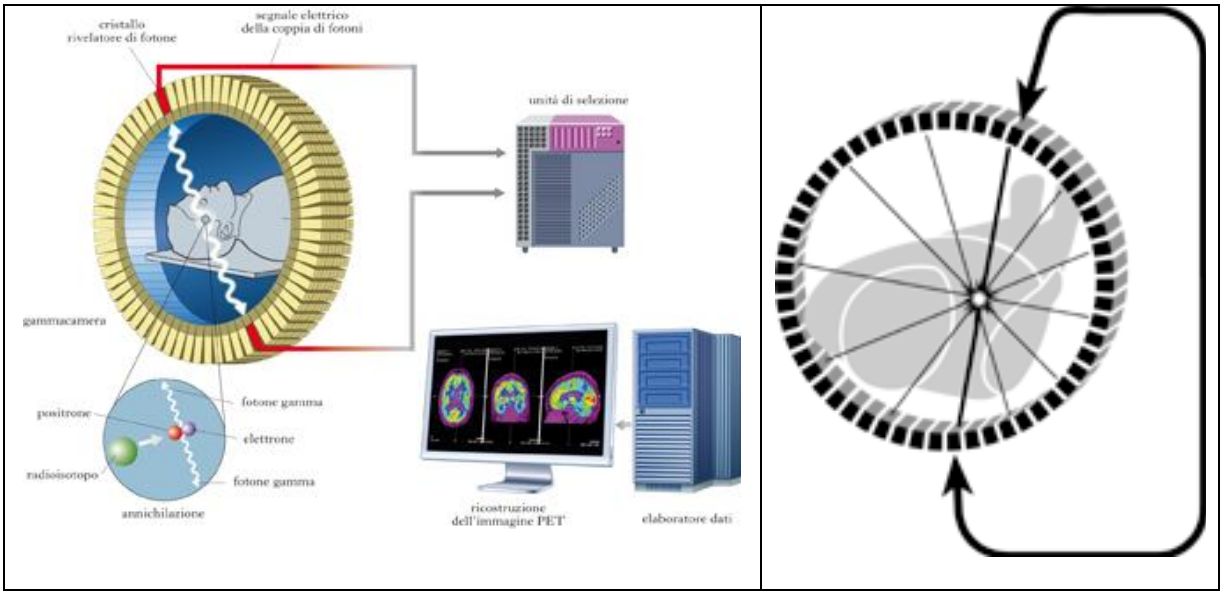

Fig. 1. 4 A scheme of a PET behavior, the back to back emitted gamma rays are detected by the scintillators placed on a ring. If the crystals have a good quality and a fast response (fast decay time) the emission point can be evaluated along the line by the measure of the time of flight. Otherwise more statistics and a higher computational effort is needed, resulting in a longer persistence of the patience exposition.

In PET the patient ingests some radio-element that releases positrons (beta decay). The recombination of the positron with an ambient electron produces two opposite gamma rays of well-defined energy (511 keV) detected in opposite scintillator pixels (usually 2 x 2 x 10 mm^3 prisms) [8].
Modern devices aim to be characterized by lower radiation doses (and/or shorter exposures), 3-D information (tomography), real-time observation, tissue or function identification, with the help of large arrays of fine scintillators (pixels) surrounding the patient or covering the organ (mammography) and powerful reconstruction software [9].
Even if the architecture and the principle of detection is similar to the calorimeters, the different scope and dimensions require special characteristics of the scintillators.
Small pixeled crystals are mandatory, with a high light yield to have the necessary spatial resolution.

Also, a good energy resolution (a well-defined peak of emission) to increase the sensitivity is needed. A fast response with a short decay time is needed to achieve a time of flight PET analysis (TOF-PET), crucial for a shorter exposure of the patient and a real-time diagnosis.
Each PET is provided of about 20000 crystals. Aging and stability of the scintillators are crucial for the behavior of this complex medical tool. Growth and machining are critical as well as the homogenous distribution of the dopants (performance decrement and lattice distortion can derive from an incorrect distribution).
Stress and distortion affect dramatically the functional properties and the production efficiency. The induced change of the refractive indices affect the light transport and extraction; a low residual stress state makes the machining and polishing more efficient. The capability to endure to eventual shocks is improved controlling the stress state, so to achieve a slow aging.
SPECT [10] (single photon emission computed tomography, namely Positron emission single photon), is another diagnostic technique very similar to PET [10]. It is largely used for the diagnosis of diseases of brain and neuroendocrine system. SPECT differs from PET by the use of radioactive compounds that directly emit gamma rays.
An example is the use of the isomer ^{99m}Tc, which decaying emits a single photon; this has a peak around 140 keV and the half-life of 6 hours. The SPECT technology is, usually, less expensive than the PET and the exposition is typically short (15-20 seconds each image acquisition). It offers the possibility to visualize the hematic flow for a long time.
After the injection of the radioactive substance, a gamma camera (Fig. 5) acquires planar images at several angles around the phantom or the patient. By these, a 3D reconstruction of the images is achieved. The main elements which compose the gamma camera are (Fig. 1.5):

1. The collimator: a lead plate with holes which allow gamma rays in a particular direction; it is used to manage the magnification and the field of view.
2. Pixelated scintillating crystals, used to convert the gamma photon in light signals.
3. Photodetectors
4. Computing system

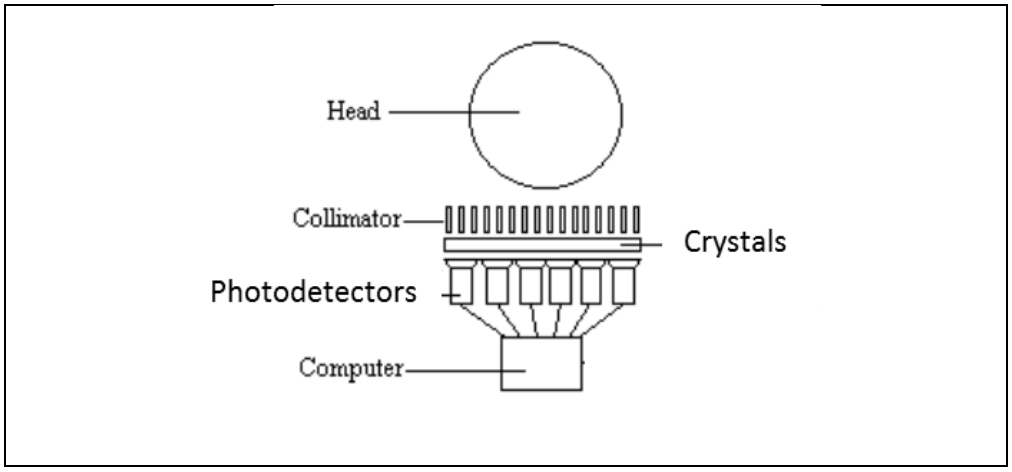

Fig. 1. 5 A scheme of a gamma camera. The collimater allows gamma rays, coming from the phantom (head), which have a particular direction, the pixelated crystals convert the gamma rays in light detected by the photodetectors which produce electric signals analyzed by the computer.

The quality of the pixelated crystals rules the entire behavior of the device. To achieve spatially resolved images, they are machined in very small pixels; it is, therefore, fundamental check their condition, since this affects the performances in terms of sensitivity, energy resolution and light collection, influencing the quality of the signal.

1.2 Scope of this work

In the previous paragraphs, the production processes and some of the main applications which involve scintillating crystals have been briefly outlined with their own characteristics and criticalities. The crystals functional behavior and service life are related to their quality; their internal structure and mechanical stress may affect negatively performance and lifetime.
Unwanted or unpredict failure during production or during function are linked to the mechanical stress conditions that is relate to the whole crystal quality.
Stress and structure distortion may affect the lightning phenomena so to lead to an out of design performances with unpredictable and non-repeatable behavior.
A deeper knowledge of the opto-mechanical behavior and the assessment of the crystal condition, are mandatory to overcome the above-mentioned issues.

This work deals with the development of method and systems to characterize and evaluate the condition of birefringent crystals by means of the assessment of the residual stress state [11].
Residual stress is a good indicator of the crystal quality, since it affects the crystals from the production to the function.
The developed methods are aimed to achieve:

- A safe check of the samples state, since crystal are expensive and delicate
- An efficient quality control systems and useful feedbacks for the production process.
- Reliable tools to develop predictive models of the opto-mechanical behavior.

Therefore, methods which can have a transversal exploitation, from research to the industries and users, have been developed.
To be suitable for the purpose, non-invasive techniques have been developed and optimized.
Since scintillating crystals are mostly naturally birefringent and transparent materials, photoelastic methods [12] and optical crystallography [13][14] techniques are suitable bases for the work. Moreover, they allow to develop non-destructive testing methods, which are relevant for process and quality control of crystal production.
In fact, these methods have been adapted and optimized for the purpose of scintillating crystal inspection.

1.3 State of the Art. A brief survey

Scintillating materials are transparent and usually are optically anisotropic. Internal stress causes lattice strain and deformations, which manifest as stress induced birefringence [12]; this means that the distribution of the refractive indices varies as a function of stress. The piezo-optic properties of the material can be observed to verify its internal strain (or stress) state.
Photoelasticity is a classical measurement technique suited to observe stress induced birefringence in transparent materials, classically used for isotropic materials [11].
Fringe pattern is observed in isotropic materials due to the stress state distribution (Fig. 1.6).

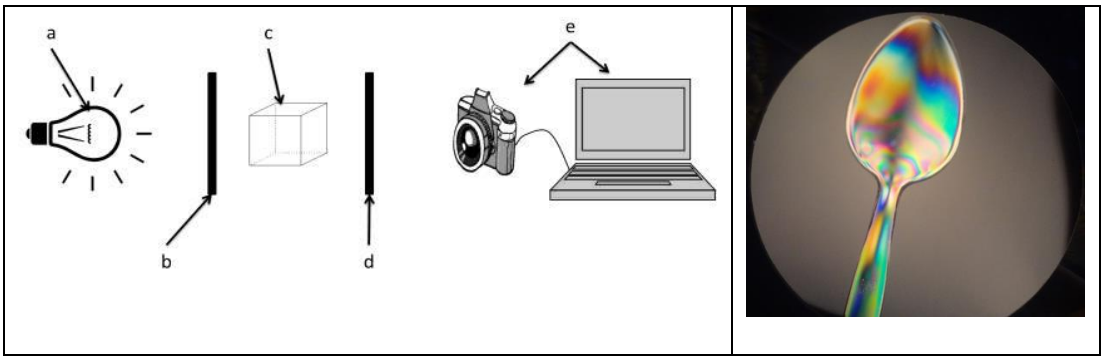

Fig. 1. 6 On the left a scheme of a polariscope set-up: a) the diffuse light source, b) and d) the crossed polarizers (d is usually called analyzer), c) the sample, e) acquisition system. On the right the typical fringe pattern due to a residual stress condition in an isotropic material.

Therefore, photoelasticity is a suitable and non-invasive method for quality control of scintillating crystals. This measurement method, implemented by observation in polarized light (polariscopes), provides information on crystal quality, related to mechanical strain and stress, and requires an accurate knowledge of piezo-optic properties of the material [14][15], which are not always available. Furthermore, it is a volumetric technique which provides information on the spatial integral of the stress distribution along the light path through the crystal.

The optical properties of transparent naturally birefringent materials are often observed and evaluated by means of conoscopy [13]. Observation made by converging or diverging polarized light (conoscopy) in transmission through an optically transparent crystal allows to observe interference fringes, which provide information about the structural and elasto-optic properties of the material. Qualitative and quantitative information about external influences, such as temperature, stress, electric, and magnetic fields, on optical characteristics could be extracted through the conoscopic observations [16].

Conoscopy is well known in both mineralogy and optical crystallography [17] where the method is usually implemented by means of the polarized microscopes to determine the species and the characteristics of the crystal mineral. The method is also used to evaluate the light characteristics like polarization (e.g. in [18])

The technique, generally used for naturally birefringent materials, produces fringe patterns that are a signature of the crystal structure even if stress is not present (Fig. 1.7).

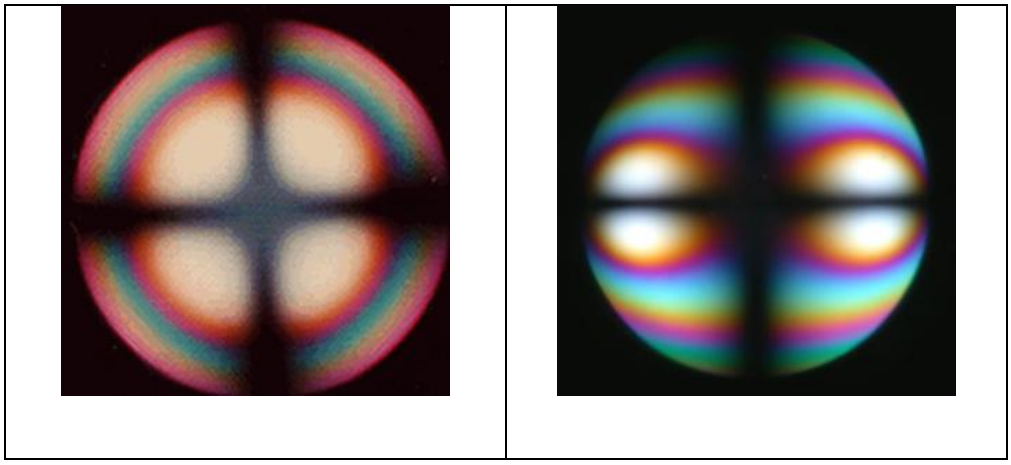

Fig. 1. 7 Fringe patterns carried out by means of polarized microscopes in conoscopy configuration (diverging light) observing anisotropic media. The shape is a signature of the crystal symmetry: uniaxial crystal on the left and biaxial on the right.

Photoelasticity and optical crystallography, by means of Conoscopy, are at the bases of this research activity in conjunction with image processing and analysis techniques [19]. In fact, an efficient data process is mandatory to obtain reliable fringe pattern images.

Actually, the use of the classical diffuse light polariscope applying conoscopic observation is the state of the art for non-invasive analysis of the crystal state. How it will be outlined in chapter 3, these systems are reliable and capable to evaluate the crystal condition, allowing to assess the correspondence between interference fringe pattern shape and stress level [20]. They are not affected by environmental condition and external influences like vibrations, temperature and crystal surface quality. Anyway, the classical polariscope based methods present limitation in terms of sensitivity, spatial resolution and precision.

Chapter 2

2 Crystal Optics

Scintillating Crystals are optically transparent, therefore photoelastic methods; in transmitted light, are natural candidate to build up a non-invasive technique to check the crystal conditions and characterize them.
The behavior of the light transmitted through the medium depends by its optical characteristics linked to the refractive indices distribution [13].
One example of the interaction between light and matter is the well-known Snell law [17].
The refractive index distribution along the optical path of a light beam will affect the electromagnetic wave (light) with respect to its wavelength (λ), polarization (direction of the vibration of the electric field) and direction of propagation [14].
The photoelastic phenomena treated in this work are therefore linked to how the light propagates into the media rather than the interaction at the interface of two different media.
In this chapter, it will be briefly shown the difference between isotropic media and anisotropic ones (naturally birefringent crystals) considered in this work.
At the base of the treatment there is the wave theory of light (light wave), therefore, some about light wave and polarization will be briefly outlined hereafter.

2.1 *Light and Polarization*

The wave model describes the light as a composition of electric E and magnetic H field which are in phase each other and that oscillate perpendicularly to each other (Fig. 2.1a). The wavelength λ and the frequency f are connected each other by the law:

$$\lambda \cdot f = c \qquad \text{(eq. 2.1)}$$

Where c is the speed of light. The light waves can propagate in several directions. The loci of points where at the same time t the electric fields vibrate in the same way (they have the same phase) is defined as *wave front.* The shape of the wave front can be geometrically regular (sphere, plane) or completely random (Fig. 2.1b).

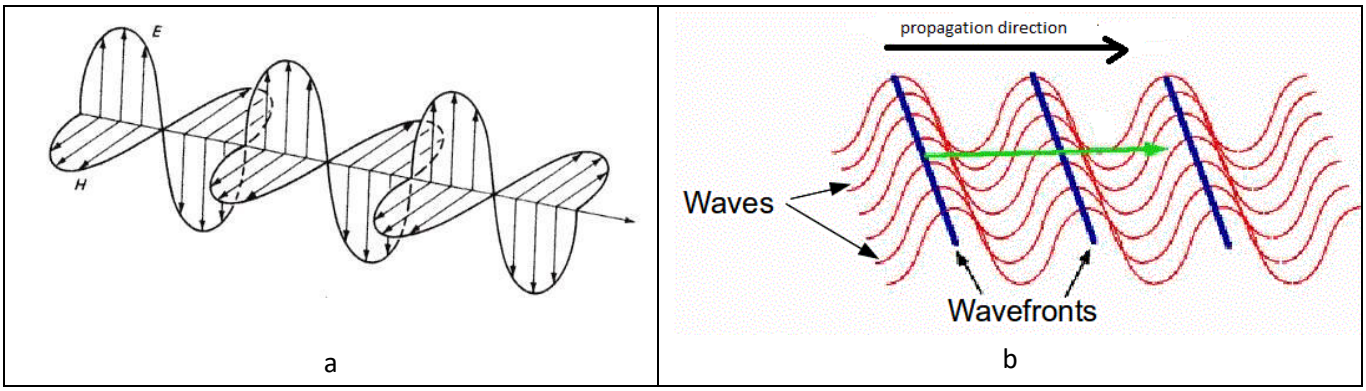

Fig. 2. 1- Electromagnetic wave representation (a) as the oscillation of E, electric field, and H, magnetic field, in phase and mutually orthogonal. (b) representation of the wavefront in a coherent propagation of light waves.

Maxwell equations in vacuum describe wave propagation. These equations connect the spatial E and H variations to their temporal variations [21].

$$\nabla^2 \mathbf{E} = \mu_0 \varepsilon_0 \frac{\partial^2 \mathbf{E}}{\partial t^2} \qquad \text{(eq.2.2)}$$

$$\nabla^2 \mathbf{H} = \mu_0 \varepsilon_0 \frac{\partial^2 \mathbf{H}}{\partial t^2} \qquad \text{(eq. 2.3)}$$

Where:

- μ= magnetic permeability [17];
- ε = dielectric constant [17];

To describe an optical wave just the E vector is considered. The electric field function that satisfy the equation (2.2) is:

$E = E_0 \, e^{i(kr - \omega t)}$ (eq. 2.4)

In which:

- E_0 = vector amplitude;
- k = wave vector with the amplitude $2\pi/\lambda$ and parallel to the propagation direction;
- r = displacement vector;
- ω = angular frequency = $2\pi f$.

In the case of a plane wave front wave which propagates in the z direction it is possible to write the function:

$$E = E_0 \cos\frac{2\pi}{\lambda}(z - ct) \qquad \text{(eq. 2.5)}$$

In the image (Fig 2.2) are represented waves with different phase delay δ.

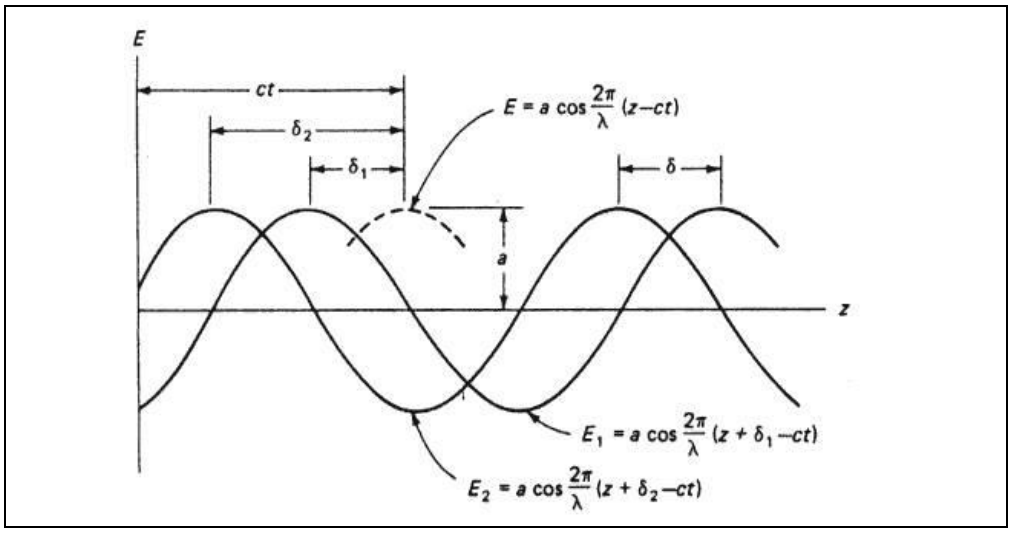

Fig. 2. 2 representation of waves with the same characteristics in terms of λ, amplitude and ω (2πc/λ) but with different delay δ.

The waves in Fig. 2.2 can be described by the functions [17]:

$$E = E_0 \cos\frac{2\pi}{\lambda}(z - ct) \qquad \text{(eq. 2.6)}$$

$$E_1 = E_0 \cos\frac{2\pi}{\lambda}(z + \delta_1 - ct) \qquad \text{(eq. 2.7)}$$

$$E_2 = E_0 \cos\frac{2\pi}{\lambda}(z + \delta_2 - ct) \qquad \text{(eq. 2.8)}$$

A comfortable representation is achieved if the following assumptions are made:

Let's define the phase delay as

$$\delta = \delta_2 - \delta_1 \qquad \text{(eq. 2.9)}$$

And the phase angle as

$$\phi = (z + \delta)\frac{2\pi}{\lambda} \qquad \text{(eq. 2.10)}$$

The three equation can be written as:

$$E = E_0 \cos(\phi - \omega t) \qquad \text{(eq.2.11)}$$

$$E_1 = E_0 \cos(\phi_1 - \omega t) \quad \text{(eq.2.12)}$$

$$E_2 = E_0 \cos(\phi_2 - \omega t) \quad \text{(eq. 2.13)}$$

A wave emission is composed by a series of short impulses and from great number of emitting atoms; each impulse contains a discrete number of oscillations; this is usually called wave train. If the emissions are not coordinate each train will be different to the other in terms of amplitude, phase and vibration plane. That is, the light is not coherent. Otherwise, if the light has a regular wave front and vibrates ordinately then is defined coherent (Fig. 2.1b).
Polarization of light, is about how the light wave vibrates along its propagation path. The harmonic light waves (defined as the oscillation of the Electric Field *E*) can vibrate in a plane, then is linear polarized or plane polarized (Fig. 2.3a) but can also vibrate generating a circular or elliptic helix (circular and elliptic polarization Fig. 2.3b and c), or randomly (unpolarised) like most the light sources.

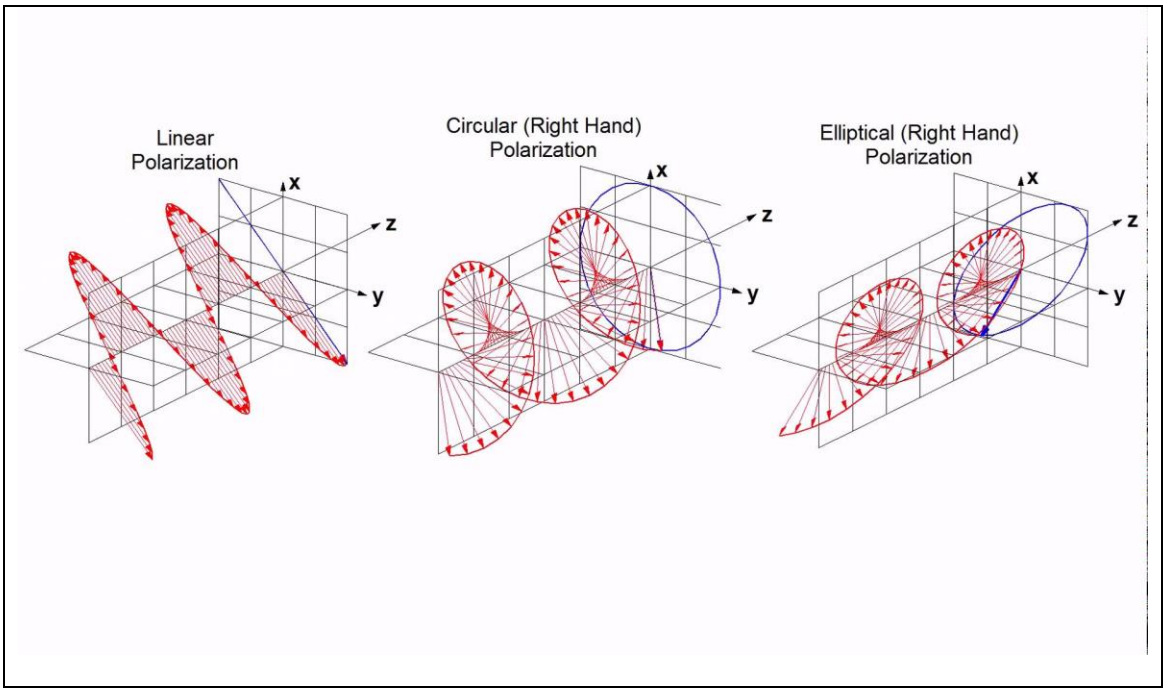

Fig. 2. 3 polarization of the light wave (how the electric field vibrates); linear (a), circular (b) and elliptical (c).

Polarization can result by the composition of the light waves which vibrate in planes mutually orthogonal (Fig. 2.4).

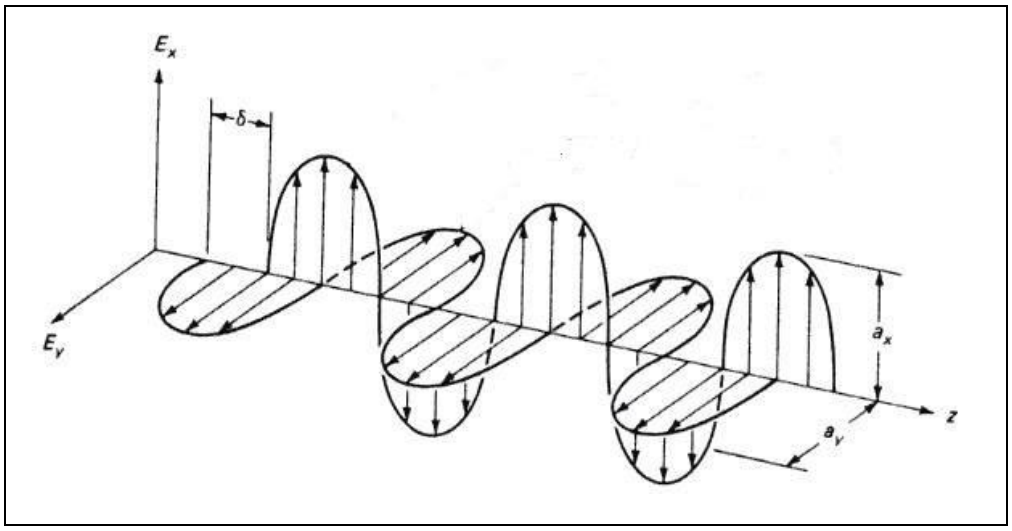

Fig. 2. 4 two identic light waves which vibrate in mutually orthogonal planes. The resulting wave by their composition has a polarization which is a function of the delay and the amplitudes.

Let us consider the waves in Fig. 2.4, they are defined with the harmonic motions:

$$E_x = E_{0x}\cos(\omega t) \qquad \text{(eq. 2.14)}$$

$$E_y = E_{0y}\cos(\phi - \omega t) \qquad \text{(eq. 2.15)}$$

They can be rearranged so to eliminate the time and see what the tip of the resulting vector E describes on the plane orthogonal to the propagation [13].

$$\frac{E_x}{E_{0x}} = \cos(\omega t) \qquad \text{(eq. 2.16)}$$

$$\frac{E_y}{E_{0y}} = \cos(\omega t)\cos(\phi) + \sin(\omega t)\sin(\phi) \qquad \text{(eq. 2.17)}$$

Substituting:

$$\frac{E_y}{E_{0y}} = \frac{E_x}{E_{0x}}\cos(\phi) + \sqrt{1 - \frac{E_x^2}{E_{01}^2}}\sin(\phi) \qquad \text{(eq. 2.18)}$$

Transposing and squaring

$$\left[\frac{E_y}{E_{0y}} - \frac{E_x}{E_{0x}}\cos(\phi)\right]^2 = \left[1 - \frac{E_x^2}{E_{0x}^2}\right]\sin^2(\phi) \qquad \text{(eq. 2.19)}$$

$$\left(\frac{E_y}{E_{0y}}\right)^2+\left(\frac{E_x}{E_{0x}}\right)^2-2\frac{E_yE_x}{E_{0y}E_{0x}}\cos(\phi)=\sin^2(\phi) \qquad \text{(eq. 2.20)}$$

This last equation represents an ellipse in the plane X-Y. Remembering the equation (eq. 2.10) in that plane (Z=0) we can describe some cases of the function in (eq. 2.20). The trace of the tip of the E vector of the resulting wave:

For $\phi = \pm N\pi$, that is, $\delta = \frac{N}{2}\lambda$ (with N integer number) the equation of a straight linear is obtained (linear polarization Fig. 2.3a) as:

$$\left[\frac{E_y}{E_{0y}}\pm\frac{E_x}{E_{0x}}\right]^2=0 \qquad \text{(eq. 2.21)}$$

$$E_y=\pm\frac{E_{0y}}{E_{0x}}E_x \qquad \text{(eq. 2.22)}$$

It is worth to notice that the linear polarization of pair and odd N numbers are mutually orthogonal.

When $\phi=\frac{\pm N\pi}{2}$ or $\delta=\frac{N\lambda}{4}$, in which N is a whole odd number the equation of an ellipse (Fig. 2.3b) is obtained and of a circle if E_{01} and E_{02} have the same amplitude (Fig. 2.3c):

$$\left(\frac{E_y}{E_{0y}}\right)^2+\left(\frac{E_x}{E_{0x}}\right)^2=1 \qquad \text{(eq. 2.23)}$$

It is clear how the phase delay between two waves influences the polarization of the resulting one (Fig. 2.3).

2.2 Refractive Indices and Optical Indicatrix

Reflection, refraction, absorption [17] are some of the phenomena linked to the interaction between matter and light waves. Here the behavior of the light propagating through the media is outlined rather than the phenomena at the interfaces.
When the oscillating electric fields passes through a substance, interacts with atoms and ions perturbating the electric atmosphere. Actually, an oscillation is forced in the substance particles and the restoring forces of the induced vibrating dipoles (due to the substance and crystal structure) rule the propagation of the electromagnetic wave [22].
The interaction depends by the direction of the oscillation of the electric fields [21] and by the bonding forces of the structure [22].
The speed of the electromagnetic light wave is slower than the speed in vacuum when it passes through a medium [17] and depends by the magnetic and dielectric properties of the material [21] (eq. 2.24).

$$v = \frac{1}{\sqrt{\mu\varepsilon}} \qquad \text{(eq. 2.24)}$$

The ratio between the speed of light in vacuum c and the speed in the material is named refractive index n [17].
Since in this case the constant μ is the same as in the vacuum, the definition of the refractive index is (for further details see [13], [17] and [21]):

$$n = \sqrt{\varepsilon} \qquad \text{(eq. 2.25)}$$

Or, considering the dielectric impermeability $B = \frac{1}{\varepsilon}$ [21]:

$$n = \frac{1}{\sqrt{B}} \qquad \text{(eq. 2.25)}$$

In case of isotropic material, the refractive index is the same for each direction of the propagation while, in optically anisotropic there is a distribution of the refractive indices with respect to the direction of the light. In fact, light transmitted energy depends by the arrangement of the dipoles that conforms to the crystal requirements of internal symmetry [22]. Therefore, isometric crystals (e.g. cubic ones) or amorphous material transmit the energy in an isotropic behavior while, not isomeric structures (e.g. hexagonal or rhombohedra) have anisotropic transmission of light.
In these last materials, the refractive indices are represented by a positive-definite and symmetric tensor [23].
The light transmitted through the anisotropic media is represented by the eq. 2.26 in which D is the electric displacement vector (for further details see [20][21][22]).

$$\begin{pmatrix} D_x \\ D_y \\ D_z \end{pmatrix} = \begin{pmatrix} \varepsilon_{xx} & \varepsilon_{xy} & \varepsilon_{xz} \\ \varepsilon_{yx} & \varepsilon_{yy} & \varepsilon_{yz} \\ \varepsilon_{zx} & \varepsilon_{zy} & \varepsilon_{zz} \end{pmatrix} \begin{pmatrix} E_x \\ E_y \\ E_z \end{pmatrix} \qquad \text{(eq. 2.26)}$$

Or shorter

$$(D) = [\varepsilon](E) \qquad \text{(eq. 2.27)}$$

From the eigenvalues of $[\varepsilon]$ the principal refractive indices can be derived, which describe the optical behavior of the media.

$$n_x = \sqrt{\varepsilon_x}\ ,\ n_y = \sqrt{\varepsilon_y}\ ,\ n_z = \sqrt{\varepsilon_z} \qquad \text{(eq. 2.28)}$$

By the [17] and [20], considering that $[\varepsilon^{-1}](D) = (E)$, the dielectric energy is defined as follow [20][21][22]:

$$U = \frac{1}{2}[\varepsilon^{-1}](D)\cdot(D) \qquad \text{(eq. 2.29)}$$

In the most general case the surface with constant energy is an ellipsoid [22].

$$\frac{x^2}{\varepsilon_x} + \frac{y^2}{\varepsilon_y} + \frac{z^2}{\varepsilon_z} = C \text{ or} \qquad \text{(eq. 2.30)}$$

$$\frac{x^2}{n_x^2} + \frac{y^2}{n_y^2} + \frac{z^2}{n_z^2} = C \text{ or} \qquad \text{(eq. 2.31)}$$

$$B_x x^2 + B_y y^2 + B_z z^2 = C \qquad \text{(eq. 2.32)}$$

This ellipsoid describes the distribution of the refractive indices and it is named as Fresnel ellipsoid, index ellipsoid or optical indicatrix [13].
By eq. 2.30 three cases can be distinguished with respect to the light transmission according to the eigenvalues of eq. (2.26):

1) isotropic behavior ($n_x=n_y=n_z=n$), the ellipsoid became a sphere (Fig. 2.5) and the light is transmitted in the same way in each direction.

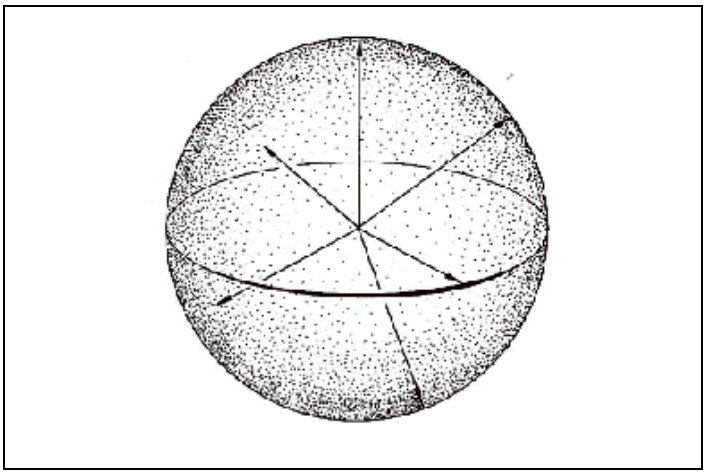

Fig. 2. 5-the image from [13] represents the transmission of light in an unstressed isotropic substance; the light propagation behavior is the same for each direction, the radius of the sphere is proportional to the refractive index.

2) anisotropic uniaxial behavior ($n_x=n_y\neq n_z$), the ellipsoid has one axis. This axis is normal to the circular cross section with the radius equal to $n_x=n_y$ and it is named *optical axis.* The refractive indices n_x *and* n_y have the same value and are named ordinary indices n_o. the other index n_z is named extraordinary index n_e (in Fig. 2.6 are reported the positive and negative ones [13]).

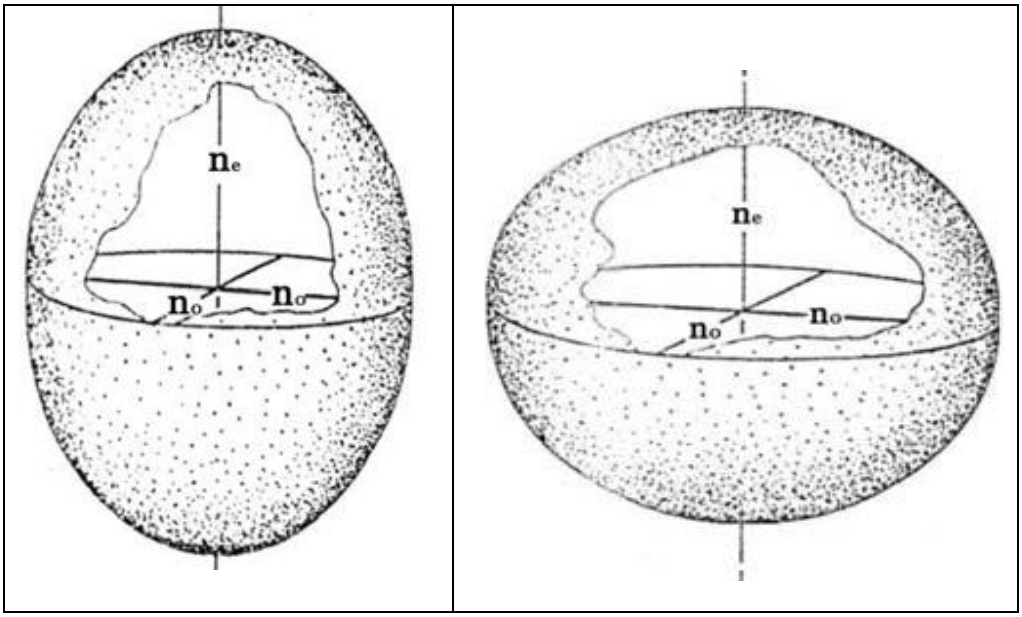

Fig. 2. 6-the uniaxial optical indicatrix is shown in the pictures (positive on the left, with $n_e>n_o$, and negative on the right). The light transport behavior changes as a function of the direction of propagation. The optical axis is the axis normal to the circular surface with its radius proportional to n_o (ordinary refractive index). In this direction, an isotropic behavior is maintained and the light does not change its initial polarization, running with one velocity. Any other direction shows anisotropic behavior and the birefringent effect [13], these directions are normal to ellipses with one axis equal to n_o and the other depending by the specific direction (n'). the resulting electromagnetic perturbance is the sum of two different waves mutually orthogonal polarized (as the axis of the ellipse normal to the direction n_o and n') and traveling with different velocities (a phase delay is carried out).

3) anisotropic biaxial behavior ($n_x\neq n_y\neq n_z$). In this case the ellipsoid has two axes with circular cross section (*two optical axes* that lie on the optical plane). Even in this case, ordinary and extraordinary refractive indices can be recognized as the radius of the circular cross sections and the dimension of the circular axes (in Fig. 2.27 are reported the positive and negative ones).

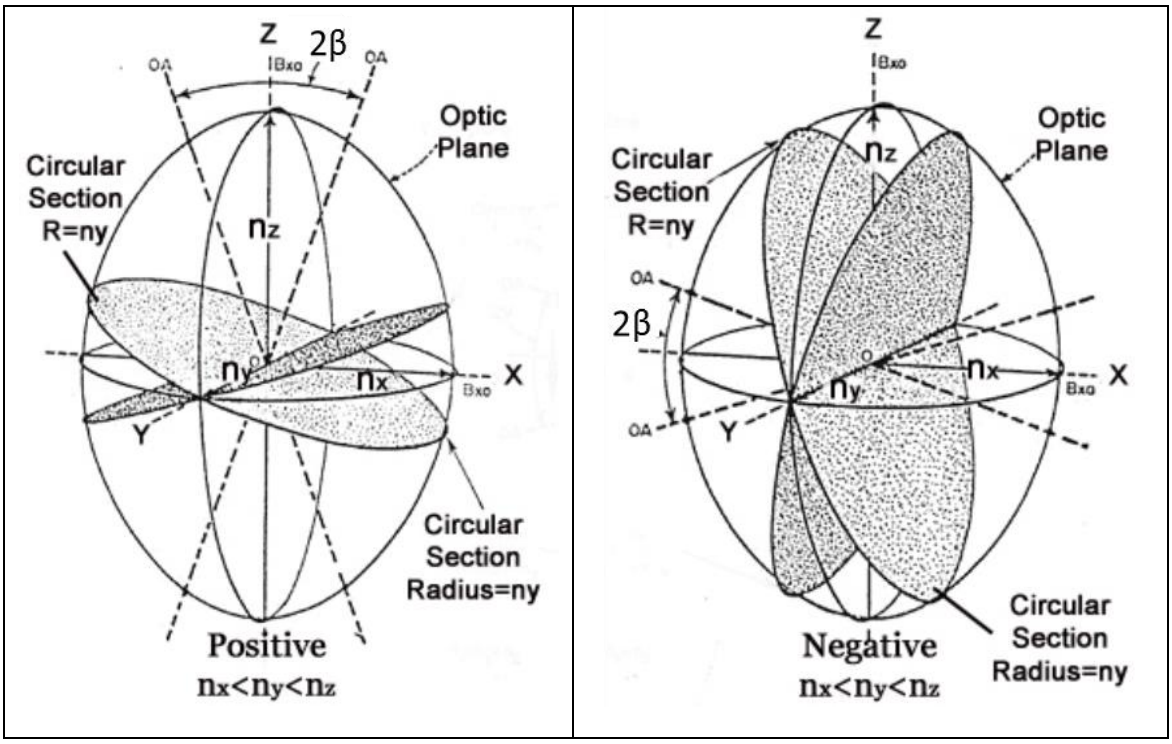

Fig. 2. 7-biaxial indicatrix, the optical axis are represented as the normal to the circular cross section. Along these directions an isotropic transport of light is present ruled by one refractive index (n_o). along any other direction the resulting perturbance is composed by two waves delayed and polarized as the axis of the ellipses normal to the specific direction.

The angle between these axes can be evaluated by (eq. 2.31) [17].

$$tg^2\beta = \frac{\left(\frac{1}{n_y}\right)^2 - \left(\frac{1}{n_x}\right)^2}{\left(\frac{1}{n_z}\right)^2 - \left(\frac{1}{n_y}\right)^2} \qquad \text{(eq. 2.33)}$$

In the last two cases, the media have an isotropic behavior in the direction of the optical axes only. In any other direction, it has been demonstrated by theory and proven by experiments that any electromagnetic perturbation consists in the sum of two plane and mutual orthogonally polarized light waves [13]. These waves are affected by different forces acting to restore the vibrating dipoles, therefore, they travel with different velocities [17]. In fact, for these directions the refractive indices are represented by the axis of their cross section. These anisotropic material, are naturally birefringent [14].

It is worth to remind that the combination of such waves gives a resulting wave with a polarization which depends by the relative delay.

In general, for the anisotropic media the light propagation is affected by the fact that the electric field *E* and the displacement vector *D* are not parallel except along the direction of the optical axes.

To get the idea of the behavior a sort of Huygenian construction [13] is presented considering that the axes of the index ellipsoid are the direction of vibration of the waves which move with a velocity related to that axis (inversely proportional to the refractive index).

It is comfortable introduce the “surface velocity” which is related to the optical indicatrix as mentioned above.

This means that the velocity surface about the ordinary light waves (governed by the ordinary index) is a sphere while the one about the extraordinary ray (velocity proportional to $\frac{1}{n_e}$) is still an ellipsoid.

Some section of this surfaces are presented and the wave front behavior explained in the Fig. 2.8 [13];

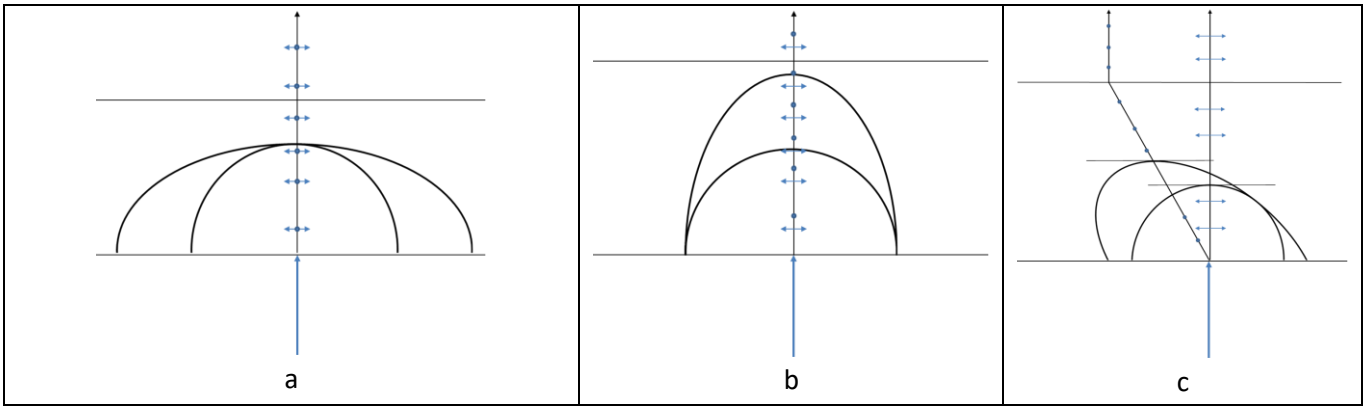

Fig. 2. 8-in the image, sections of the ray velocity propagation surfaces are shown. These surfaces are related to the optical indicatrix (velocity is proportional to $\frac{1}{n}$) and in the figures the trace of the refracted rays are drawn. The polarization is indicated as dots, when the vibration is normal to the section, and with doubled arrows lines, when the vibration is parallel to the section. The light impinges normally to the surface. In (a) the ray is not refracted and crosses the crystal thickness along the optical axis; therefore, a uniform and isotropic behavior as recognized. In (b) the light goes along the orthogonal direction with respect to the optic axis; even if the light run the same path, a birefringent effect is present. In fact, the resulting wave is composed by the sum of two orthogonally polarized waves which run with different velocities (one with V proportional to $\frac{1}{n_o}$ and the other with V proportional to $\frac{1}{n_e}$). The light emerges from the outlet surface with a phase delay. In (c) the crystal is cut randomly. The impinging ray (normal to the inlet surface) is divided in two rays. The ordinary ray (not refracted) follows the spherical propagation and the other (refracted) the elliptical. In the image the wave fronts are draw as tangent to the ray velocity surfaces. The overall electromagnetic perturbance is composed by two waves. The waves have different velocity and run through different paths. The extraordinary ray is refracted again at the outlet surface (normal to that surface). The emerging rays have achieved a phase delay.

It is clear how when rays of lights propagate in direction different from the optical axes, each ray is divided in two mutually orthogonally polarized waves which propagate with different velocities [13].

2.3 Bertin surfaces

In the previous paragraphs, it has been outlined how the delay between interacting light waves affects the resulting one. In our case the delay can be generated by birefringent material and it is ruled by their optical indicatrix (refractive indices distribution) and the relative ray velocity surfaces.
Consider the Fig. 2.8b, in that case two waves are travelling the thickness of the crystal along the same path but with different velocities and mutually orthogonal polarized.
At the outlet surface, they get a delay due to the thickness and to the different refractive indices (eq. 2.34). That is, defining the dimension of the thickness as *d:*

$$\delta = n_e d - n_o d \qquad \text{(eq. 2.34)}$$

It is convenient, here, to express the delay as optical path difference (related to the wavelength λ) and as phase delay ($\phi = \frac{2\pi}{\lambda}\delta$):

$$N\lambda = d\left(n_e - n_o\right) \qquad \text{(eq. 2.35)}$$

$$\phi = \frac{2\pi}{\lambda} d\left(n_e - n_o\right) \qquad \text{(eq. 2.36)}$$

About the delay (optical path or phase delay) it is possible to trace points with the same phase delay and optical delay in terms of number of wavelength. These points compose the so called *Bertin Surfaces* [13][24]*,* that is, the loci of point where the refracted waves get the same phase delay.
In Fig. 2.9 is reported the trace of the surfaces in 2D and 3D construction for the uniaxial crystals.

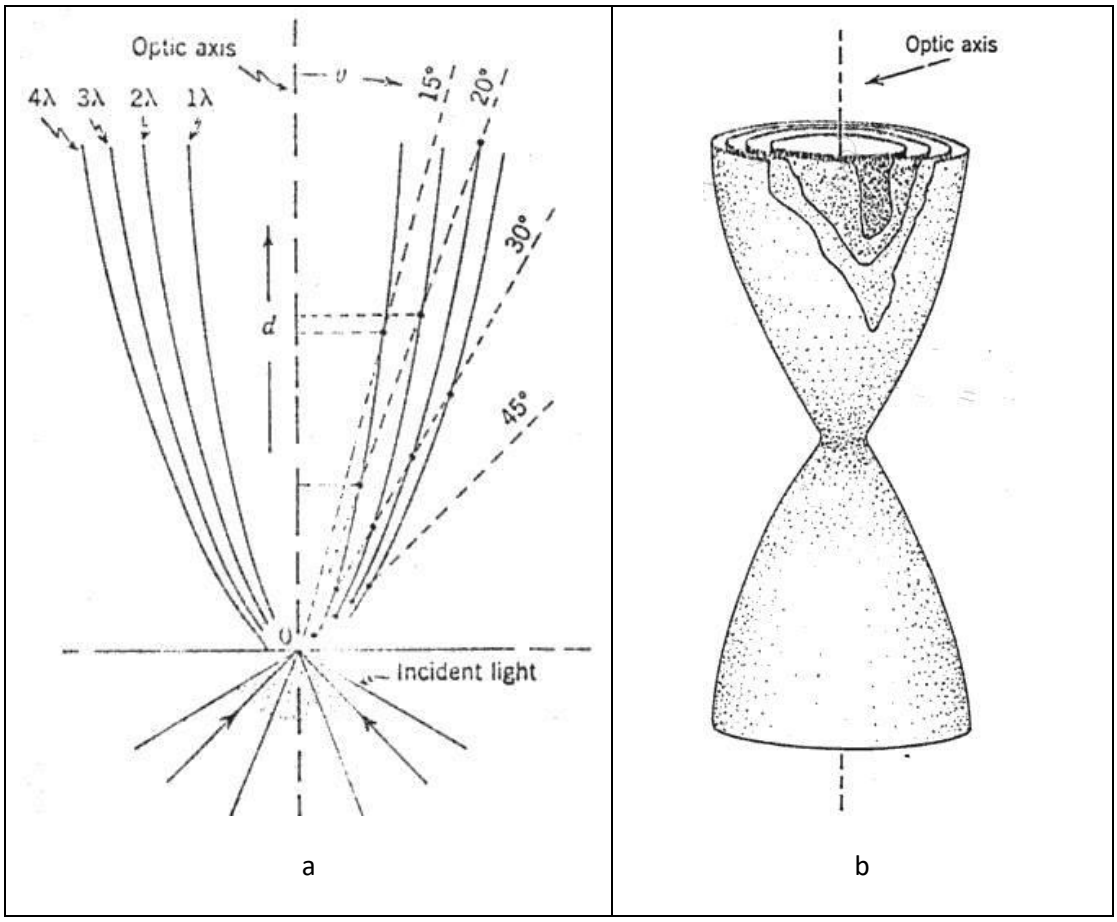

Fig. 2. 9- construction of the Bertin surfaces [13]; (a) two-dimensional representation of the equal delay or optical path difference as function of the angle of refraction. (b) three-dimensional reconstruction by means of the circular symmetry of the light behavior around the optic axis.

Considering a small angle between the ordinary and the extraordinary ray [17] the Fig. 2.9a can be represented with an equation similar to the (eq. 2.36 and 2.37):

$$\phi = \frac{2\pi d}{\lambda \cos\theta_m}(n_e - n_o)\sin^2\theta \qquad \text{(eq. 2.38)}$$

Where θ is the angle between the refracted ray and the optic axis, while θ_m is the angle between the optic axis and the bisector of the ordinary and extraordinary ray; practically, $\theta_m=\theta$. The same equation is achievable for the optical path difference.

$$N\lambda = \frac{d}{\cos\theta_m}(n_e - n_o)\sin^2\theta \qquad \text{(eq. 2.39)}$$

In the same manner, Bertin surfaces can be traced for the biaxial crystals. Hereafter the construction of the curves for the three planes of symmetry of the optical indicatrix are reported [13] (Fig. 2.10), described with mathematical approach as (eq. 2.35).

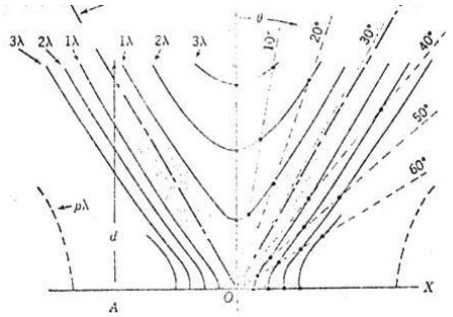 a	$N\lambda = \frac{d}{\cos\theta_m}(n_y - n_i)$ (eq. 2.40)
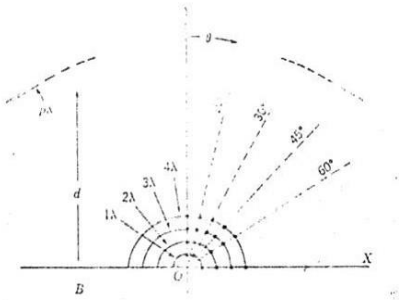 b	$N\lambda = \frac{d}{\cos\theta_m}(n_z - n_i)$ (eq. 2.41)
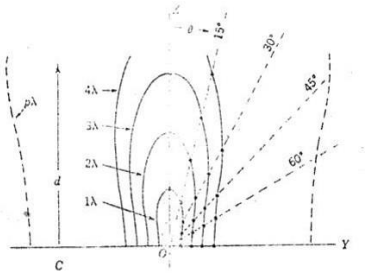 c	$N\lambda = \frac{d}{\cos\theta_m}(n_i - n_x)$ (eq. 2.42)

Fig. 2. 10 Two dimansional trace of the biaxial Bertin surface in the planes of the principal section of the optical indicatrix. On the right are repoted the relative path difference relation as function of the refractive indices.

The evaluation of n_i has been made for each angle by the (eq. 2.43) [13]:

$$(n_i)^2 = \frac{(n_z)^2 (n_x)^2}{(n_x)^2 \sin^2\theta + (n_z)^2 \cos^2\theta} \qquad \text{(eq. 2.43)}$$

By the Fresnel treatment [17] the Bertin curves can be represented by a relation similar to (eq. 2.39), taking into account that the refracted middle ray has an angle from each optic axis (θ_1 and θ_2).

$$N\lambda = \frac{d}{\cos\theta_m}(n_z - n_x)\sin\theta_1 \sin\theta_2 \qquad \text{(eq. 2.44)}$$

The curves and the mathematical relations are at the base of the construction of the biaxial Bertin surfaces (Fig. 2.11).

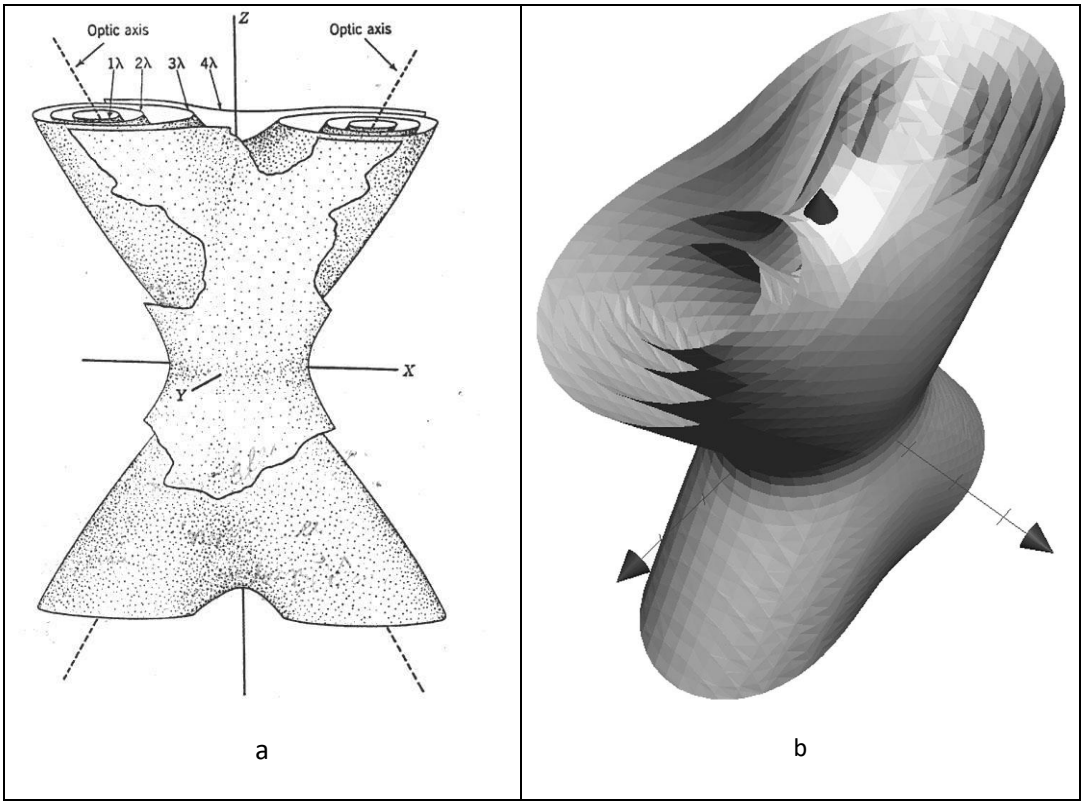

Fig. 2. 11- three-dimensional reconstruction of the equal path difference curves in biaxial crystals, (a) by [26]. (b) computer simulation of the Bertin surfaces by the model in [26].

Starting from this, a fourth-order polynomial expression representing the Bertin surfaces has been found in [20][27] (eq. 2.45):

$$(N\lambda)^2 = \left(x^2 + y^2 + z^2\right)\cdot(n_x - n_z)^2\left(1 - \frac{\left[z\cdot\cos\beta + x\cdot\sin\beta\right]^2}{x^2 + y^2 + z^2}\right)\cdot\left(1 - \frac{\left[z\cdot\cos\beta - x\cdot\sin\beta\right]^2}{x^2 + y^2 + z^2}\right) \qquad \text{(eq. 2.45)}$$

A three-dimensional representation of the model described by (eq. 2.45) is shown in Fig. 2.11b.

2.4 Conoscopic Fringe Patterns

The Bertin surfaces are mathematical concepts which are helpful to determine the optical path difference and the phase delay of light waves traveling through a birefringent crystal. Fringe patterns are observed using polarized light and optical systems. The morphology of those patterns is due to the path difference; therefore, they are directly related to the Bertin surfaces.

Polarizers are optical accessories which have the capability to absorb linear polarized light which has an angle with respect to polarizer transmission axis [12] (Fig. 2.12). They are at the bases of numbers of optical systems like polarized microscopes [13] and polariscopes [28] used, classically, for photoelastic observation.

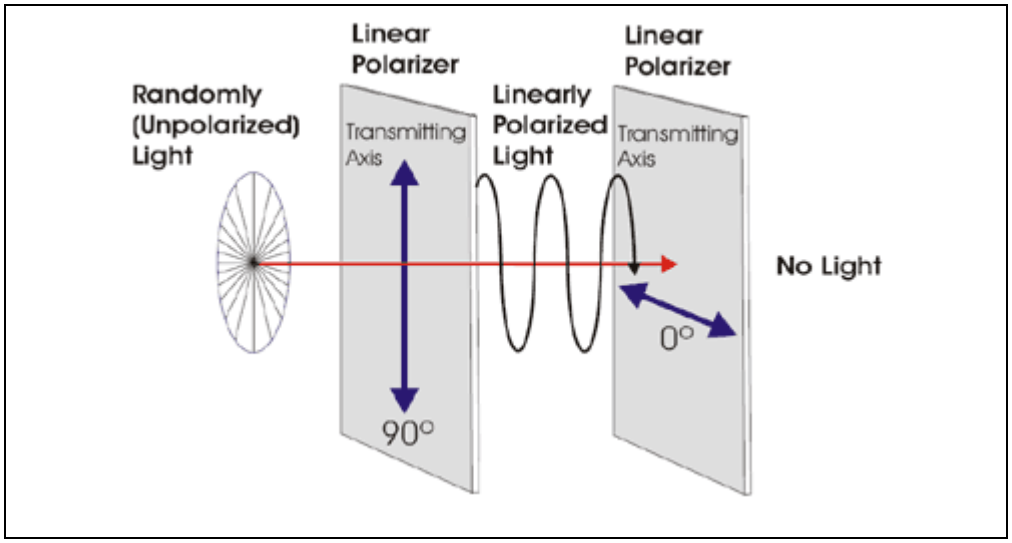

Fig. 2. 12 a schema of the behavior of the polarizer. In typical optical devices like polariscopes or polarized microsopes, the second polarizer (0°) is called analyzer.

A simple and helpful method using vectors is presented (see for details [13]), to evaluate the light transmitted by the analyzer when it is crossed by π/2 with respect to the polarizer (Fig. 2.13).

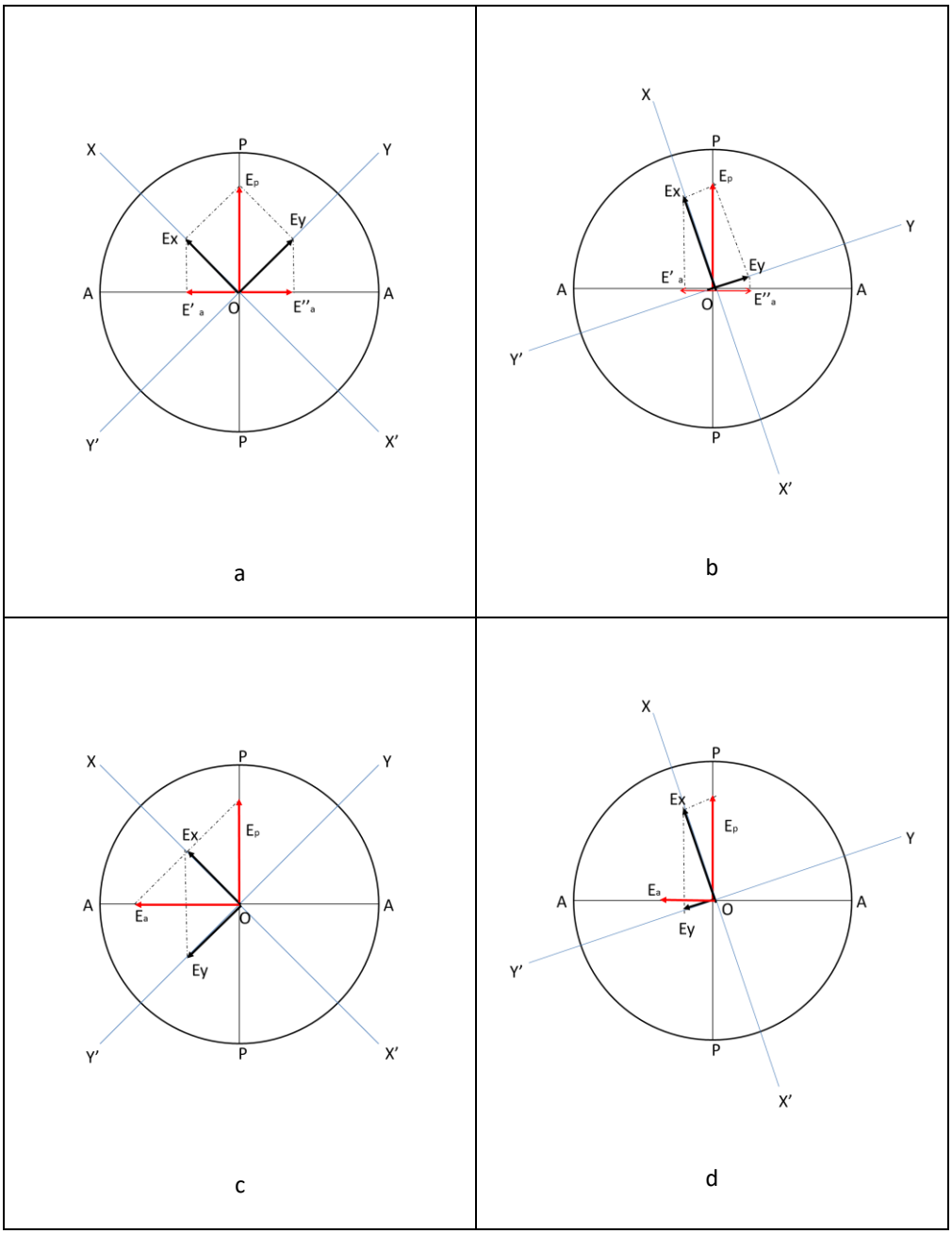

Fig. 2. 13-a scheme to evaluate the light, emerging from the crystal outlet surface, transmited by the analyzer. XX' and YY' are the direction of the plane of vibration of the light waves. PP and AA are polarizer and the analyzer. The polarized electric field is represented by Ep; Ex and Ey are its component along the vibration planes. In (a) and (b) the wave components (in black) have a Nλ path difference, therefore they are in the same positive quadrant X-Y. The resulting vectors on the analyzer are equal and in opposition, no light is transmitted. In (c) and (d), the path difference of the components is (N/2)λ with N odd number. Ey is, in this case, in the negative part of YY'. The resulting vectors on the analyzer are in the same direction. Intensity is transmitted due to the constructive interference.

In the Fig. 2.13, polarizer and analyzer are named as PP and AA while the traces of the vibration planes of the light emerging from the crystal are XX' and YY' (the axis of the relative ellipse obtained as a section of the optical indicatrix normal to the light ray).

The amplitude of the electric field emerging from the polarizer (P) is represented by E. Crossing the crystal, the light is composed by two rays vibrating along XX' and YY' (E_x and E_y). The amplitude of the electric field transmitted by the analyzer is named as E_a. In the case a and b of the Fig.2.13, since the delay is Nλ with N a whole pair number, the vectors of the electric fields parallel to the analyzer are equal and opposite. A destructive interference is obtained.
In (c) and (d), since the path difference is (N/2)λ (N an odd number), the component on YY' is opposite to the one in (a) and (b) (this is in accord with the eq. 2.20). Therefore, the electric fields vectors on the analyzer are equal and in the same direction. A constructive interference is carried out. In the case (d) the transmitted intensity is lower.
Illuminating a crystal with convergent polarized light, like in the scheme of Fig. 2.9a and 2.9b, the plane of vibration of the emerging ray in Fig. 2.14 are obtained.

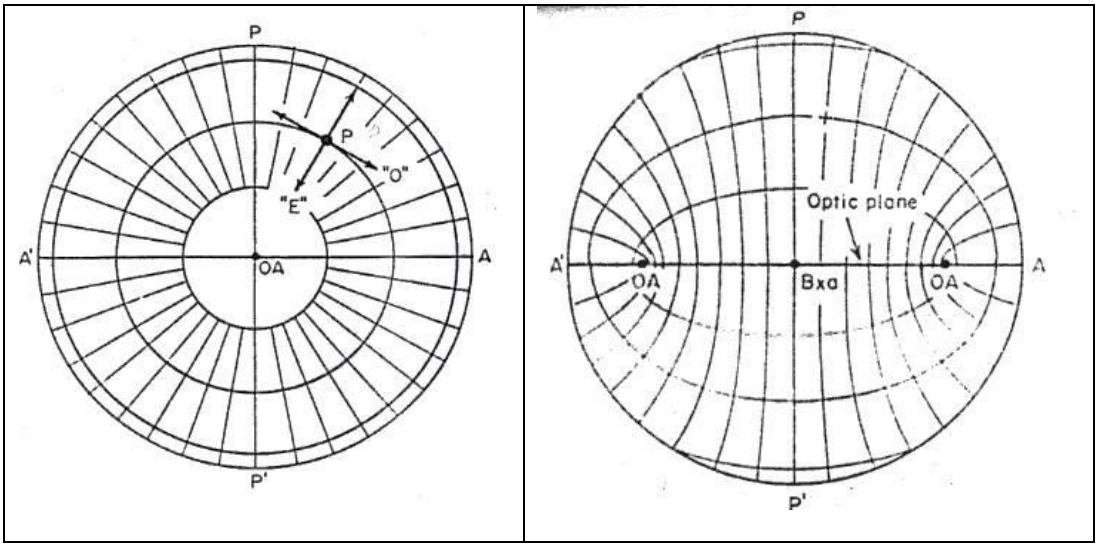

Fig. 2. 14 the lines represent the trace of the vibration planes for each direction angle of diverging light inside the crystal. Left, uniaxial crystal observed along its optic axis; right, biaxial observed along its acute bisector.

By the system in Fig. 2.15, each couple of parallel rays vibrating on orthogonal plane, are recombined on the focal plane.
Their optical path difference (or phase delay), described by the Bertin surface, determine destructive or constructive interference.

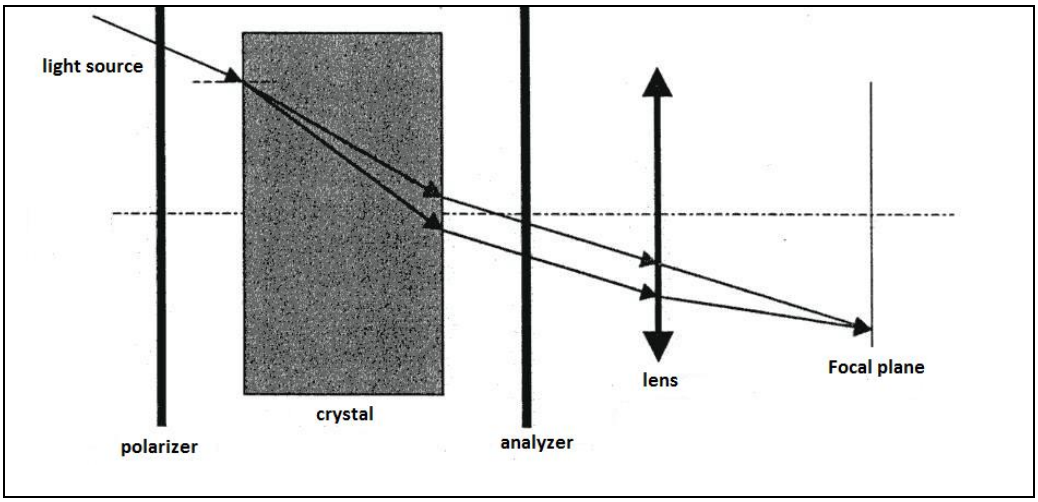

Fig. 2. 15 typical observation scheme with the sample between two crossed polarizers. The lens makes the parallel rays, emerging from the sample, converge on the focal plane. A bijective correspondence between point to angle is achieved and an interference is carried out on the focal plane.

The typical fringe patterns carried out are shown in Fig. 2.16 which can be though and expressed as the intersection of the Bertin surfaces with planes (the edge surfaces of the crystal).

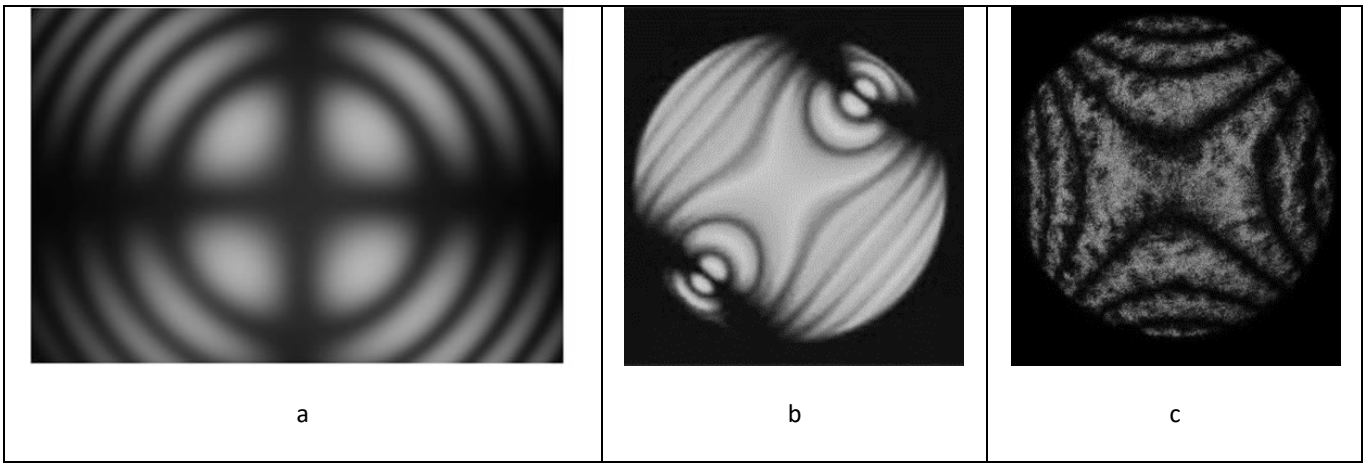

Fig. 2. 16- conoscopic fringe patterns, uniaxial (a), biaxial (b) and uniaxial observed along the optic axis normal. The black cross in (a) and (b) is because the planes of vibration coincide with the polarizer and analyzer axis, therefore, no light is transmitted.

Chapter 3

3 Birefringent crystals photoelasticity and the diffused light polariscope

Photoelasticity is a classical measurement technique suited to observe stress in transparent isotropic materials [10]. The birefringence induced by the stress leads to an estimate of the stress condition by the appearing of fringe patterns due to the induced refractive indices difference [12].
The presented research deals with naturally birefringent media in which a fringe structure is already present even when the stress is not present [13]. Usually these patterns are symmetric.
Then, in case of stress it is observed a modification or distortion of the symmetries of the patterns due to the deformation of the stressed lattice [12].
Hereafter are outlined, briefly, the principles governing phooelasticity of natuarally birefringent materials and the piezo-optic behavior of the anisotropic transparent media as well as the diffuse light polariscope technique; its strength and its limitation will be underlined.

3.1 Crystals Photoelasticity: Piezo-Optic effect

Each transparent material is affected by a changing of its optical properties with respect to stress conditions.
In isotropic materials, the stress tensor (Lamè ellipsoid) [29] interacts with the structure modifying the spheroid indicatrix so as to became an ellipsoid (Fig. 3.1).

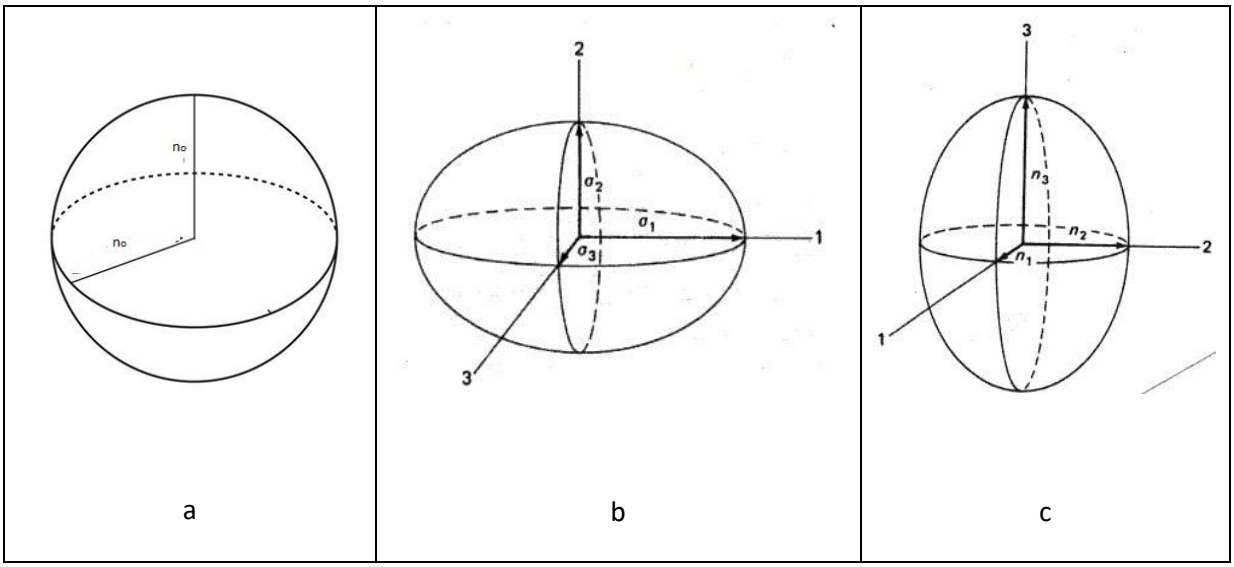

Fig. 3. 1- A graphical representation of the interaction of the isotropic optical indicatrix (a) with the stress tensor (b) named Lamè ellipsoid [29]. The spherical indicatrix (a) turns in a general ellipsoid (c).

The induced birefringence is governed by the Photoelastic constants as follow.

$$\begin{aligned} n_1 - n_0 &= f_1\sigma_1 + f_2(\sigma_2 + \sigma_3) \\ n_2 - n_0 &= f_1\sigma_2 + f_2(\sigma_1 + \sigma_3) \\ n_3 - n_0 &= f_1\sigma_3 + f_2(\sigma_1 + \sigma_2) \end{aligned} \qquad \text{(eq. 3.1)}$$

Where f_1 and f_2 are the elasto-optic coefficients. Therefore, a stressed isotropic material behaves as a birefringent substance. Managing the equations 3.1 so to eliminate n_0 the following relations are obtained:

$$\begin{aligned} n_2 - n_1 &= f(\sigma_1 - \sigma_2) \\ n_3 - n_2 &= f(\sigma_2 - \sigma_3) \\ n_1 - n_3 &= f(\sigma_3 - \sigma_1) \end{aligned} \qquad \text{(eq. 3.2)}$$

Where f is the relative photoelastic constant. By the equations 3.2 the path difference and the ellipsoid of Fig. 3.1 can be traced and linked to the stress tensor [12].
The distortion of the crystal lattice symmetries (influencing the electronic displacement), due to the stress tensor, leads to a change in the light transport and transmission. The electromagnetic atmosphere is modified due to that distortion and the light perturbation faces different restoring forces of the oscillating dipoles.
The refractive indices distribution changes and the relative optic indicatrix modifies its shape. This is actually named Piezo-Optic effect.
The magnitude and the shape of this distortion are depending on the characteristic Piezo-Optic π matrix (it can be considered a tensor of the photoelastic constants) [23].
This matrix links the stress tensor to the dielectric impermeability tensor deformation B and, therefore, to the deformation of the distribution of the refractive indices [13].
Actually, it governs the interaction of the tensile ellipsoid (Lamè Tensor) [30] with the index ellipsoid which (Fig. 3.1).
An example for tetragonal crystals (the π tensor belongs the point group 4, $\underline{4}$, 4/m) is given in the equation 3.3 [23].

$$\begin{pmatrix} \Delta B_{xx} \\ \Delta B_{yy} \\ \Delta B_{zz} \\ \Delta B_{xz} \\ \Delta B_{yz} \\ \Delta B_{xy} \end{pmatrix} = \begin{bmatrix} \pi_{xxxx} & \pi_{xxyy} & \pi_{xxzz} & 0 & 0 & \pi_{xxxy} \\ \pi_{xx} & \pi_{yyyy} & \pi_{xx} & 0 & 0 & -\pi_{xxxy} \\ \pi_{xx} & \pi_{xx} & \pi_{zzzz} & 0 & 0 & 0 \\ 0 & 0 & 0 & \pi_{xzxz} & \pi_{xzxz} & 0 \\ 0 & 0 & 0 & -\pi_{xzxz} & \pi_{xzxz} & 0 \\ -\pi_{xyxx} & \pi_{xyxx} & 0 & 0 & 0 & \pi_{xyxy} \end{bmatrix} \begin{pmatrix} \sigma_{xx} \\ \sigma_{yy} \\ \sigma_{zz} \\ \sigma_{xz} \\ \sigma_{yz} \\ \sigma_{xy} \end{pmatrix} \qquad \text{(eq. 3.3)}$$

The resulting [B] tensor is than given (in a shorter notation) by the expression [26]:

$$[B] = [B_0] + [\Delta B] = [\varepsilon]^{-1} \qquad \text{(eq. 3.4)}$$

The optical indicatrix will modify in with respect to the eq. 3. 32. The resulting eigenvalue and eigenvectors of [*B*] will warp the index ellipsoid by relation $n_i = \frac{1}{\sqrt{B_i}}$ due to the piezo-optic effect.

Remembering the relation (eq 2.33), here reported $tg^2\beta = \frac{\left(\frac{1}{n_y}\right)^2 - \left(\frac{1}{n_x}\right)^2}{\left(\frac{1}{n_z}\right)^2 - \left(\frac{1}{n_y}\right)^2}$, a variation of the optic angle is observed whenever stress is present.

Considering a uniaxial crystal, where $n_x=n_y=n_o$, it becomes biaxial ($n_x=n_y=n_o \neq n_y=n_e$) in case of plane stress orthogonal to its optic axis (Fig. 3.2).

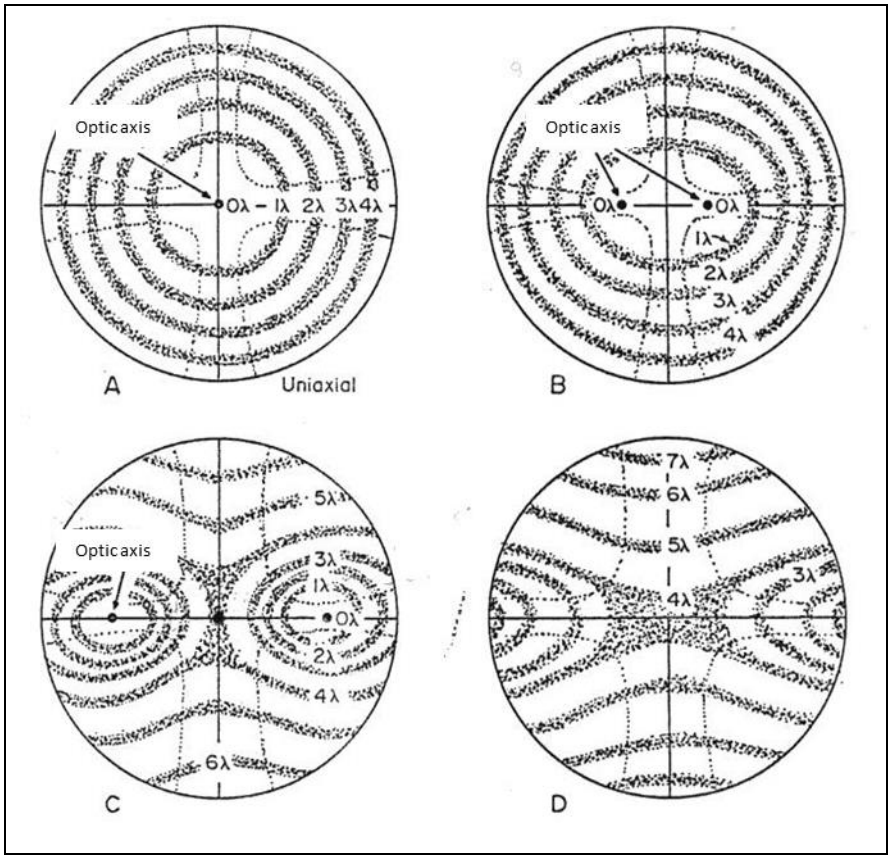

Fig. 3. 2 – in the image the induced biaxial behavior for a uniaxial crystal is shown. The fringes are due to the intersection of the Bertin surfaces with a plane orthogonal to the optica axis. The load increases from (A) to (D), the image clearly shows that the angle between the induced optic axes increases as well.

The construction of the entire Bertin surfaces changes due to the warping of the optical indicatrix [27] (eq. 2.37 to eq. 2.44), as it is reported in Fig. 3.3 by the simulation obtained from the expression (eq. 2.44).

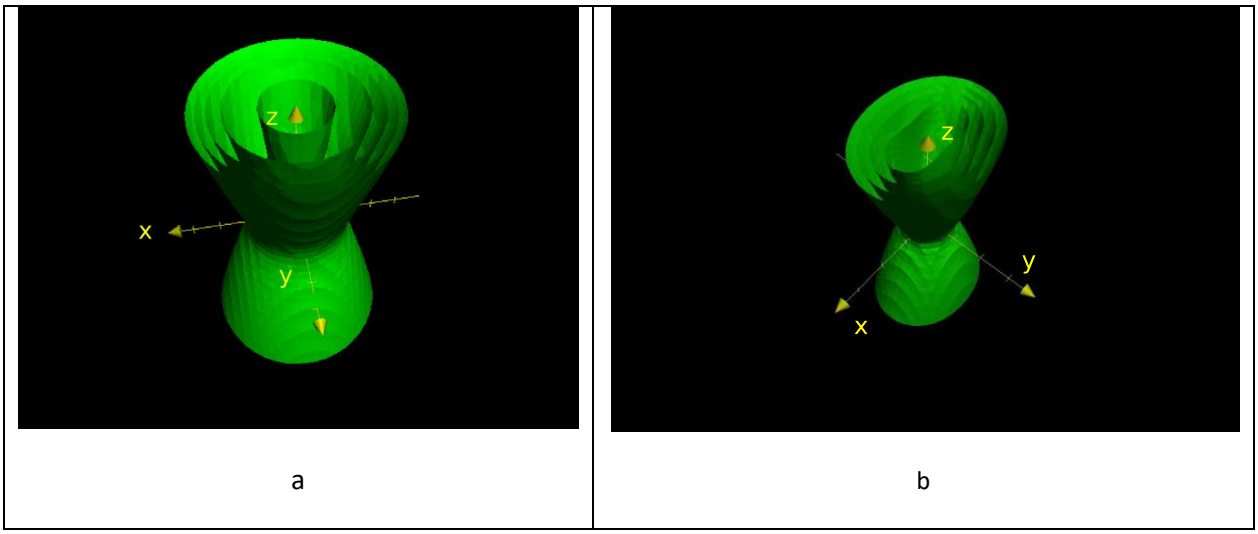

Fig. 3. 3- simulation of the Bertin Surfaces distortion [27] by the model in eq. 2.44. In (a) the initial uniaxial state and in (b) the induced biaxial deformation. In (b), the axes are not indicated but the Z direction of the optical indicatrix which coincide with the original uniaxial direction.

3.2 *Diffused light polariscope.*

Is the simplest and, actually, the state of the art system for the photoelastic assessment of stress distribution in transparent material [12].
The transparent media is placed between two crossed polarizers (polarizer and analyzer as it has been outlined in the previous chapter) and illuminated by diffused monochromatic or white light, usually a sodium lamp (λ=589,3 nm); finally, a camera acquires the fringe pattern images (Fig. 3.4).

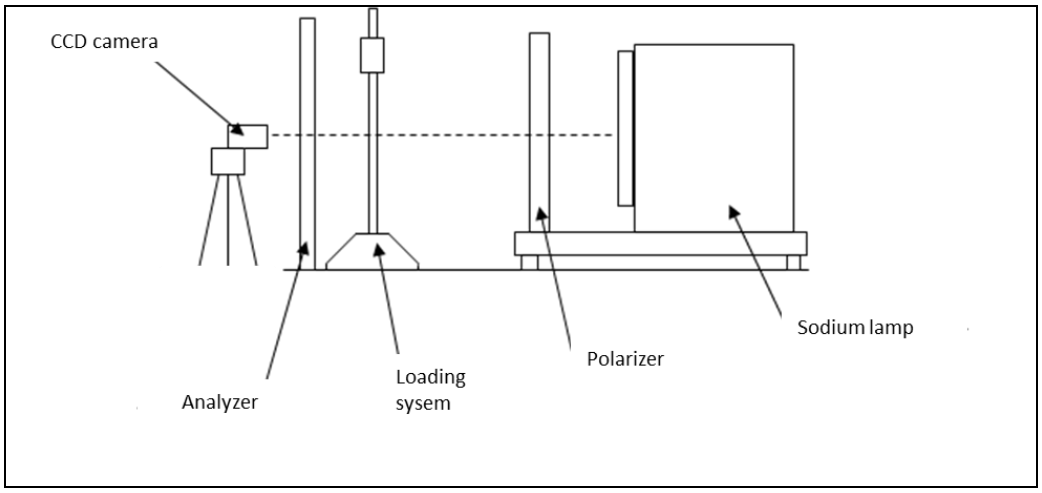

Fig. 3. 4- the lay-out of a classical diffuse light polariscope. In the scheme are reported the load devices, to test the sample with known stress condition, and the camera focused to the infinity so to get the fringe pattern on the sensor.

To get the fringes on the camera sensor the lens is focused to the infinity. Therefore, each point in the sensor corresponds to an angle of light rays emerging from the sample.
The images carried out are presented in Fig. 3.5. The fringe pattern in the picture are due to the observation of a PWO (uniaxial, point group 4/m) sample along its optic axis (Z axis in Fig. 3.3). The sample has been illuminated by sodium lamp.
In the figure 3.5, observation in unloaded condition (Fig. 3.5a) and in uniform compressive load condition (Fig. 3.5b) are presented.
Since has been outlined in the previous chapter, the fringes are due to the intersection of the Bertin surfaces with a plane (the crystal geometrical surfaces).
In unloaded condition (Fig. 3.5a) the pattern is composed by a series of circles due to the crystal symmetry.

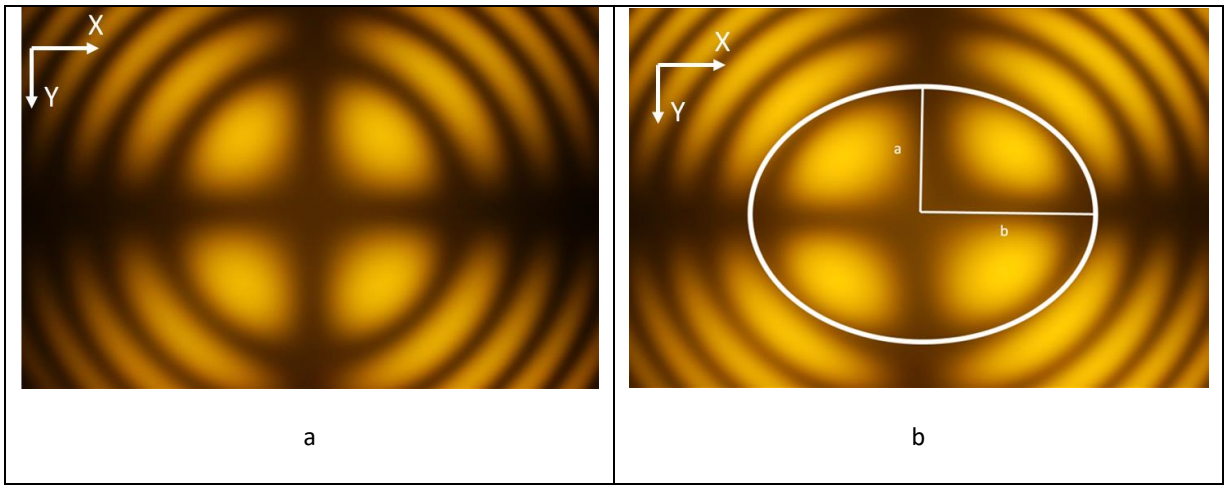

Fig. 3. 5- fringe patterns acquired by the diffuse light polariscope. The light source is a sodium lamp (520 nm) and the uniaxial sample is observed along its optic axis. In (a) the sample is stress free while in (b) in homogeneous compressive load. The induced biaxial behavior leads to a formation of Cassini like shaped fringes (b). for low level of distortion, the Cassini curves can be approximate with ellipses (b).

The uniform compressing state, induces the biaxial behavior and the Bertin surfaces deform accordingly [20]. Consequently, the pattern turns like in Fig. 3.5b. That pattern can be considered composed by Cassini like curves, expressed like follow:

$$[(x-a^2)+y^2][(x+a^2)+y^2]=b^4 \qquad \text{(eq. 3.3)}$$

If the distortion is not too high, as it is the case of relatively low residual strain fields normally encountered in crystals, the induced Cassini curves can be considered ellipses with negligible error, therefore it is convenient relate the stress to the ellipticity of the fringes [31] as:

$$\Delta\sigma = \frac{C}{f_\sigma} \qquad \text{(eq. 3.4)}$$

Where f_σ is the photoelastic constant measured in the calibration step [32] which depends by the π matrix and, linearly by the thickness or optical path [32].

C is the ellipticity evaluated by the ratio of the major and minor ellipses semi axis (Fig. 3.5b) and as [31]:

$$C = \frac{b}{a} - 1 \qquad \text{(eq. 3.5)}$$

Actually, the ellipticity of the first order of the fringe pattern is considered.
With this set-up, if more complex stress distribution is induced, the fringes pattern will be complex as well [20].
An example is shown in the Fig. 3.6; the sample has been bent in a four-point bending test [33]. The pattern which can be observed, is superimposed to the sample geometry in Fig. 3.6a and shown in detail in Fig. 3.6b. A pear like shape with a vertical axis appears, which is physically related to the stress gradient along the vertical axis of the sample.

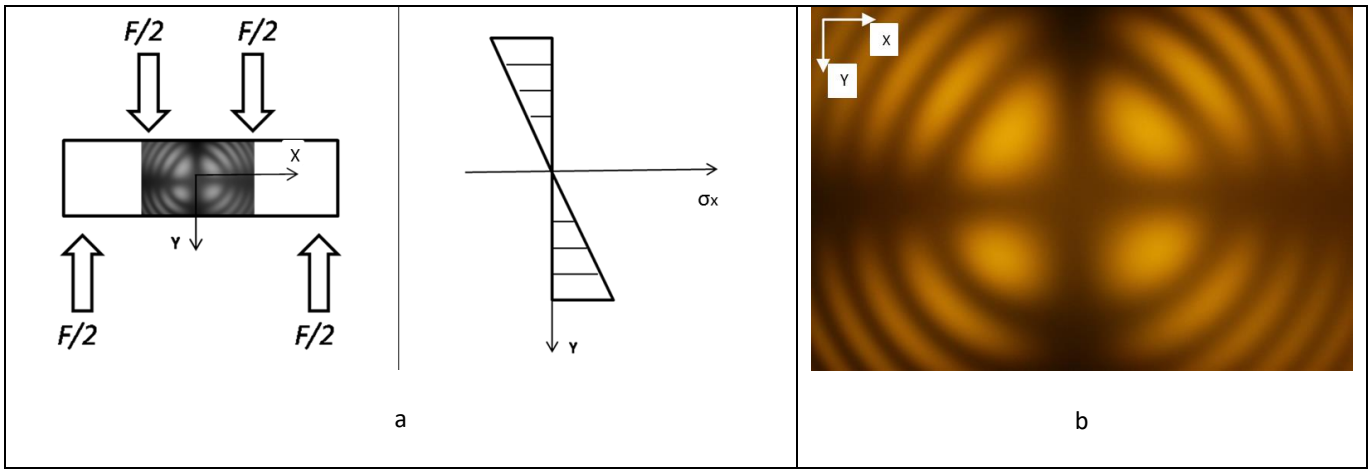

Fig. 3. 6 – The results due the four points bending test are presented in the image. In (a) the fringe pattern is superimposed to the sample geometry with the relative induced stress trend (the typical antisymmetric distribution of σ_x). The resulting fringe pattern is highlighted in (b) in which a pear-like shape is recognizable. It remains a complex pattern to analyze, the neutral axis (where σ_x=0, is not detectable)

Indeed, the fringe pattern is due to the classical antisymmetric distribution of σ_x along the Y axis and has been modelled in [20], but it remains difficult to extract from this image the actual stress distribution in the sample.

For example, it is not easy find detect the position of the neutral axis (σ_x =0) in the fringe pattern, therefore it is clear that for complex stress distribution complex fringe shape to analyze are carried out [20]. Moreover, in the case of internal stress this technique "mediates" the stress on a relative large volume so punctual magnitudes are difficult to be detected.

This method has demonstrated to be sensitive to the overall condition of the crystals. The environmental conditions like vibration, temperature and crystal surfaces polishing are not critical for this measurement system but it presents some limitation listed hereafter:

1) The diffused light impinges on the crystal with infinite angles and in a random way; this can affect the formation of the fringes. The phenomenon could be increased by internal reflections of the light at the boundary surfaces.
2) It is difficult to refer the pattern to a specific location inside the crystal volume. In fact, the crystal is fully illuminated, therefore the method is intrinsically a volume method, and does not allow for a spatially resolved local inspection. This affects negatively the spatial resolution of the measurement [34].
3) The matter mentioned above will influence the sensitivity too. Actually, it is difficult to detect concentrated stress, smooth variation and local distribution of the residual stress. Since a unique pattern is obtained from the entire volume, these condition as well as local defect are averaged on the overall probe volume [33].
4) As already clarified, from a complex stress distribution, a complex shape of the fringe pattern derives. Therefore, it is difficult to analyze it so to get information about the spatial distribution of stress and identify local defects [35].

If 1) is not too critical, 2), 3) and 4) highly affect the measurement sensitivity and spatial resolution. It therefore remains a method to have a reliable but coarse evaluation of the birefringent media condition.

Chapter 4

4 Innovative contribution: Laser Conoscopy and Sphenoscopy

In this chapter, the contribution and the developed methods to overcome the limitation introduced in the previous section, will be given in detail.

The developed methods and systems have improved the capability of a reliable and precise analysis. The systems are provided of a dedicated algorithm so as to analyze the fringe pattern images with a low uncertainty.

The following steps will be outlined:

1. In the first step, the sensitivity and the resolution of the Photoelastic measurement has been improved by the developed laser conoscopic method.
2. In this second step, the method in (1) has been adapted to observe uniaxial crystals orthogonally to the optic axis. Here, the first attempt to measure in a different position with respect to the optic axis will be discussed.
3. The last step is about the development of a technique (Sphenoscopy) which fastens the inspection and simplifies the analysis of the crystal state in each direction of observation.
4. The dedicated algorithm to analyze images will be discussed in this section.
5. In this last part, the validation tests and the results with respect each developed methods are presented.

4.1 Laser Conoscopy

The limitations outlined in the previous chapter have been overcome by using a laser light polariscope.
The laser light provides some advantages exploited for the purpose. That light has high quality characteristics in terms of polarization, directivity, wave length stability and coherence.
These characteristics have allowed the developing of the methodology whose set-up is shown in a schematic view in Fig. 4.1.

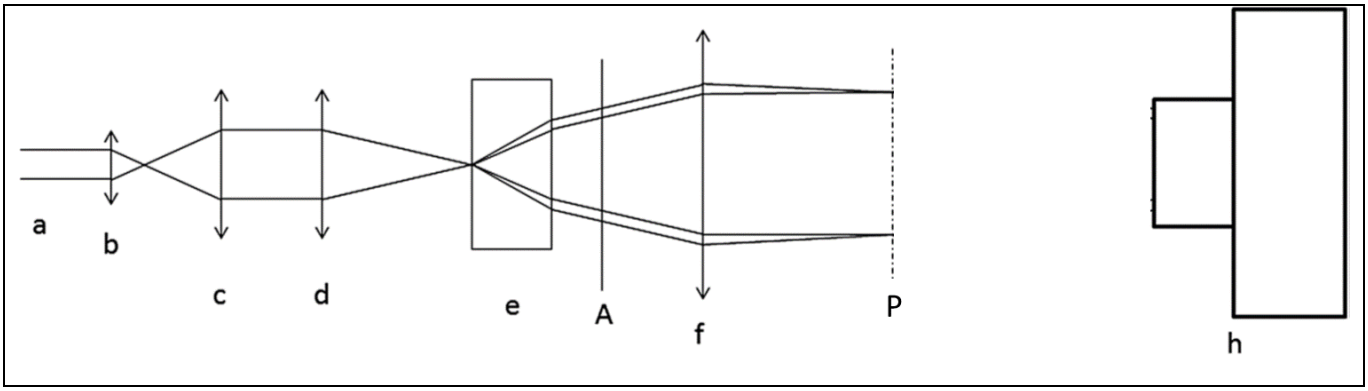

Fig. 4. 1- the laser conoscopy lay-out. The two lines in (a) represent the boarder of the laser beam, the lens system (b and c) is a beam expander which magnifies the initial beam. The enlarged beam is focused on the crystal surface by the lens (d). In the crystal sample (e) a conic probe volume is generated and the light undergoes the birefringent effect (represented by the double lines), the light is confined in that known volume. The rays, emerging with the phase delay, cross the analyzer (A) and are focused on the ground glass screen P; the screen is placed at the focal lenght of the lens (f). On that plane the parallel rays are recombined so to get the interference. The fringe pattern image is diffused by the ground glass and finally acquired by the camera (h) focused on (P).

The He-Ne laser produces a coherent and linearly polarized light beam (a). That beam is expanded by the beam expander lens system (b and c) and, then, focused by the spherical lens (d) on the crystal inlet surface. Inside the crystal (e) a conic probe volume is generated (Fig. 4.2a) and the birefringent effect is carried out (in the Fig. 4.1 it is indicated by the double lines).
This part of the system allows to confine the light is a specific part of the crystal volume. The generated probe volume could be easily managed by the optical system (b), (c) and (d) in Fig. 4.1 [34].
The light rays get the optical path difference crossing the crystal thickness and emerge from the outlet surface of the sample.

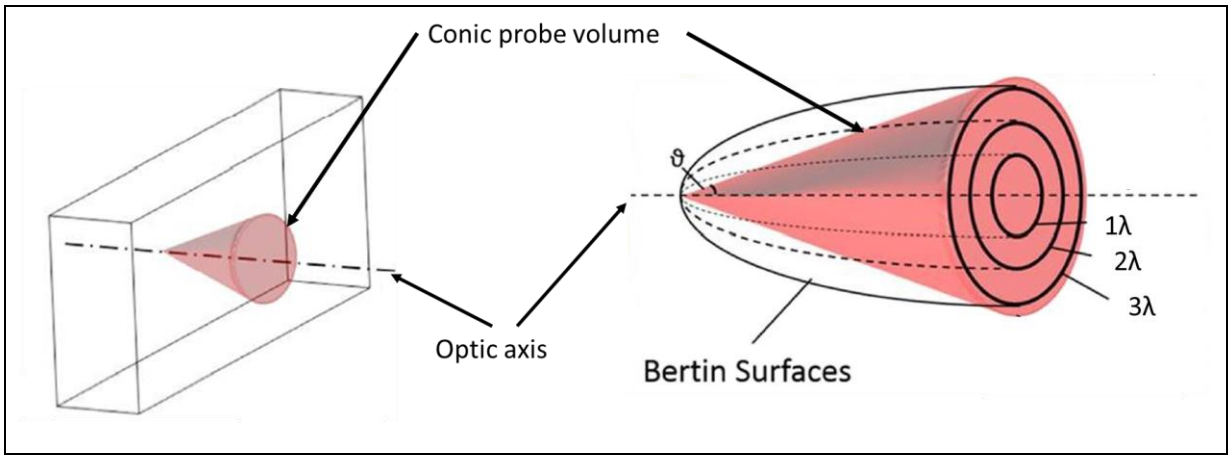

Fig. 4. 2- schematic representation of the conic probe volume and the generation of the relative fringe pattern (observation along the optic axis). Differently from the diffuse light polariscope, by laser conascopy the light is confined in a specific part of the sample volume and with known angles. By the Bertin surfaces, the fringe pattern is due to the angle of incidence and the thickness of the sample. The phenomenon is schematically represented in the right side of the figure.

As explained in the previous sections, for each ray impinging on the sample, two rays orthogonally polarized emerge from the sample and run through the crossed analyzer (A). That position of the analyzer in the lay-out avoid any risk of unwanted photoelastic effect of lens (f) and the screen (p).
The light waves are recombined on the screen (a ground glass in (p)) placed at the focal distance of the lens (f).
Here, the interference fringes are generated; the pattern is acquired by the camera (i) that, now, is focused on the screen (p).
This method has provided some advantages, listed below, to the photoelastic assessment of the crystal state.

1. The coherent light is precisely confined in a specific part of the sample volume; therefore, the crystal is not fully and randomly illuminated; impinging angles and the illuminated volume are known (Fig 4.2a) [34].
2. The generation of the fringe pattern is more accurate, precise and sensitive by the coherence, the directivity and the precise polarization of the laser light.
3. The pattern is due uniquely to the illuminated volume; since the probe volume can be managed, reducing its dimension the sensitivity and spatial resolution are largely enhanced [33]. Concentration of stress or smooth gradient are easily detected [34].
4. This controllable probe volume allows to get a precise study and characterization of the material; e.g. the number of fringe orders to generate can be decided a priori verifying the model of eq. 2.37 (see validation test section).
5. Whatever the stress distribution is, the volume can be reduced to dimension in which stress can be considered uniform. Therefore, no complex pattern shapes are expected; e.g. in observations along the optic axis, only circles and ellipses are expected (see the validation test section) [34].
6. A very detailed map of stress distribution can be carried out scanning a grid of points over the entire sample volume; the spatial resolution is limited only by the position system and not by the probe volume.

Indeed, the method is more accurate and sensitive than the diffused light techniques, allowing a local and pointwise inspection [33]. The typical images acquired by the system, observing along the optic axis of a uniaxial crystal, are presented in Fig. 4.3.

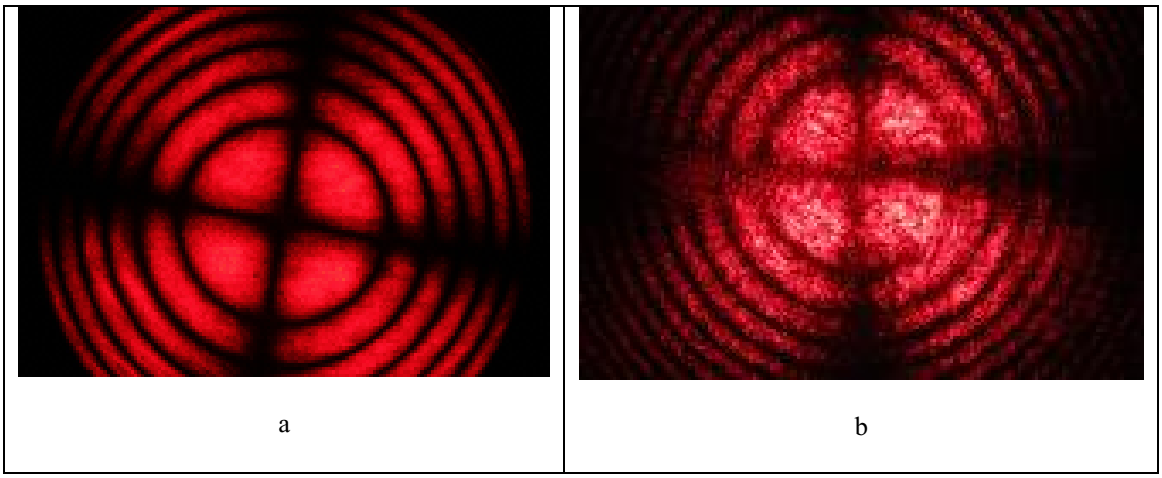

Fig. 4. 3-Typical fringe pattern (PWO uniaxial) acquired by laser conoscopy observing along the optic axis of the uniaxial crystal. The bad quality of the image in (b) is due to the condition of the surface. Chipping and scratches increase the noise due to the speckle, reflections and diffractions.

The use of the coherent light and the reduction of the probe volume dimensions, have enhanced the sensitivity with respect to the measurement conditions too. Vibration and surface conditions can badly affect the quality of the conoscopic images acquired (Fig. 4.3b) [33].

A modified version of the set-up shown in Fig. 4.1 has been presented in [33]. The difference consists in substituting the ground glass screen with a second lens (g) (Fig. 4.4). This lens is placed at a distance equal to its focal lens from the focal plane of the lens (f). The lens (g) turns the diverging rays in parallel and directed to the camera which, now, is again focused to the infinity.

In Fig. 4.4 is reported the modified system. This allows to reduce the part of the speckle noise, due to the screen granulometry, and to acquire as much light as possible. On the other hand, it needs an accurate alignment of each part of the acquiring section (lens (f) lens (g) and camera).

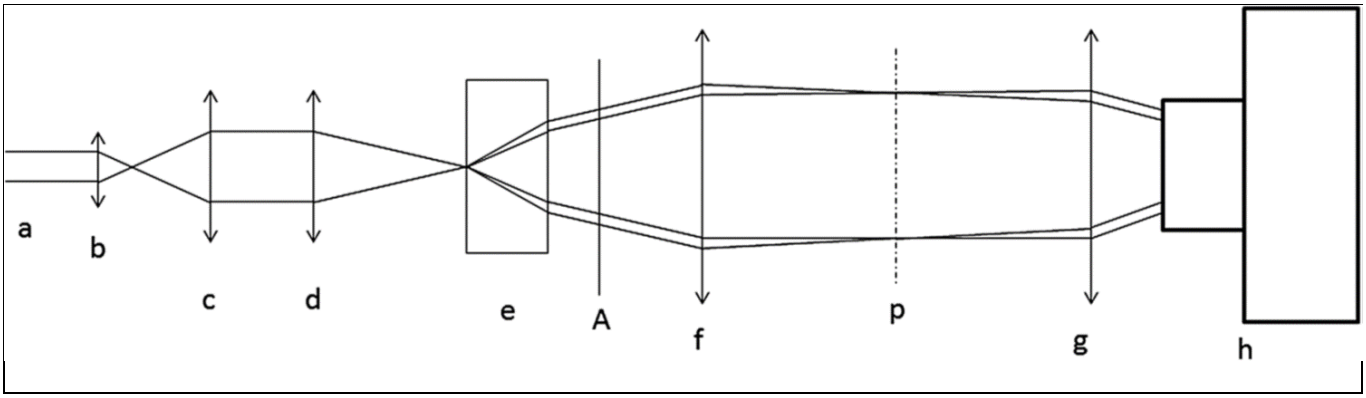

Fig. 4. 4- Modified laser conoscopy lay-out. In this system, the ground glass, previously in P, has been substituted by the lens (g) placed at its focal distance from P. This lens makes parallel the diverging rays from P and directs them to the camera lens (h) focused to the infinity so to get the interference ion its sensor.

4.2 Laser Conoscopy: observation orthogonal with respect to the optic axis

The aim to enlarge the possibilities to achieve a complete characterization of the birefringent media, prompt the necessity to analyze the crystal not only along its optic axis.
In this phase, observations and analysis orthogonal to the optic axis have been carried out. The typical interferogram acquire by observing in this direction are shown in the Fig. 4.5.

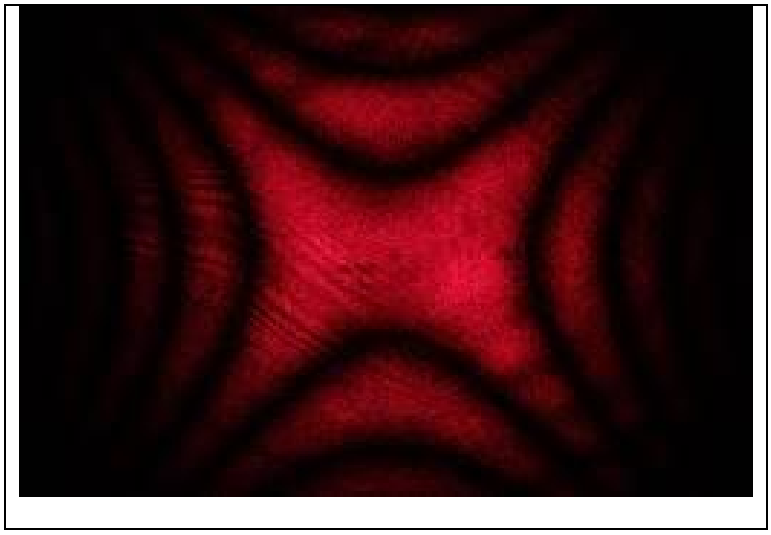

Fig. 4.5 Typical fringe pattern of a PWO observed orthogonally to the optic axis. The shape of the fringes resembles to a series of Hyperboles.

The different shape of the fringes has required a change in the interpretation since no ellipses or circle are recognizable in the images.
The outcome of this first attempt is the definition of a characteristic feature, of the conoscopic images, which gives a reliable evaluation of the crystal state variation from point to point.

4.2.1 Analyzing the model

In the "crystal optic" section, it has been outlined how the fringe pattern can be considered the intersection between the Bertin surfaces (iso-delay curves) and planes which represent the crystal geometrical edge surfaces.
The presence of stress induces a biaxial behavior and a variation of the angle β (the semi-angle between the optic axes). Therefore, the Bertin surfaces and the relative fringes will mutate, as it has been stated in the chapter 3.
By the relations in [13] expressed in the chapter 2 and the model developed in [26] and [27] an analysis has been carried out to predict the behavior of the fringe pattern with respect to the stress variation.
The trace of the intersection between the Bertin surfaces and a plane parallel to the optic axis are quartic curves (Fig. 4.6, see chapter 2 and [26], [27]).

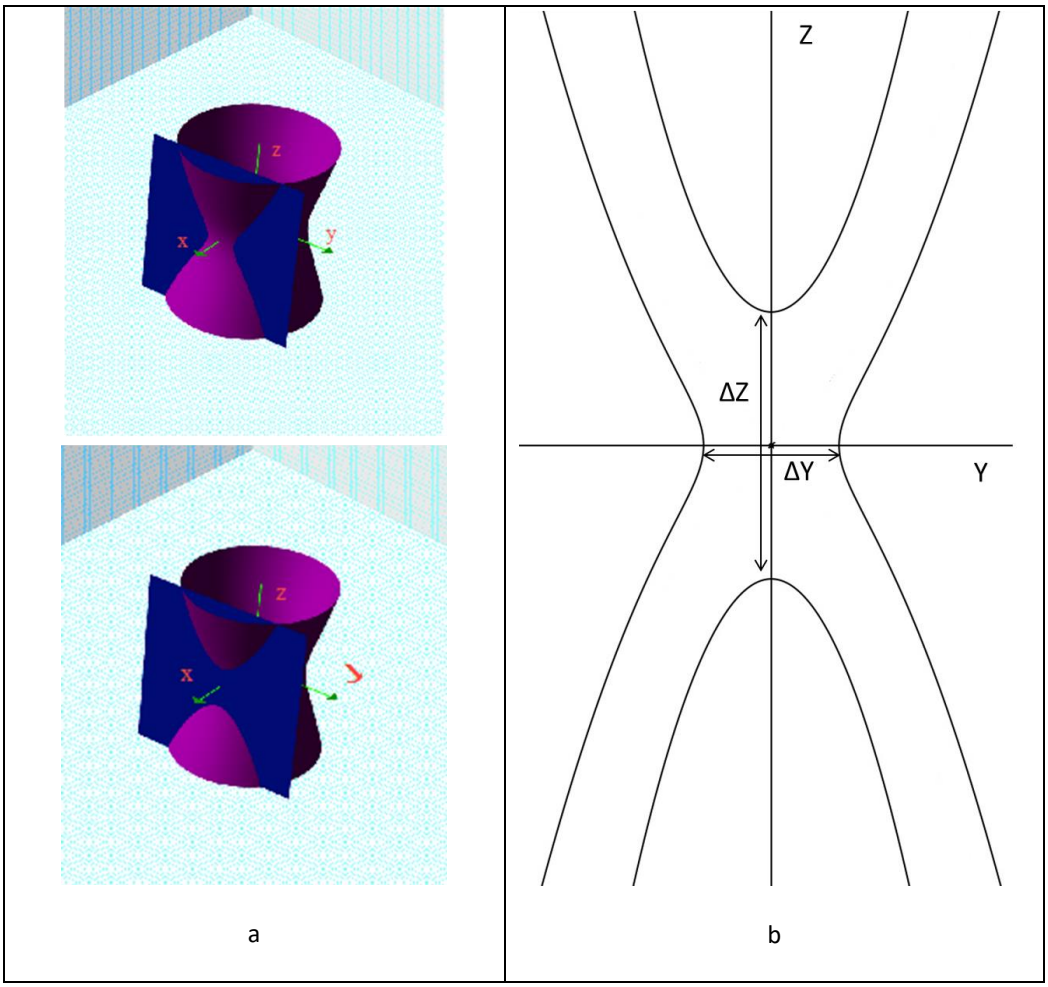

Fig. 4. 6 In the image (a) the intersection of the Bertin surfaces with a plane parallel to the optic axis is represented. Since the fringes are due to the intersection of two different orders of the Bertin surfaces, in the image (a) the intersections are presented separately to have a clearer view of the phenomenon. In (b) the resulting curves which represent the relative fringe pattern expected. In (b) the distances ΔZ and ΔY are indicated. Those measurable features are used to have a numerical indication of the crystal state.

In the case, the fringe pattern is composed by two different orders which intersect respectively the Z and the Y axis as it is represented in Fig. 4.18. Characteristic features of the figure are the distances ΔZ and ΔY reported in the Fig. 4.18b.
These features will variate as the angle β changes with respect to the stress state; the difference R= ΔZ – ΔY is a measurable quantity and can be considered representative of the crystal state and its variation.
By the model in [26], in [27] and the eq. 2.37 to 2.44 in the chapter 2, the expression for the Bertin surfaces can be rearrange as [27] (eq. 4.2):

$$\cos^4\beta x^4 + y^4 + \sin^4\beta z^4 + 2\cos^2\beta x^2 y^2 + 2\sin^2\beta z^2 y^2 - 2\cos^2\beta \sin^2\beta z^2 x^2 - N^2H^2\left(z^2 + y^2 + x^2\right) = 0 \qquad \text{(eq.4.2)}$$

Where $H = \dfrac{\lambda}{n_e - n_o}$ (eq. 4.3)

By the equation (eq. 4.3), considering x=d the Fig. 4.6b can be obtained. The expression of ΔZ and ΔY can be achieved with some simplification in the case of compressive stress ($z^4\sin^4\beta \rightarrow 0$) and represented as (eq. 4.4 and eq. 4.5):

$$\Delta y = \sqrt{2}NH\sqrt{1-2\left(1-\sin^2\beta\right)\xi^2 \pm \sqrt{1+4\xi^2\sin^2\beta}} \qquad \text{(eq. 4.4)}$$

$$\Delta z = 2d\sqrt{\frac{\cos^4\beta\cdot\zeta^2-1}{2\sin^2\beta\cos^2\beta\cdot\zeta^2+1}} \qquad \text{(eq. 4.5)}$$

Where $\xi = \frac{d}{NH}$ (eq. 4.6)

The expression (eq. 4.4) and (eq. 4.5) are carried out respectively with z=0 and y=0 and considering that the order N must be different for the two equations. Since the eq. 2.33 can be rearrange to carry out the following expressions (eq. 4.7 and eq. 4.8):

$$\cos\beta = \sqrt{\frac{B_2 - B_3}{B_1 - B_3}} \qquad \text{(eq. 4.7)}$$

$$\sin\beta = \sqrt{\frac{B_1 - B_2}{B_1 - B_3}} \qquad \text{(eq. 4.8)}$$

The trend of the difference R with respect to $sin^2\beta$ (linked to the stress distribution) can be carried out (reported in the graph (Fig. 4.7).

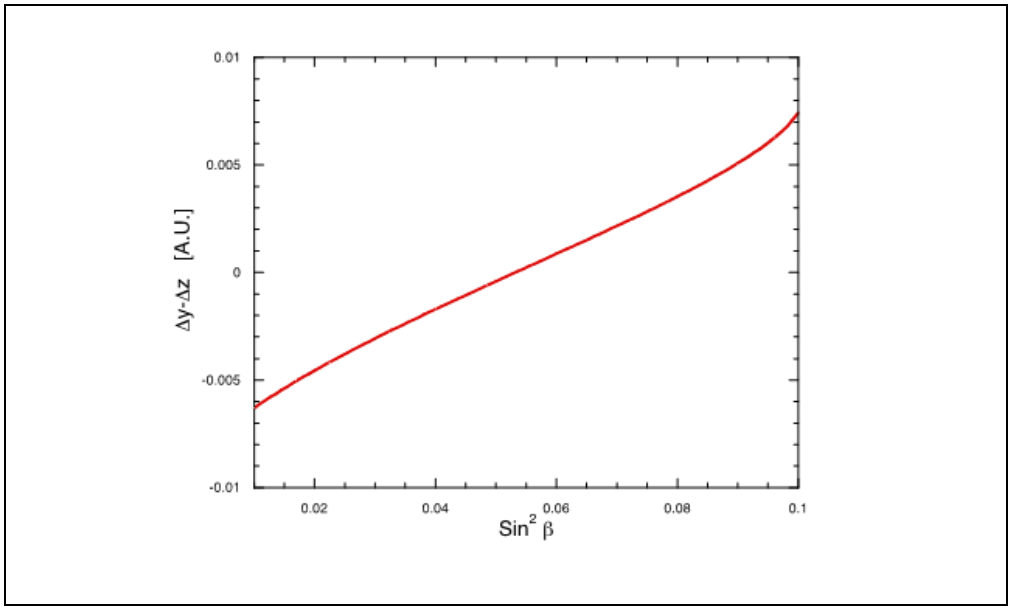

Fig. 4. 7 The graph represents the variation of the measurable difference R=ΔY-ΔZ as a function of *sin² θ*. The value of *sin² θ* is directly correlated to the stress condition. Therefore, this measurable difference gives an indication about the stress distribution over the sample.

Since $sin^2\,\beta$ is a function of σ_y, σ_z by the piezo-optic π matrix, the quantity R= Δy-Δz can be used as indirect measure of the internal stress. The quantity Δy-Δz is locally linearizable as a function of $sin^2\,\beta$ but carefully.

A Research, carried out on tetragonal crystal, is ongoing; hereafter, some considerations are reports (as an insertion) which will be completed in a forthcoming paper, that needs of a deeper investigation.
By the piezo-optic relation (eq. 3.33), ruled by the π matrix, $sin^2\,\beta$ can be expressed as (eq. 4.9):

$$\sin^2\beta = \frac{\pm\sigma_y D(\pi)}{\Delta B + \sigma_y G_{\pm}(\pi) + \sigma_z H(\pi)} \qquad \textit{(eq. 4.9)}$$

Expanding in Taylor series $sin^2\beta$, considering that it is possible consider

$$|\Delta B| >> |\sigma_y G_{\pm}(\pi) + \sigma_z H(\pi)| \qquad \textit{(eq. 4.10)}$$

where $G_{\pm}(\pi)$ and $H(\pi)$ are functions of the elements of the tensor π.

We obtain, in term of the dimensionless parameter $\upsilon = \frac{\sigma_y G_{\pm}(\pi) + \sigma_z H(\pi)}{\Delta B}$

$$\sin^2\beta = \frac{\pm\sigma_y D(\pi)}{\Delta B}\left[1 - \upsilon + \upsilon^2 + o(\upsilon)\right] \qquad \textit{(eq. 4.11)}$$

From (eq. 4.11), at the first order $sin^2\beta$ depends linearly from $\boldsymbol{\sigma_y}$. The dependence from $\boldsymbol{\sigma_z}$ happens only at higher orders. It seems that the measure of R is particularly sensitive to the stress component $\boldsymbol{\sigma_y}$.
In the case of tensile stress the results are similar and at the end we obtain

$$R(\sigma_y, \sigma_z) = k_0 + k\sigma_y + o(\sigma_y, \sigma_z) \qquad \textit{(eq. 4.12)}$$

Further studies are ongoing.

An improvement of the model is still ongoing but, anyway, the measurement of the difference R is a reliable method to evaluate the distribution of the internal stress in the birefringent media.

Summarizing, the controlled Laser Conoscopic technique has increased the sensitivity and improved the spatial resolution. Moving the analysis along the *a* crystallographic axis, traditionally not yet extensively studied, has extended the tools for a more complete characterization.
These precise and accurate techniques can be exploited not only for a correct evaluation of the crystal stress state but for improve the material behavior knowledge.
For example, a correct evaluation of the ellipticity and the photoelastic constants, leads to a correct definition of the piezo-optic parameters, as in the research conducted in [26] and [27] on tetragonal crystals, by means of:

$$C = \frac{\sqrt{4\pi_{61} + (\pi_{11} - \pi_{12})}}{B_x - B_z}\left(1 + \frac{2K^2}{1 + \sqrt{1 + 4K^2}}\right)(\sigma_y - \sigma_x) \quad \text{(eq. 4.13)}$$

$$f_\sigma = \frac{\sqrt{4\pi_{61} + (\pi_{11} - \pi_{12})}}{B_x - B_z}\left(1 + \frac{2K^2}{1 + \sqrt{1 + 4K^2}}\right) \quad \text{(eq. 4.14)}$$

Where $K = \frac{d(n_e - n_o)}{\lambda}$ and the π coefficients are components of the piezo-optic matrix.

Aiming to a general law as the eq. 4.15 [27]:

$$C(n_i, n_j) = f_\sigma \backslash (\sigma_i - \sigma_j) \quad \text{(eq. 4.15)}$$

generalizing the Brewster law [12] to the anisotropic tetragonal anisotropic crystals.

4.3 Sphenoscopy

Fundamental changes in photoelasticity are proposed in this section, from the methodological and conceptual point of view, to meet some needs raised by the use of Laser conoscopy.
Laser Conoscopy is an extremely spatially resolved and accurate technique. On the other hand, since it provides a punctual inspection, number of points must be inspected to assess the entire volume of a crystal sample. This produces a large set of data not always necessary, depending on the level of detail needed.
Moreover, a great effort has to be done in the interpretation of the fringe pattern when the observation is carried out not along the characteristic axis, even if the stress is uniform (e.g. if the sample is randomly cut with surfaces not orthogonal or parallel to the axes).
While, in Laser Conoscopy the light spans in a solid cone, generating a conic probe volume (Fig. 4.2), in the sphenoscopic technique the light spans in a plane angle (Fig. 4.8a).
By this, the fringes, derived by the Bertins surfaces, are not completely generated. Therefore, just one dimension of the orders is produced as it is highlighted in the Fig. 4.8b [40].

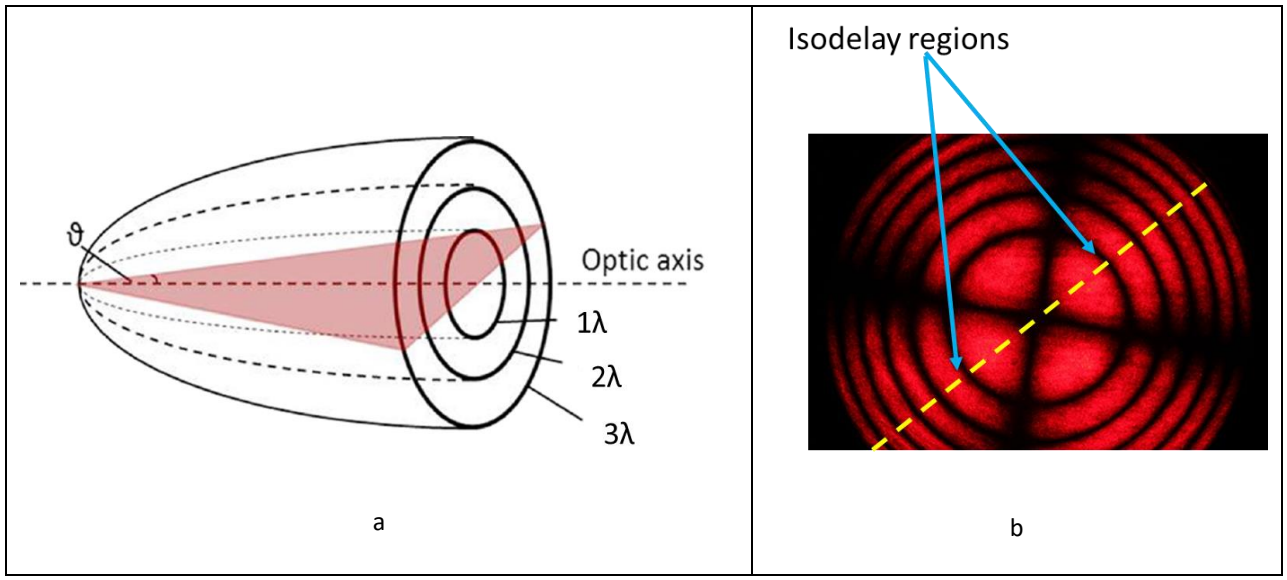

Fig. 4. 8 A schematic representation of the sphenoscopic principle. The light spans in a plane angle creating a plane of light (a). The fringe orders derived by the Bertin surfaces are not completely formed. In fact, since the triangular light plane intersect the Bertin surface in one dimension, only that dimension will be generated and the isodelay curves turn into isodelay points or regions (b).

By the superposition of several planes like in Fig. 4.8a, a wedge (In ancient Greek, wedge is translated as “sphenon” and to observe is “scopeo”, from which the term sphenoscopy = observation by a wedge) of light is generated.
The light wedge can be obtained by substituting, in the conoscopic set-up, the spherical lens with the cylindrical one (Fig. 4.9a).
The light is, therefore, focused on a line and the probe volume is a wedge which can cover an entire dimension of a sample (Fig. 4.9b) [40].
The fringe pattern, presented in the Fig. 4.9c, is composed by the envelope of one dimension of the conoscopic fringe orders, piled up along the wedge height.

By the model in [20] (eq. 2.44 and 2.45) the one-dimensional expression can be achieved as [40]:

$$H^2(n_x)N^2(x^2 + z^2)(1 + tg^2\beta)^2 = (x^2 - z^2tg^2\beta)^2 \qquad \text{(eq. 4.16)}$$

Considering a uniaxial crystal not stressed ($\beta=0$) that equation leads to the 3D model in Fig. 4.9d. That model can be considered as the Bertin surfaces generated by Sphenoscopy. Each plane of light, which composes the light wedge, generates a trace of the iso-delay curves (Bertin surfaces) according to the eq. 4.16; the simulation in Fig. 4.9d is the superposition of several traces along y (the hypothetical height of the sample).

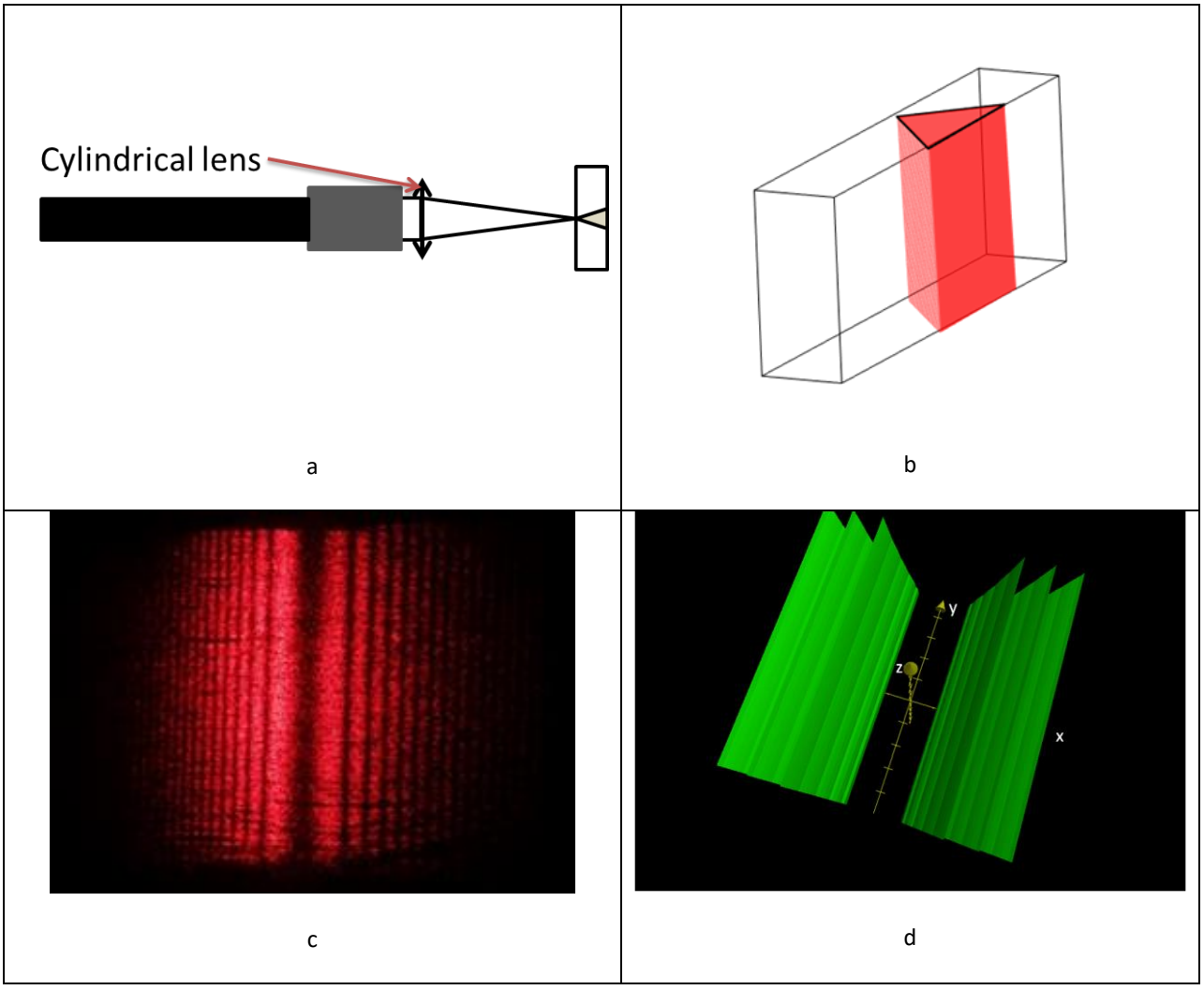

Fig. 4. 9 The system with the cylindrical lens (a). After the magnification of the beam (a) the cylindrical lens generate a wedge-shaped probe volume in the sample (b), which can cove an entire dimension of the geometry. The resulting fringe pattern is composed by lines (c) which represents the envelope of the generated dimension of the conoscopic pattern, over the wedge height. In (d) a simulation of the Sphenoscopic Bertin surfaces for a uniaxial crystal is presented.

As it is clear from the eq. 4.16, the model works also for biaxial crystals in which the semi-angle β is not zero.

The pattern, carried out by Sphnoscopy, is obtained by intersecting the “sphenoscopic Bertin surfaces” with a plane (e.g. z=d the thickness of the sample). Therefore, line shaped fringes will compose the resulting interferogram (Fig. 4.9c).
Straight lines are achieved whatever the direction of observation is, if the area observed is homogenous and free of defects. This leads to a simplified interpretation of the pattern: the presence of a residual stress distribution or defectiveness is revealed by a change in the distances between the lines and in their curvature. Moreover, even though it gives less number of details, Sphenoscopy is a field technique and provides a faster inspection; in fact, the line inspected by one sphenoscopic acquisition requires numbers of conoscopic images to cover the same area.

4.4 Fringe analysis algorithms

4.4.1 Laser Conoscopy – observation along the optical axis

Thanks to the light coherence and the reduction of the probe volume, a local inspection is achieved. The enhanced sensitivity and spatial resolution lead to the necessity of efficient and reliable tools so to analyze the large number of conoscopic fringe images carried out by the method.
It has been clarified that, even if a stress distribution is present in the material, the expected shapes of the first fringe order are ellipses or circle. Therefore, the goal of the developed algorithm is to find the best ellipse that fits the shape of the first fringe order [33].
That algorithm can be considered composed of four phases listened below:

1. Autonomous recognition of the region of interest (ROI): this part is crucial to reduce the involvement of the operator in the analysis of large number of images.
   In this step, the pattern matching technique [36] has been exploited.
   A suitable pattern is usually carried out by selecting specific features of the images (Fig. 4.10a). The algorithm superimposes that pattern to the series of images so to individuate the ROI (Fig. 4.10b and c).

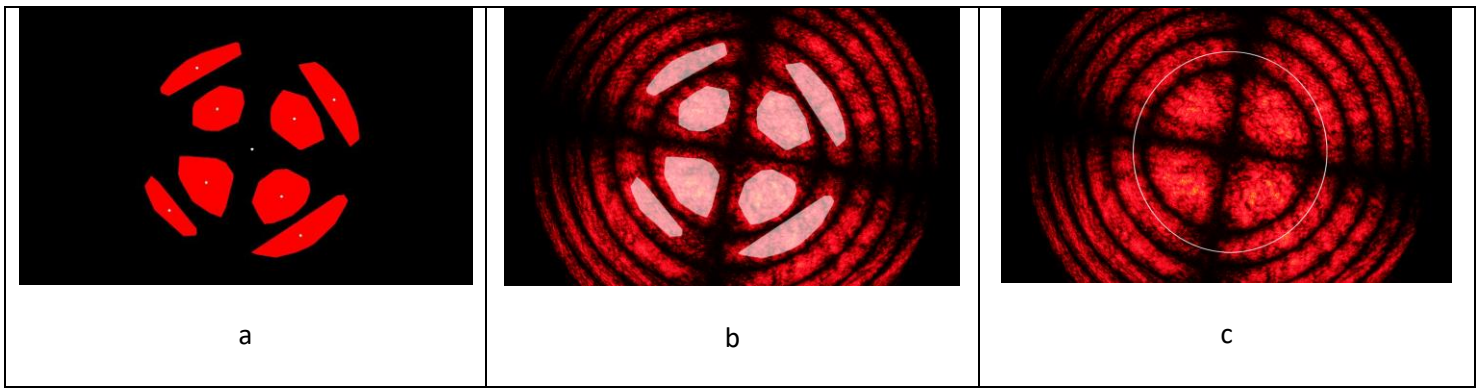

Fig. 4. 10-Pattern matching technique to recognize the ROI autonomously. In (a) the proposed pattern extrapolated by typical features of the conoscopic images. Superimposition of the pattern (a) on the area of the image with the highest score (b). (c) Definition of the ROI.

2. Image processing. Since the light laser is exploited by the methods, the conoscopic images are affected by speckle noise; by the enhanced sensitivity, the images are affected by surfaces damage (scratches, chipping and polishing quality). In this part, filters and algorithms (typical in the image processing techniques) are exploited so to make the pattern suitable for the analysis [33].
   A color plane extraction is the beginning of this step. The red plane is extracted in the case due to the He-Ne laser source. The algorithm operates on the gray-scale image using a lookup table to increase the contrast (Fig. 4.11a and c). This phase ends with the application of a median filter to the image, as in [19][37]. Erode and dilate algorithms [37][38] in conjunction with that low-pass filter allows to obtain an image with considerable noise reduction without significant alterations of the features (Fig 4.11b and d). Speckle noise is, then, reduced and the edges of the fringes became smoother. The dimensions and the shape of the filters must be chosen considering the acquisition parameters, the dimension of the image and its resolution.

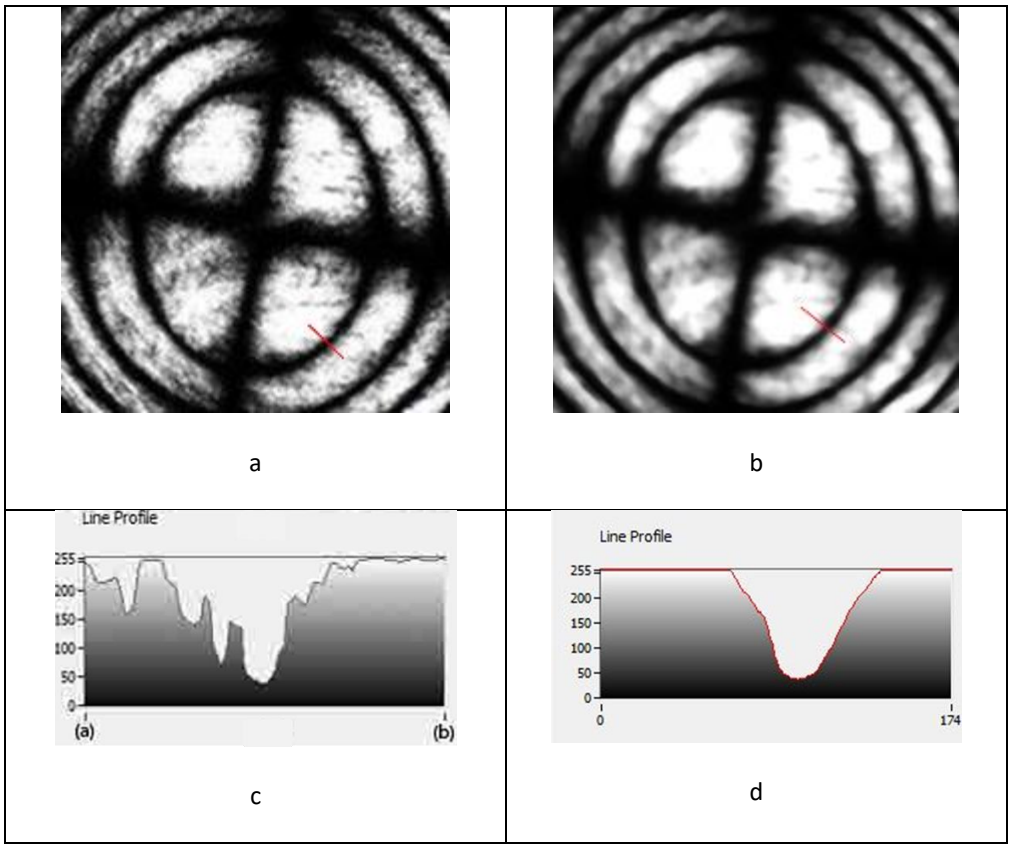

Fig. 4. 11 In (a) the conosopic image after the color extraction (gray scale). In (b) the enhanced image. In both the images has been extracted the intensity line profile, (c) and (d), of the red segment which crosses the fringe order. In the smoother line profile (d), finding the correct position of the minimum is easier.

3. Image analysis: in this part, the algorithm fits an ellipse in the first fringe order. The outcome is the analytical expression of that ellipse.
   Straight lines are traced from the center of the ROI to its boarder. Each line profile intensity is interpolated with a polynomial function and the position of the minimum is evaluated. The ellipse is fitted by the algorithm through those points, using the minimum squared error method (Fig. 4.12a) [36].

4. Optimization of the results: in this last phase, number of ellipses are generated close to the first one. The aim is to find the ellipse with the lowest light intensity on its boarder. From the expression of this ellipse, the ellipticity ratio will be calculated.
   The five parameters of the ellipse, (1) the x coordinate of the center, (2) the y coordinate of the center, (3) length of the major axis, (4) length of the minor axis, and (5) angle of rotation with respect to the horizontal line, are randomly variated so to generate numbers of ellipses (Fig. 4.12b). Finally, from the lowest intensity ellipse the *C* ratio is extrapolated [33].

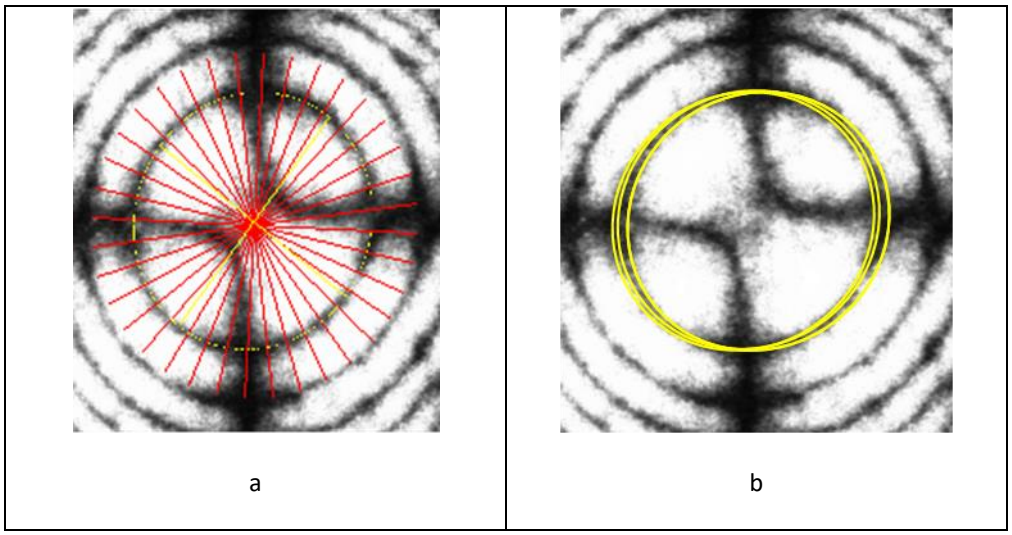

Fig. 4. 12 – Once the ROI is defined, segments are traced from its center crossing the first fringe order (a). In each segment the position of the minimum intensity is carried out and a first ellipse is fitted by them (a). Close to that ellipse, number of ellipses are generated randomly so to find the one with the lowest intensity on its boarder (b).

To be sure that the first fringe order can be approximate with an ellipse, the R^2 value is considered. If that value is higher than 0,88, the fit is accepted otherwise is rejected. If R^2 is lower than 0,88, then the fringe order can not be considered an ellipse anymore. In fact, beyond that limit the ellipticity is not linear with respect to the increasing load: the fringe order has to be fitted with a quartic curve (Cassini-like curve).
From our tests, the measured ellipticity ratio *C* has an uncertainty [39] of 0.006, using about 4 times the erode and dilate filters, a 40x40 median filter and 1000 optimization iterations with a 18Mpx camera (in our tests, the range of ellipticities goes from 0 to 0.4). Actually, a reduction of a factor 3 of the initial uncertainty has been achieved.

4.4.2 Laser Conoscopy: observation orthogonal to the optic axis

The same strategy has been used to analyze the images carried out observing along the *a* axis. The same steps for the image processing are used in this case.
Instead of ellipses, hyperboles have been fitted by the position of the minimum intensity points in the fringes (Fig. 4.13).

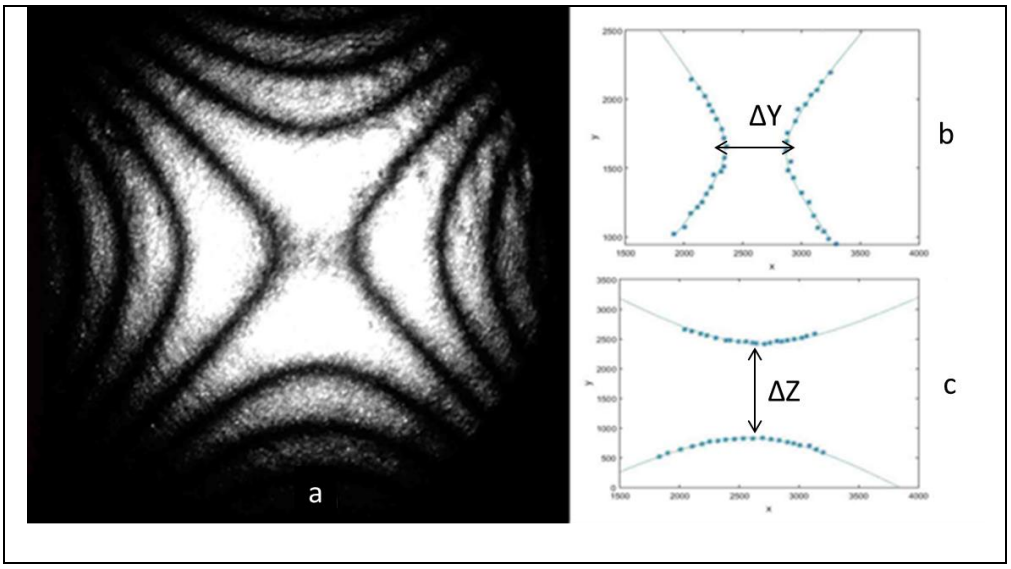

Fig. 4. 13 The processed image (a). In (b) and (c) the fitted hyperboles are shown. The algorithm fits the hyperboles by the minimum intensity points ~~in~~ on the fringes, in a separate way to easily calculate the distances ΔZ and ΔY.

The distances between the tip of the hyperboles branches are evaluated so to get the difference R =Δy-Δz which, according to the model, gives a good evaluation of the crystal state.

4.4.3 Sphenoscopic fringe patterns

Since the images are affected by the same phenomena as Conoscopy, the acquired images are processed in the same way so to be suitable for the analysis. In case of sphenoscopic fringe images, the actual algorithm evaluates the distance between two fringes included in a squared ROI (Fig.14). In the ROI, number of lines are traced in order to evaluate the distances between the minimum points in each line at different heights of the wedge (Fig. 14).
Further developments are aimed to evaluate the curvature of each fringe so to give the possibility to have complete analysis of the pattern.
The case in Fig.14 represents the analysis of a sphenoscopic pattern acquired along the *a* crystallographic axis.

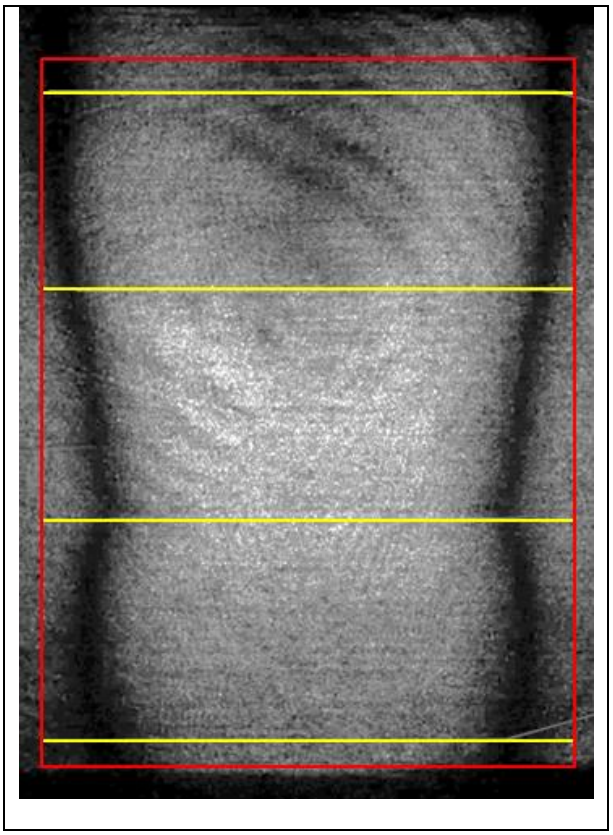

Fig. 4. 14 The image presents the analysis of a fringe pattern acquired by Sphenoscopy along the *a* crystallographic axis. The squared ROI (in red) comprehends the needed fringes. The lines (in yellow) allow to calculate the distance between the fringes at different heights by the position of the minimum intensity points in each line. Once the location of those points is obtained, the analysis of the curvature is also possible.

4.5 Experimental validation and results

Here the tests to validate the methods and the techniques are reported. Those tests have proven in a qualitative and quantitative way the reliability of the developed methods.

4.5.1 Laser Conoscopy along the optic axis: tests and validation

Tests have been carried out in order to validate the technique. A sample of PWO uniaxial crystal (prismatic sample with dimensions of 60 × 15 × 10 mm Fig 4.17a) has been observed along its optic axis in unloaded condition and with an induced stress distribution by means of the four-point bending test. The analysis has been carried out by measuring the ellipticity of the first fringe order and its angle of rotation with respect to the horizontal X axis (Fig 4.15) [34].

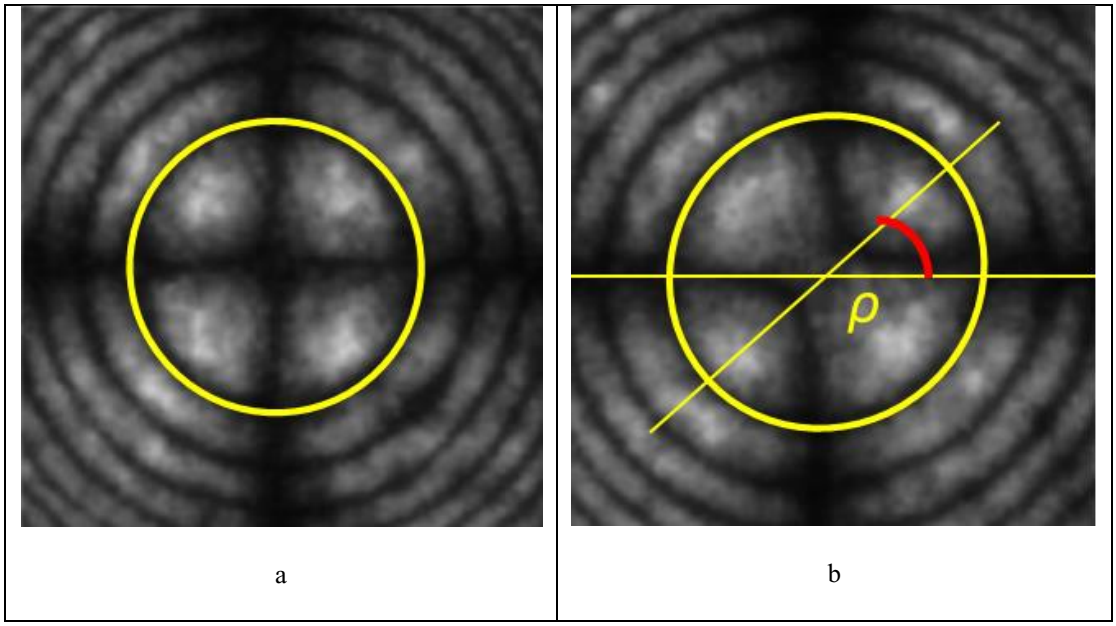

Fig. 4. 15 In the image are represented the unloaded condition of the fringe pattern (a) and the stressed one (b). While in (a) the first fringe order is a circle, in (b) it has an elliptic shape with a certain angle of rotation (ρ) with respect to the horizontal X axis. The latter is measured in conjunction with the ellipticity so as to evaluate the local stress condition.

4.5.1.1 Unloaded conditions

By changing the lens focal length (Fig. 4.1 and 4.4 d) or adjusting the beam expander magnification (lens system b c in Fig. 4.4), the solid angle of the probe volume can be managed so to variate the number of fringe orders. In Fig. 4.16, the fringes orders variate accordingly with the eq. 2.37.

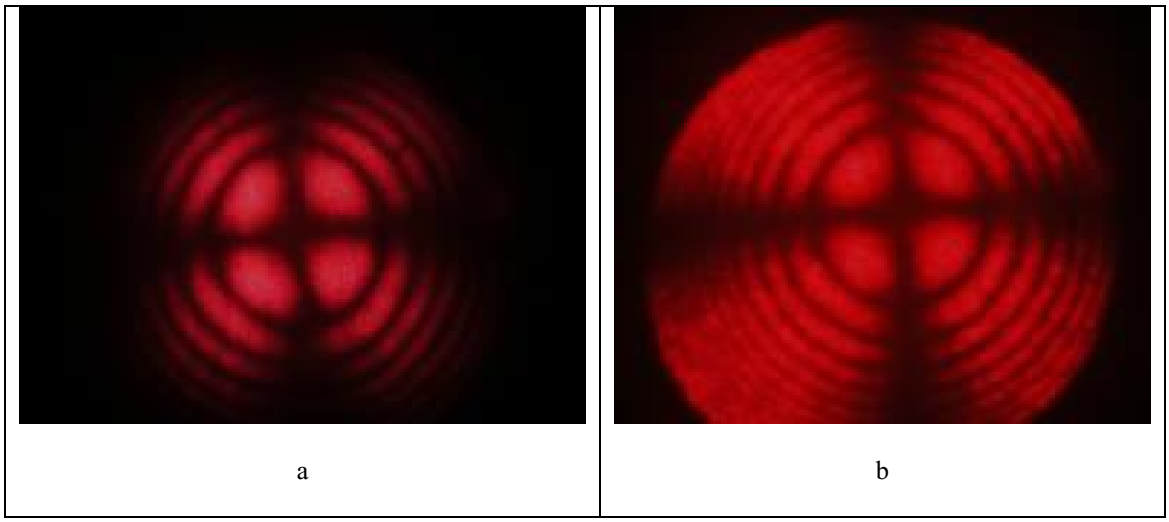

a b

Fig. 4. 16 In the image are represented the fringe pattern due to the same point of inspection but with different solid angle of the probe light cone. In (a) the aperture is about 10 deg, in (b) about 25 deg.

The impinging light cone on the inlet surface of the crystal has been variated respectively from 10 deg (Fig. 4.16a) to 25 deg (Fig 4.16b) [33].

In unloaded condition, the sample has been scanned along its height (the Y axis). Three sets of observations have been performed observing 10 mm in the middle area, starting from the bottom edge with 0.1mm step (Fig. 4.17b). Therefore 300 conoscopic images have been carried out.

The trend of ellipticities reveals a classical parabolic progression of the residual stress [34] along the scanned line (Fig. 4.17c). It is worth to emphasize that, with the diffused light polariscope, a unique image is acquired for the entire area losing the sensitivity to the residual condition.

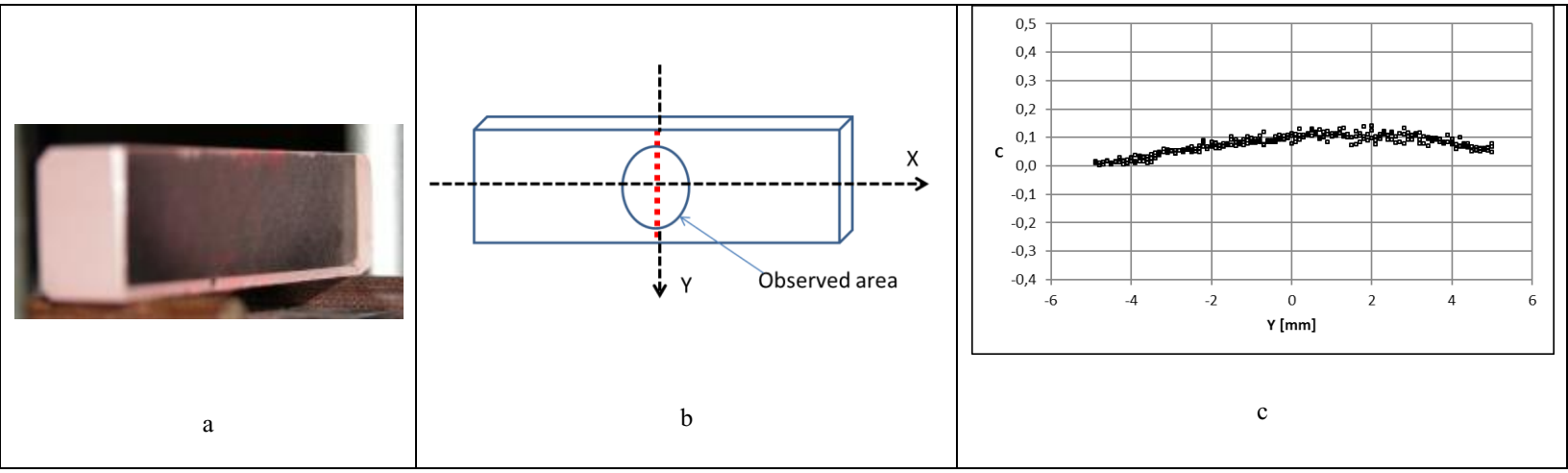

a b c

Fig. 4. 17 The inspected sample is shown in(a). (b) Is the schematic representation of the observed area of the crystal. In (c) the detected ellipticities along over the observed area are reported. A residual stress condition has been recognized as it is evident by the graph (c).

4.5.1.2 Loaded condition by four point bending test

With the classical four-point bending set up [30], a known stress distribution has been induced to the uniaxial sample so to achieve a validation and a calibration too. In Fig. 4.18 are reported the scheme of the test and the resulting stress distribution.

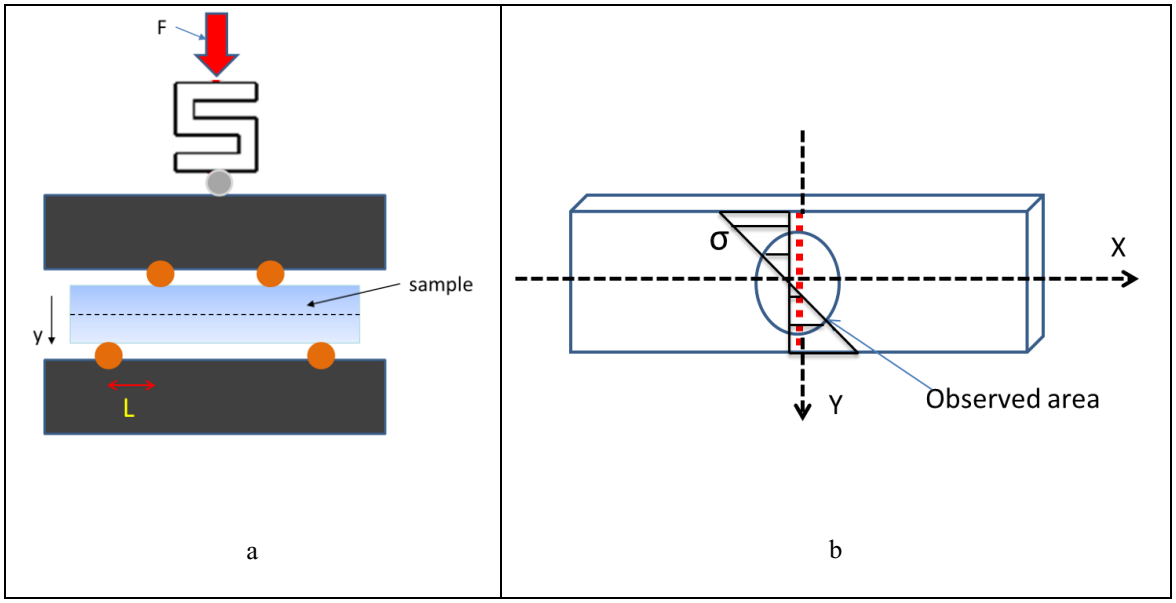

Fig. 4. 18- in (a) the loading scheme of the four-point bending test is presented. F is the loading force. In (b) the antisymmetric distribution of σ_x over the Y axis is highlighted. The distribution variates with respect to Y by the Navier relation $\sigma = \frac{FL}{2J} Y$ where J is the moment of inertia.

By means of this well know mechanical test [30] the induced load σ_x is linear with the Y axis and it is evaluated by the classical Navier formula [29]:

$$\sigma = \frac{FL}{2J} Y \qquad \text{(eq. 4.17)}$$

Where J is the moment of inertia.

4.5.1.2.1 Assessment of the local inspection

In this observation, the capability to discriminate the stress variation, performing a pointwise inspection has been tested [34].
The laser light has enhanced the sensitivity providing coherence and the possibility to minimize the probed volume. In fact, the local inspection is achieved, mostly, by this latter possibility.

The dimension of the probed volume has been variated during the test; in the first observation, a larger part of the sample has been illuminated by putting the sample out of focus. In the second, the tip of the light cone was exactly at the inlet surface [33], minimizing the probe volume (Fig. 4.19).

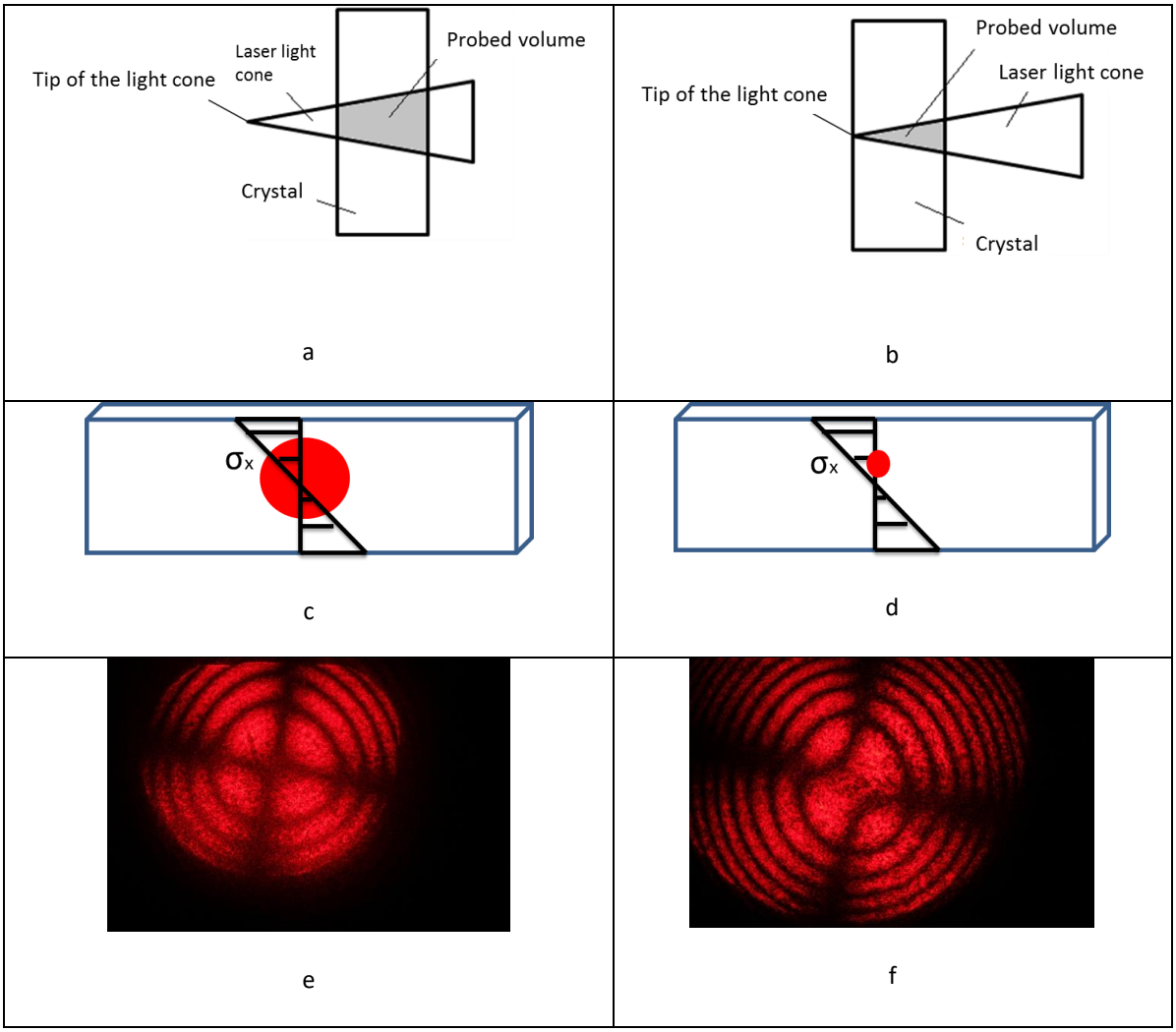

Fig. 4. 19 In (a) and (b), the different dimensions of the probed volume are schematically represented, in different positions of the sample with respect to the focal point. (c) and (d) are the relative inlet spot, it is clear how enlarging the volume a larger part of the stress gradient is involved in the probed volume. With the larger volume (a) the fringe pattern observed is in (e) (pear like shaped), while with the pointwise inspection the pattern became like in (f). Since in the smaller volume the stress can be considered uniform, the pattern is elliptic shaped. The latter leads to an easier reconstruction of the stress gradient

In the Fig. 4.19 are reported the schemes of the observations made with the different dimension of the proved volume and the resulting fringe images.

The scheme (Fig. 4.19a) shows how the probed volume is enlarged. The inlet spot is higher dimensioned by putting the crystal far from the focal point (beam waist). A large part of the sample volume is illuminated; that volume comprehends a larger part of the induced stress gradient (in the Fig. 4.19c is schematically represented the larger part of the antisymmetric distribution of σ_x included in the probe volume, in this test the diameter of the spot is about 10mm).

The resulting pattern is similar to the one carried out by the diffuse light polariscope [20] (Fig. 4.19e) (see section 3 Fig. 3.). Therefore, it is difficult to extract the exact distribution of the load by the complex shape of the pattern.

The light spot at the focal point, ideally, is considered a dimensionless point; actually, it is a small circle called the beam waist and its dimension depends on the characteristics of the optics, the wavelength, and the dimensions of the cylindrical beam that hits the focusing lens. In our experiment, the laser beam waist has a diameter largely minor of 0.1 mm; if the beam waist is coincident with the crystal surface, the probe volume is minimized.
This is represented in Fig. 4.19; in Fig. 4.19d it is highlighted how the minimized spot comprehends a smaller part of the stress distribution.
In the resulting image, in Fig. 4.19f, the pattern is composed by ellipse shaped fringe orders due to the fact that the volume has dimension in which the stress can be considered homogeneous and uniform (the dimensions are smaller than the smallest stress variation perceptible).
Therefore, a local inspection is possible and a correct reconstruction of the stress distribution is achievable, as clarified in the next paragraph.

4.5.1.2.2 Detecting the stress distribution

In the same area considered in the unloaded test, an inspection has been carried out scanning point by point 10mm of the sample height with the minimized probe volume so to achieve the appropriate sensitivity and spatial resolution.
The vertical line has been covered with a step of 0.1 mm. Each point has been observed three time (the distribution of the residuals has been assessed by a normality test, see [34]).
The raw values of ellipticity C and angle of rotation ρ are reported in Fig. 4.20. The "V" shape of the ellipticity, as shown in Fig. 20a, is due to the insensitivity of the model to the sign of σ.

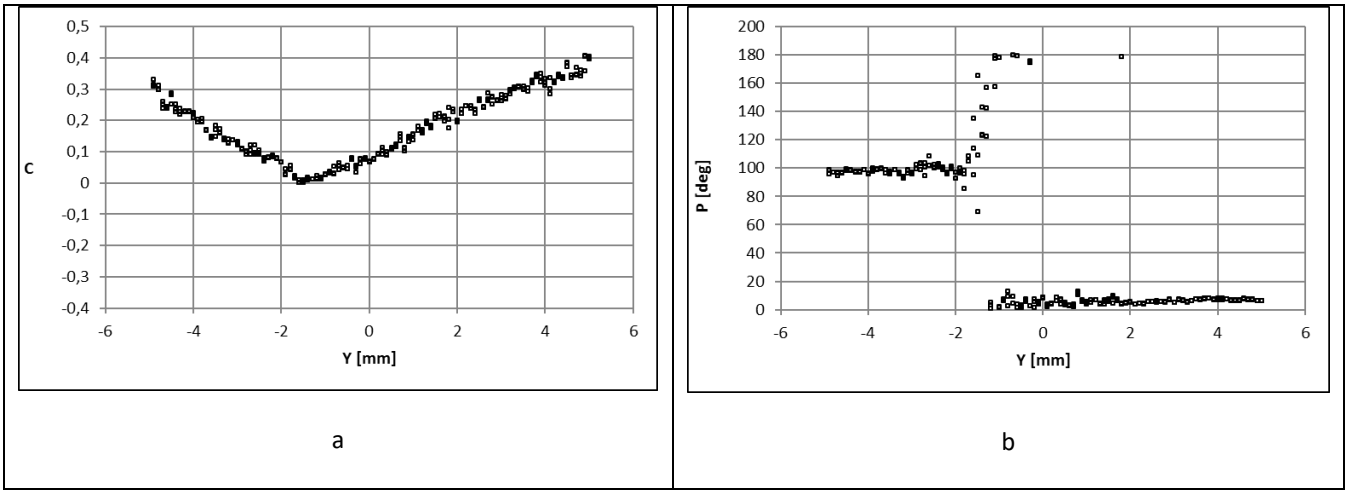

Fig. 4. 20 the detected ellipticities in bend condition (a) with the relative tilt angle (b) with respect to the horizontal X axis. The V shape of (a) is due to insensitivity of the model to the sign of the load. By the angle of rotation (b), a sign can be given to the ellipticities, and the direction of the principal stress can be detected. In the area between -1mm and 0mm the allipticity is close to 0 so the uncertainty is higher. Therefore, the flipping angle in that area, from 0° to 180°, practically describes the same ellipse.

Meaningful examples of the fringe pattern images carried out in the test, are shown in the Fig. 4.21. By the methodology, no complex fringe patterns are expected and it is possible to recognize the different stress condition areas. In fact, the no stressed area is detectable by the circular shaped fringe pattern (absence of ellipticity Fig. 21b) [34]. Tensile and compressive areas are indicated by the elliptic fringe pattern and their rotation angle (respectively orthogonally rotated, Fig. 11a and Fig. 21c).

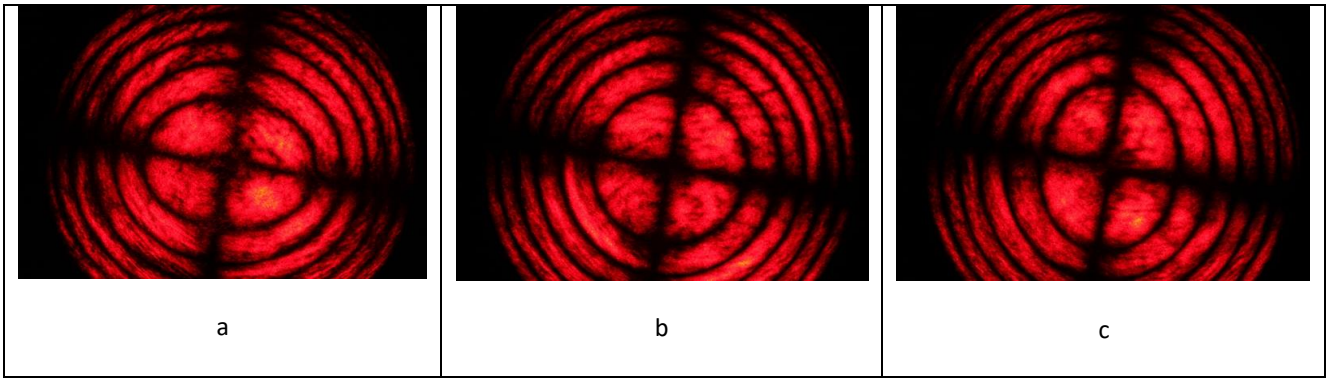

Fig. 4. 21 Three representative images carried out in bending condition. (a) is due to the tensile area of the sample, (b) to the stress-free area and (c) to the compressive one. (a) and (c) are orthogonally rotated. The direction of the principal stress direction can be evaluated by this angle.

Therefore, it is possible to recognize the sign of σ (with the convention: positive for tensile and negative for compression) is given from the tilt angle (Fig. 20b), considering that, in a more general case, the ellipse rotation follows the principal stresses direction and orientation [34].
In the following image (Fig. 4.22a) the reconstructed data about the ellipticity C are reported. It is possible to notice that the resulting trend is due to the composition of the residual stress trend and the induced one. Therefore, the data are well represented by a second order polynomial. Subtracting the data from the unloaded condition, the expected linear trend is achieved (Fig. 4.22b). The mean values of each point of the two analysis have been subtracted to carry out that results.

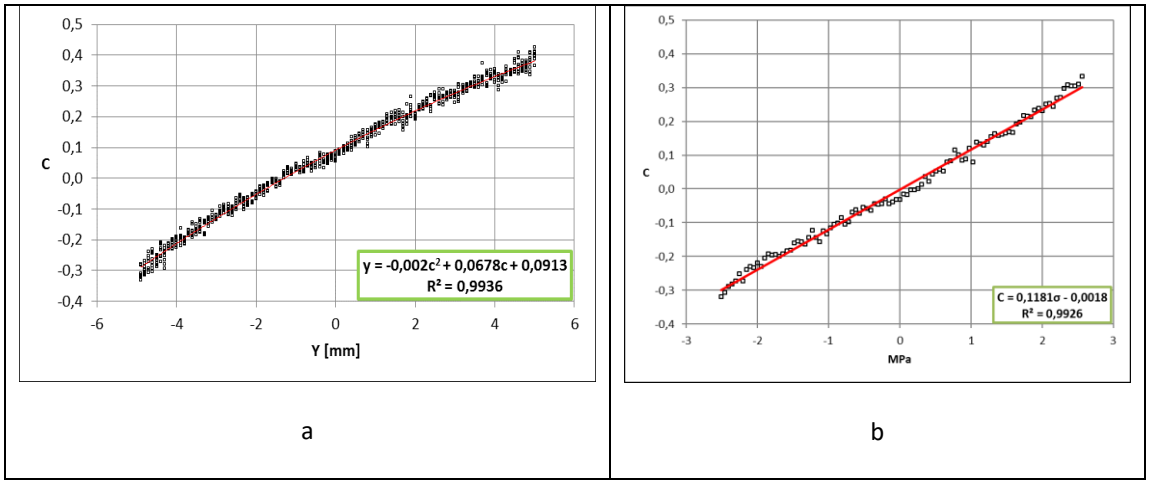

Fig. 4. 22 In the graph (a) are the reported the detected ellipticities values with the sign evaluated by the tilt angle. The graph in (b) has been carried out by the subtraction of the residual stress ellipticities values detected in unloaded condition from the values detected in bent condition so to achieve the ellipticity values related to the induced distribution.

By the data, the photoelastic constant $f\sigma$ has been evaluated and the inducted trend of load has been correctly reconstructed (Fig. 4.23a). In the Fig. 4.23b, the values of the residual stress are represented, evaluated by means of the photoelastic constant $f\sigma$.

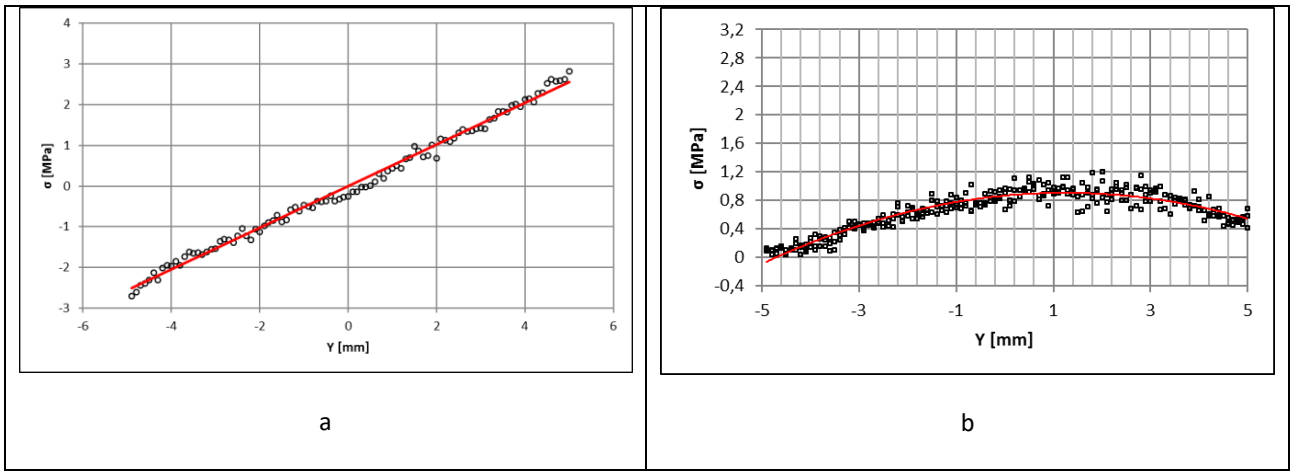

Fig. 4. 23 The reconstructed induced stress in (a). By the evaluation of the evaluation of the residual stress condition has been achieved (b).

In the case, the calculated photoelastic constant $f\sigma = 0.118$ MPa^{-1} has resulted to be compatible to what was evaluated in a previous works for similar (in dimension) PWO crystals observed by a plane polariscope with diffuse light in [32].

4.5.2 Observing orthogonally to the optic axis: experimental test

By Laser Conoscopy technique, a grid of points (about 20X20), with a resolution of 1 mm, has been inspected on a pre-series PWO sample, orthogonally with respect to the optical axis.
The sample presents a general bad quality by a visual inspection; scratches and chipping are recognizable on the surface and the geometry is not a regular cylinder (Fig. 4.24).

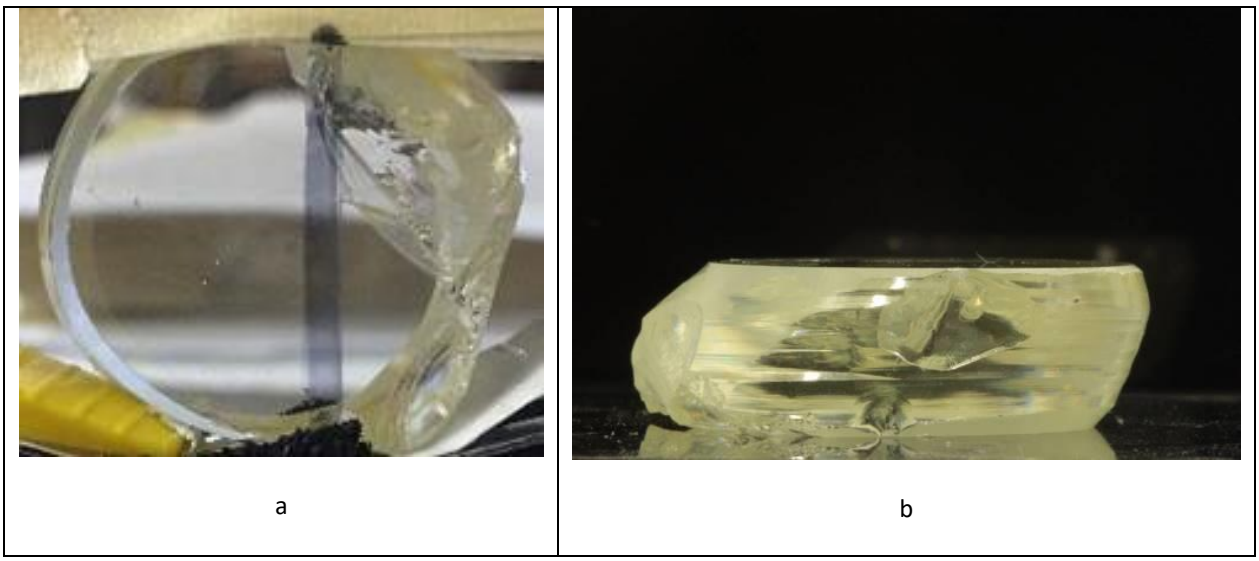

Fig. 4. 24 Pictures of the inspected PWO sample are shown in the figures. In (a) the chipping and scratches are evident on the surface. (b) the lateral prospective shows the shear of the sample which deviates from a classical cylinder, probably due to non-correct growth parameters which has generated the sliding phenomenon. A complex distribution of the residual stress is expected.

Not a homogenous state is expected but rather a complex distribution of stress and defectiveness.
Point by point, the fringe pattern has been carried out and the difference $R=\Delta y-\Delta z$ evaluated so to achieve a map of the stress trend over the crystal.
In Fig. 4.25, are reported the pattern from three different points along the crystal diameter. In those images, the variation of the distances Δy and Δz is clear and indicated by the green lines (Fig. 4.25).

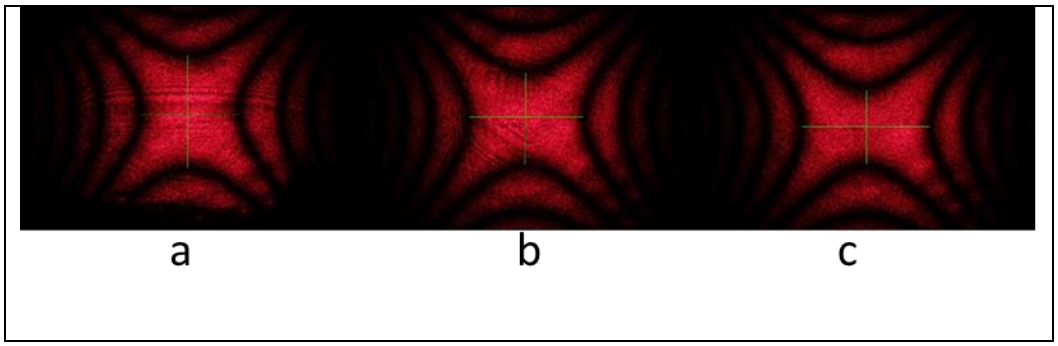

Fig. 4. 25 the images (a), (b) and (c) are fringe patterns acquired in different points on the sample diameter. (a) is due to the left boarder, (b) about in the center and (c) on the right boarder. The green lines highlight the variation of the distances Δy and Δz due to a different condition of the inspected points.

The distances between the tip of the hyperboles branches are, finally, evaluated so to get the difference R =Δy-Δz.
In Fig. 4.26, the map of the results is superimposed to the crystal geometry so to relate the residual stress trend to the sample.
The stress gradient seems to have a preferential direction along the sliding direction of the crystal (the direction along which the sample deviate from a cylinder shape).
Moreover, it is possible to notice that the faster gradient is close to the higher defectiveness area of the sample (Fig. 4.26).

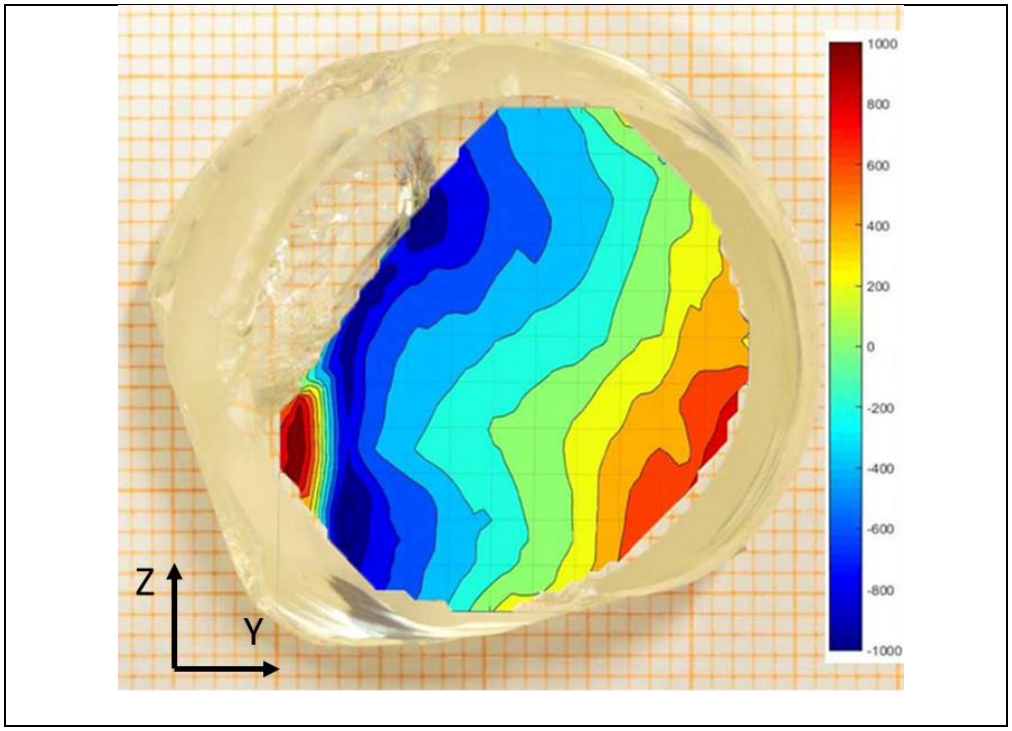

Fig. 4. 26 The map of the distribution of the difference R is superimposed to the sample. It is possible to notice that the faster gradient of colors is close to the area with a great defectiveness and seems to have a preferential direction compatible with the scrolling direction of the crystal geometry. It is worth to remark that in homogenous condition a monochromatic map is expected.

Even though, a calibration is needed to have the quantitative value of the stress in each point inspected, the map carried out in the test is well representative of the crystal state and stress distribution. In fact, a monochromatic map is expected in case of absence of residual stress and defectiveness.

4.5.3 Sphenoscopy: testing the technique

On the same sample of section 4.5.1, tests have been carried out by using the Sphenoscopic method.
The height has been inspected in one acquisition, the slight curvature of the fringe orders in the pattern confirms the residual stress distribution evaluated in the section 4.5.1 (Fig. 4.27) and (Fig. 4.23b).

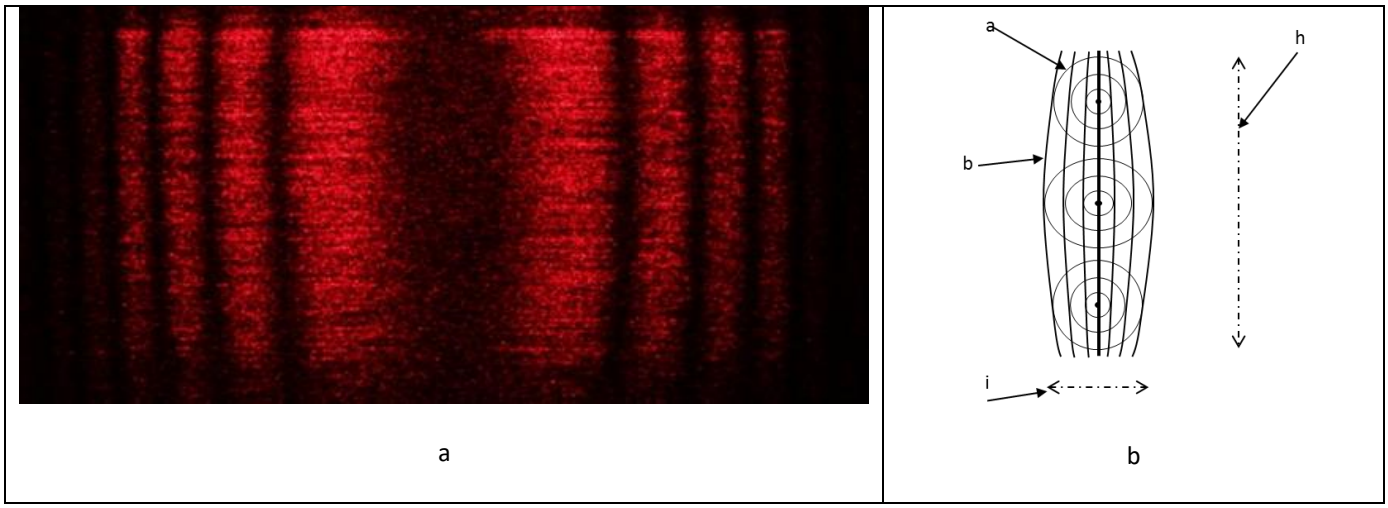

Fig. 4. 27 (left image) The fringe pattern carried out by Sphenoscopy along the height of the PWO sample in the middle area in unloaded condition. (right image) is the relative schematic representation of the pattern (b in the figure) which is the envelope of the diametric dimension (i) of the conoscopic fringe orders (a) in the same area. The slight curvature of the pattern confirms the residual stress state previously detected.

In the Fig. 4.27 the pattern is reported with a schematic representation of the fringes obtained, which are the envelope of the diametric dimension of the conoscopic on the axis pattern [35].
In the image in Fig. 4.27 the thicker central black fringe represents the trace of the optic axis (melatopes) along the height of the sample.
In the same position, the fringe pattern has been acquired while the sample was in bending condition by means of the four points bending test (Fig. 4.28a). The results are completely interpretable by the developed model represented in Fig. 4.28b [38].

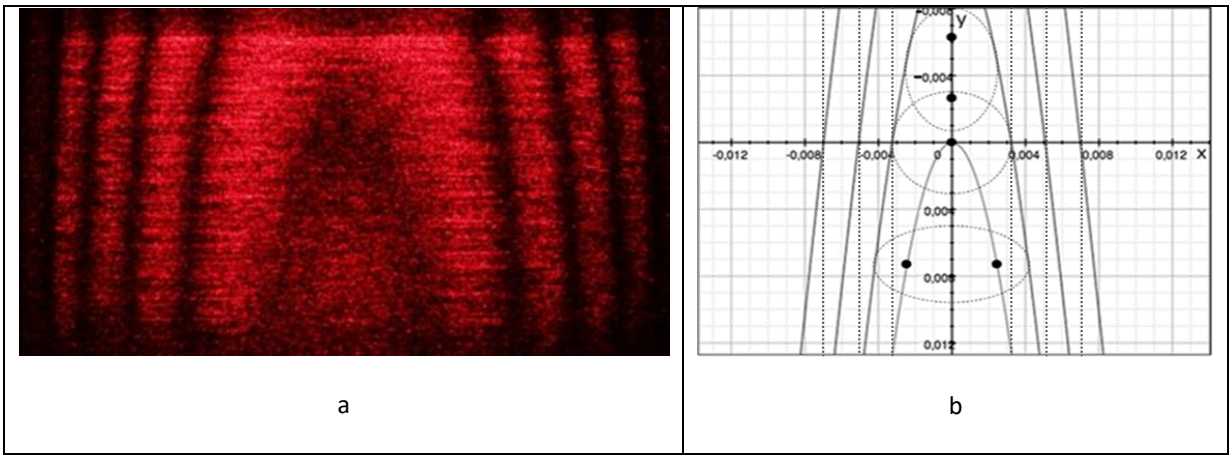

Fig. 4. 28 In the same area of the PWO sample, the fringe pattern has been acquired in bending condition (a). In (b) the result of the mathematical model in which the optic axes and their trace are represented. It is clear, from both the images, that the trace of the optic axis is clearly visible in the tensile area (bottom side) since the β angle opens in the plane of the load; while, the trace disappears in the compressive area (top side) since the optic axes open in the orthogonal plane with respect to the direction of the compressive load.

The image confirms that: while in the tensile area the optic axes open along the direction of the load; in the compressive area, they open in orthogonal direction. In fact, in the bottom side of the pattern in Fig. 4.28 (tensile area) the traces of the optic axes are clearly recognizable (the thicker black curve) while they are not present in the top side (compressive area).
The model representing the above behavior has been presented in [40], here are reported some steps.
Since n_o variates linearly with the stress, by the relation in (eq. 2.33) the angle β will variate as well as:

$$\mathrm{tg}^2\beta = \frac{n_0^{\,2} - (n_o + ky)^2}{(1 - \frac{n_o^{\,2}}{n_e^{\,2}})(n_0 + ky)^2} \qquad \text{(eq. 4.18)}$$

With k linearly dependent by the σ_x load.
the equation 4.16 is reported hereafter but this time the semi-angle β is a function of y:

$$H^2(n_x)N^2(x^2 + d^2)(1 + tg^2\beta(y))^2 = (x^2 - d^2tg^2\beta(y))^2$$

In particular, the trace of the optic axes (N=0) can be describe by [40]:

$$x^2 = d^2tg^2\beta. \qquad \text{(eq. 4.19)}$$

4.5.3.1 Observing along a random direction

Some observations have been carried out along a random position with respect to the optic axis comparing the fringe pattern acquired by the conoscopic technique with the pattern acquired with the sphenoscopic method (Fig. 4.29) [35].

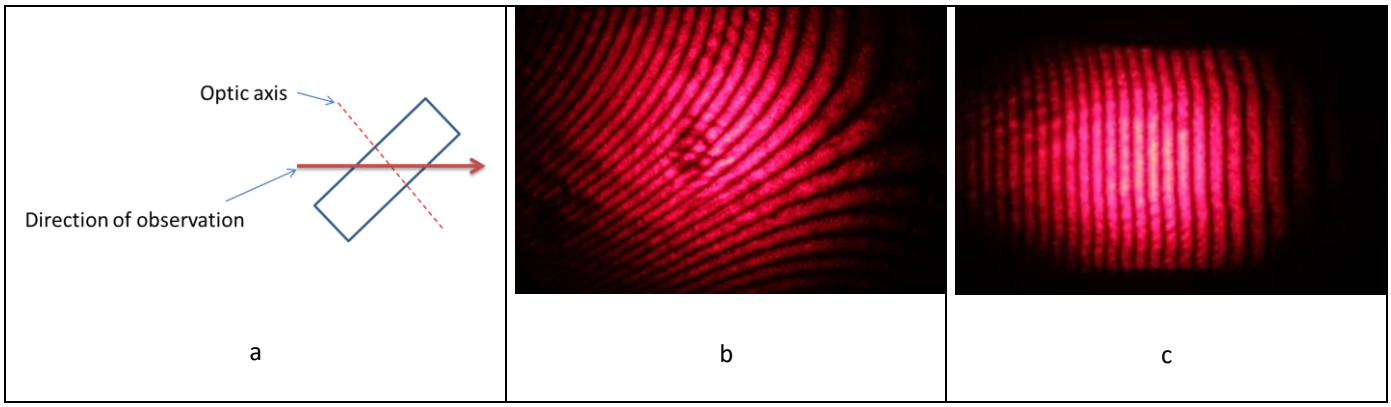

Fig. 4. 29 A scheme of the observation in a random position with respect to the optic axis (a). In (b) the fringe pattern carried out by pointwise conoscopy. (c) is the Sphenoscopic pattern due to the same direction. While the conscopic pattern (b) is not easy to interpret, by the sphenoscopic lines (c) a simplified analysis is possible. In fact, the slight curvature close to the edges confirms the presence of the residual stress.

In the image (Fig. 4.29b) the conoscopic pattern, due to a pointwise inspection, is reported, which is more complex to interpret with respect to the Sphenoscopic one (Fig. 4.29c) which covers the entire height of the sample.
The easily interpretation of the sphenoscopic pattern leads to the confirmation of the residual stress state of the sample, by the slight curvature of the lines mostly at the boarders.

4.5.3.2 Inspection of a non-homogenous sample

The last test has been carried out on a bad quality sample previously evaluated in [41]. In the Fig. 4.30 a picture of the sample is reported with the relative sphenoscopic pattern.

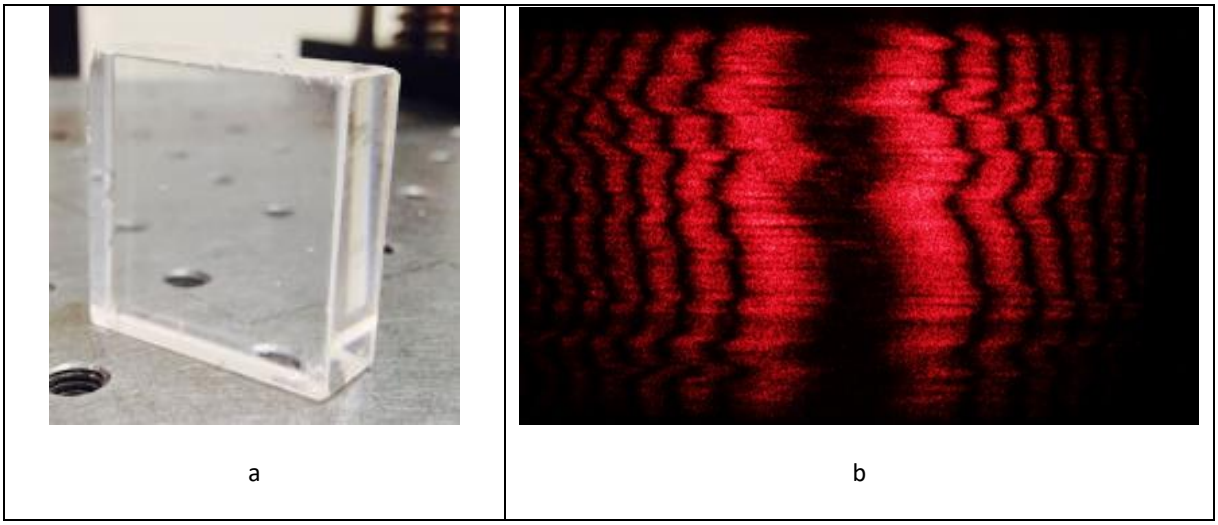

Fig. 4. 30 the picture of the bad quality sample measured in [39] (a) and the relative sphenoscopic pattern (b) carried out along the sample height. The pattern presents highly distorted fringes due to a non-homogenous position of the optic axis along the height confirming the low quality of the sample probably due to non-correct growth parameters.

That pattern presents highly distorted fringes due to a rotation of the optic axis along the sample height rather than a stress distribution. In fact, each fringe order distorts accordingly with the optic axis trace.

The shenoscopic technique has shown reliability and sensitivity to the structural and stress condition of the birefringent media.
It provides a simple pattern to interpret and has fasten the inspection (e.g. to inspect a squared sample NxN conoscopic images are need while in Sphenoscopy N+N are enough, see chapter 5 section 5.3) [40].
Moreover, since the light wedge is continuous over its eight, the spatial resolution, along that direction, is determined mainly by the acquisition system (the camera lens and its sensor resolution)
Sphenoscopy does not substitute the laser Conoscopy but it is suitable for a fast, less detailed but reliable analysis (see chapter 5 section 5.3).

Chapter 5

5 Impact

The research program has been developed in an international framework. The Polytechnic University of Marche (Università Politecnica delle Marche) is involved in collaborations like the "Crystal Clear Collaboration" and the COST ACTION TD 1401 "FAST" coordinated by the CERN. During the research period, strong collaboration with companies (e.g. Saint Gobain, Crytur) has been held. This gave the opportunity to test the developed techniques in different environment, from research institutes to the industries; giving the possibility to evaluate the impact of the methods out from the University Laboratories.
Here the result of some activities carried out in different structures are reported.

5.1 CERN experience

Benches have been arranged to assess crystal samples conditions and correlate the results with the lightning performances of the inspected samples.
The presence of stress/strain/defects/inclusions etc. can affect performance of the scintillator in terms of light yield and time of flight within the crystal bulk or fiber. The activity moved a step in testing the influence of the strain/stress and the general conditions of the crystals (e.g. orientation of the optic indicatrix) on the functional optical properties of the scintillating material like time transport of light.
In the Fig. 5.1, the picture of some of the arranged test bench is shown.

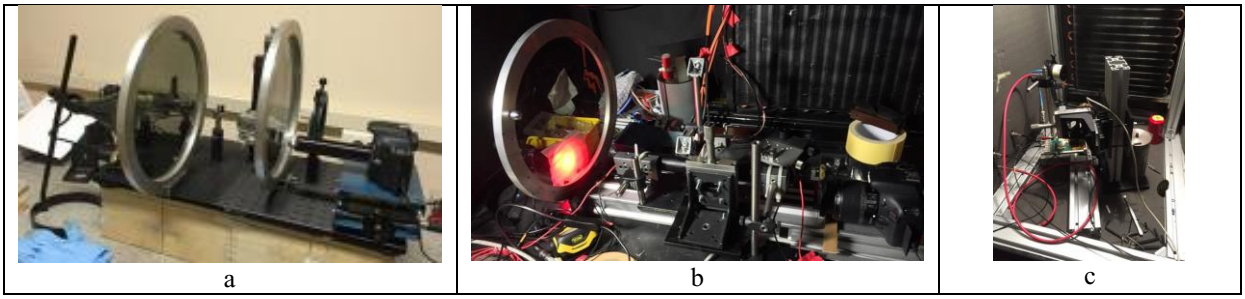

Fig. 5. 1 The figure shows in (a) the photoelastic set-up arranged to observe the crystals. (b) and (c) are typical test bench to measure the lightning performances: (b) attenuation length test bench and (c) decay time test bench. They have been provided with a load devices to measure the samples in compressed condition.

5.1.1 Interesting Results

Bulk sample of LSO and pixel sample of LYSO have been inspected with Laser Conoscopy so to evaluate their conditions.
The LSO samples have been inspected point by point evaluating the stress state and the optical orientation (the orientation of the optical indicatrix with respect to the geometry).
In some samples the pattern carried out by each point does not present distortion but the fringes change position from point to point (Fig.5.2).
This leads to a rotation of the optical indicatrix along the crystal length due to a rotation of the lattice (Fig. 5.2).
It is worth to remark that it is not possible to achieve such details by the diffuse light polariscope.

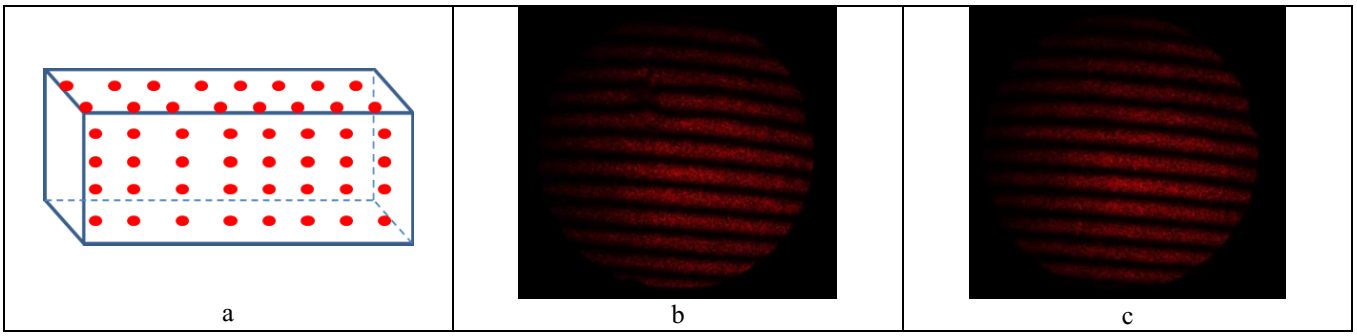

Fig. 5. 2 In (a) a schematic representation of the inspected points over the samples. (b) and (c) are the fringe pattern of two points in the same line. From (b) to (c) the pattern moves (it is easily noticeable looking at the bottom of the two images). This is due to a rotation of the optical indicatrix along the line, which depends by a non-homogenous lattice orientation over the sample.

In [42] the timing performances of two samples have been measured. In the Fig. 5.3 the results are summarized. The samples are from the same produced and should be the same in terms of structures and performances. In the Fig. 5.3 they have some slight differences, as can be shown.

Sample	Rise	Decay 1	Decay 2	CTR(Rho.)	CTR(no grease)	CTR(Meltm.)
CPI 2554	58 ± 20 [ps]	45,4 ± 3 [ns]	23,6 ± 3 [ns]	152,8 ± 2 [ps]	219,0 ± 4 [ps]	136,4 ± 2 [ps]
CPI 2745	60 ± 20 [ps]	41,5 ± 3 [ns]	-	159,1 ± 2 [ps]	230,5 ± 4 [ps]	143,0 ± 2 [ps]

Fig. 5. 3 results from the paper [40]. Even if the samples should be theoretically identical they have a slight difference in their timing performances.

The same samples have been inspected by Laser Conoscopy. In the Fig. 5.4 the acquired fringe patterns are reported. The inspection has been carried out with the same orientation with respect to the surfaces, this leads to the results of a strong difference in terms of the optical orientation between the samples (Fig. 5.4c and Fig. 5.4d).

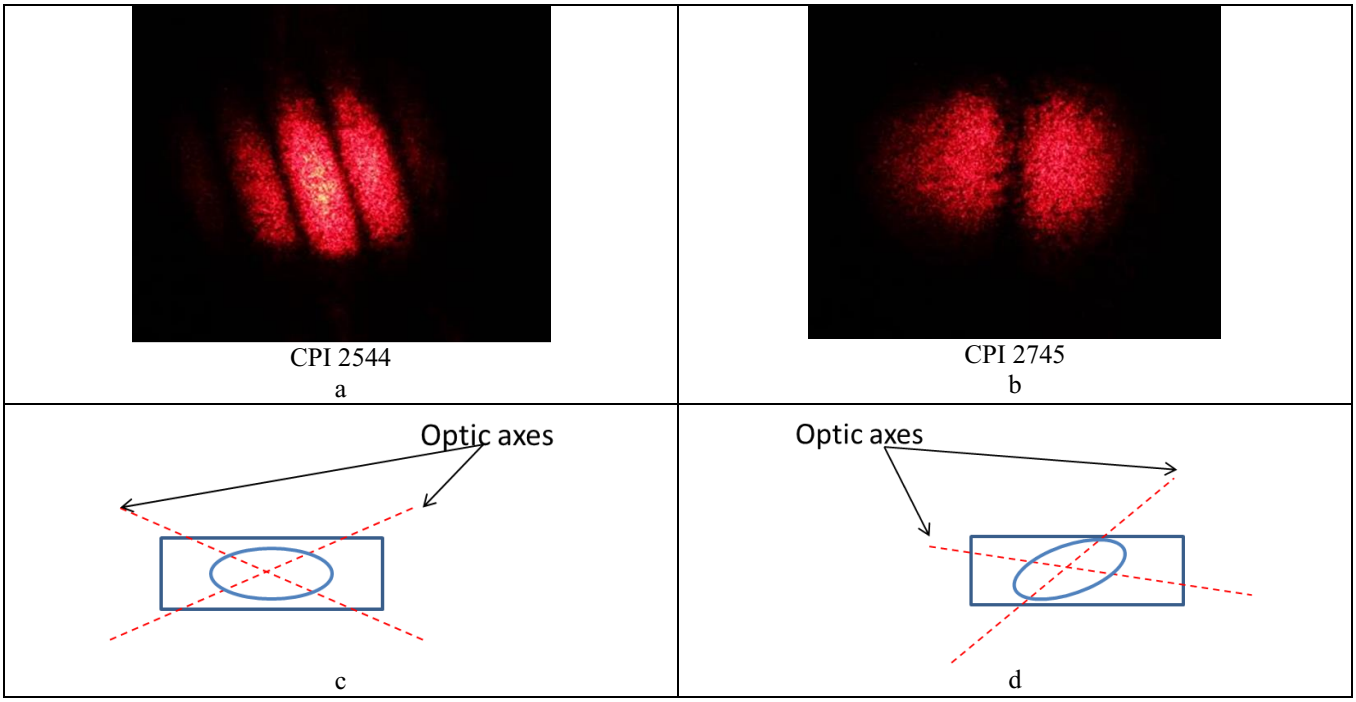

Fig. 5. 4 The fringe patterns of the LYSO samples, carried out by the same side and in the same direction (a) and (b). The patterns indicate that the samples have a different orientation of the optic indicatrix with respect to their geometry, as it is schematically reported in (c) and (d).

Both the results are interesting and push the research forward. With non-invasive tools information about structural condition of the samples have been achieved.
In the first case, the LSO samples, it would be useful to understand the reasons of the rotation of the optical indicatrix and investigate if such non-homogeneous condition can affect the performance of the scintillator.
By the results carried out from the investigation of the CPI LYSO samples, a correlation between timing performances and optical orientation seems to rise. This sounds reasonable since the optical indicatrix is related to the ray velocity surfaces. A deeper investigation is mandatory in order to asses this possible correlation (e.g. study a statistical reasonable number of samples with different optical orientation). On this item the work is in progress.
The developed tools have shown to be helpful for the purpose of checking the crystal conditions.

5.2 Saint Gobain Recherche: technological transfer

By the need of an efficient production and high quality end product, industries have prompt and stimulated part of this research.
The developed methods and techniques are suitable tools for a non-invasive quality control of the entire production giving feedbacks to properly set the growth parameters and the machining strategies.
Under the collaboration between Polytechnic University of Marche and Saint Gobain Recherche, a quality control system has been developed, based on the results of this research, which is still working in the Saint Gobain laboratories.
In Fig. 5.5 some pictures of the test bench are reported with some inspection results.

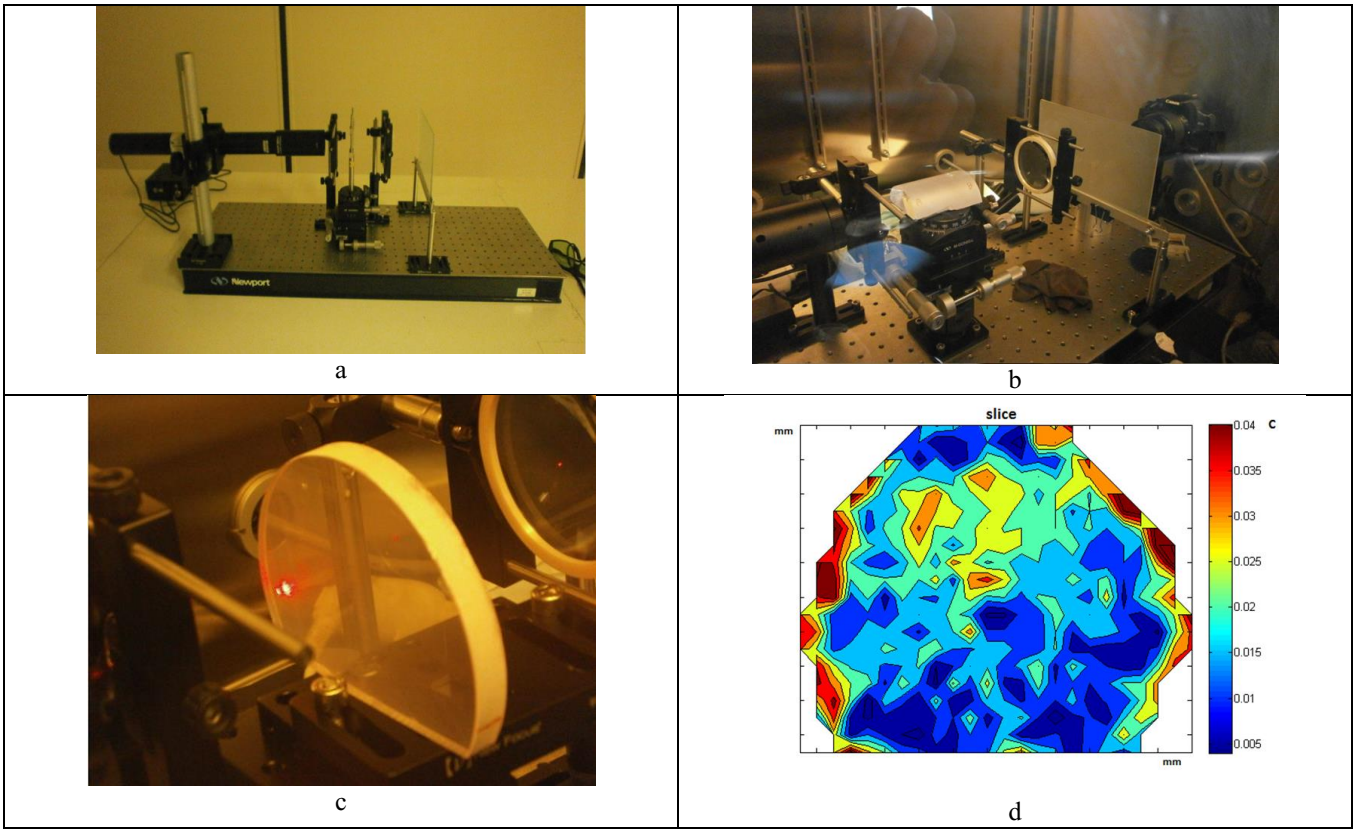

Fig. 5. 5 In the images (a) and (b) some pictures of the test bench, under construction and testing (a) and during function in the glovebox (b), are reported. In (c) a slice sample under inspection with the related results (d). The latter image (d) is a map of the residual stress distribution of the sample in (c). The high residual stress magnitude at the border, highlights how the surface finishing procedure affects the crystal condition.

A typical procedure, in industry, is to submit the samples to trial tests like thermal or vibration shocks especially if the crystals have to be installed in systems which work in critical condition. Without a residual stress evaluation, the above tests (and the functional conditions) could result destructive for these brittle materials.
The techniques presented in this thesis find place in this phase, providing a non-destructive and cost effective evaluation of crystal state in order to avoid spontaneous fractures and malfunctions under working conditions.

5.3 Testing PWO: Crytur experience

Actually, part of this experience has been described in chapter 4, the PWO sample of the section 4.2. has been kindly provided by the CRYTUR company.
The collaboration has been aimed to a quality control of the PWO production. The sample has been provided to tests the feasibility and the reliability of the developed techniques.
The PWO crystal has been inspected by the Laser Conoscopic technique and by Sphenoscopy. The fringe patterns detected by Sphenoscopy are shown in Fig 5.6.

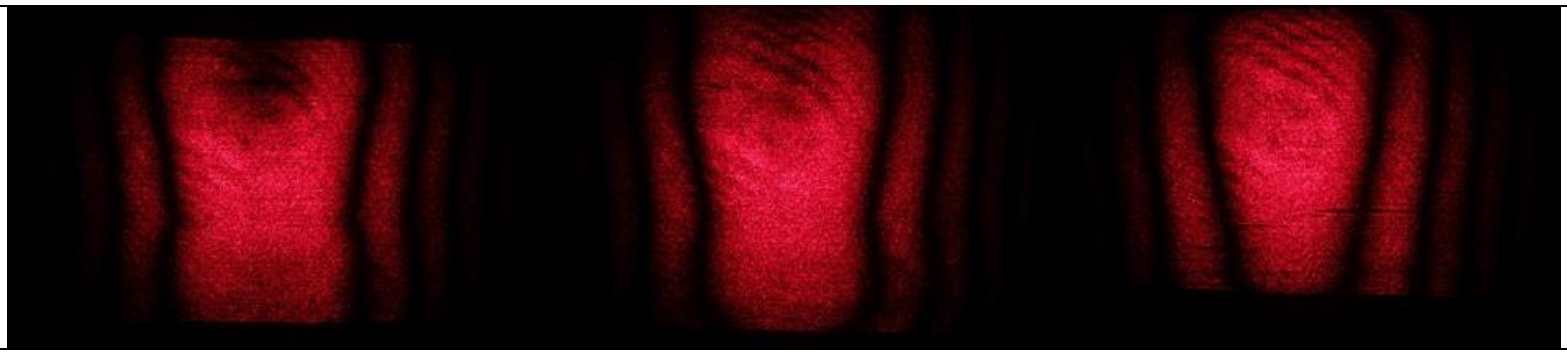

Fig. 5. 6 Sphenoscopic fringe pattern carried out on the sample: left boarder (left), central area (center) and by the right boarder (right). The changing in terms of stress and defect distribution is revealed by the curvature and the variation of the distance between the fringes.

Fig. 5.7 reports the sphenoscopic pattern compared with the relative conoscopic images from which, the pattern shape derives. The virtual grid observed, by Conoscopy, over the sample, has about 20x20 points (1 point per millimeter). The results are reported in Fig. 4.26 and in Fig. 5.8 (left).

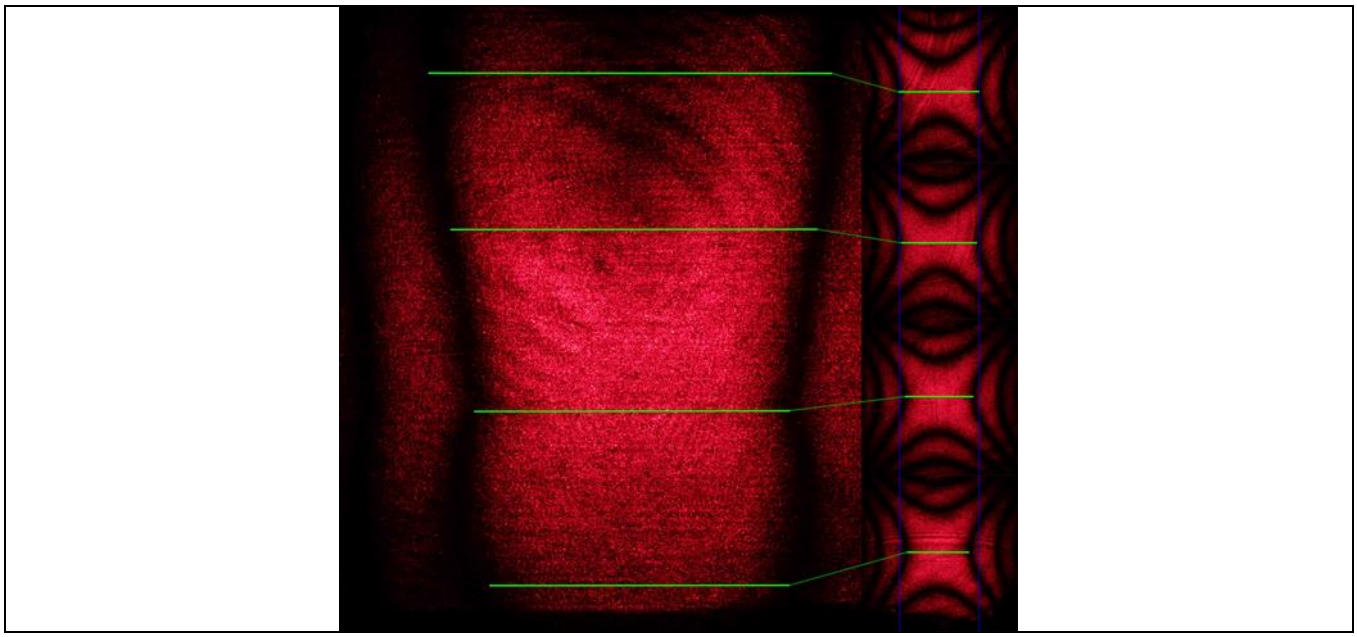

Fig. 5. 7 Sphenoscopic fringe pattern compared with the relative conoscopic pattern. The sphenoscopic one is the envelope of one dimension of the conscopic figures. 20 conoscopic acquisitions have been needed to cover the same area of one sphenoscopic inspection.

The results carried out by Sphenoscopy are reported in Fig. 5.8 (right). The same trend of the conoscopic inspection is detected.
The sphenoscopic map is indeed less detailed but provides reliable results by analyzing 20 + 20 images instead of 20x20.

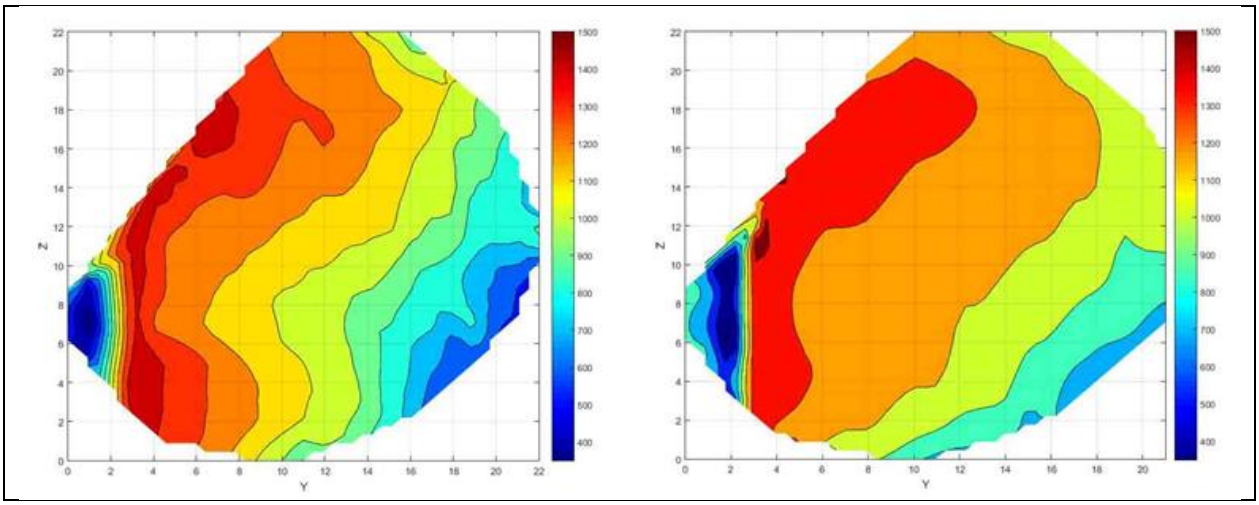

Fig. 5. 8 The map of the conoscopic results (left) and the one carried out by Sphenoscopy (right). Even if the sphenoscopy one is less detailed, reliable results are achieved. The map (right) is compatible with the conoscopy map but carried out by a faster inspection: while, by conoscopy, 20x20 images have to be acquired and inspected, by sphenoscopy, the number decreases to 20+20.

In pre-series phase, a great effort has to be provided so to set properly each parameter of the entire production process. This will ensure a good quality of the product with predictable behavior. Therefore, inspections and investigations are mandatory in order to have useful feedback for the purpose.
Flexible tools are preferred by the industries to meet the needs of the different cases which occur during the development and production of a material.
The two techniques, Laser Conoscopy and Sphenoscopy (both carried out observing along the *a* crystallographic axis), have given results compatible with the crystal conditions (in Fig. 4.24). In fact, the stress trend follows direction of the sliding phenomenon and the quicker gradient are located close to the area with high defectiveness. Therefore, those data are exploitable to tune the production process parameters.
The choice of one technique rather than the other depends by the balance between details and time which is suitable to the user needs. Even though, conoscopy offers more details in the analysis, the results carried out by Shenoscopy are more than compatible with them.

Chapter 6

6 Concluding Remarks

6.1 Conclusions

Since birefringent crystalline materials have crucial roles in numbers of fields demanding high performances, durability and acceptable cost, an effort in the theoretical knowledge is mandatory. Moreover, reliable and precise instruments and methods are required by researchers, users and producers to achieve deeper knowledge of the material and its state and to get feedback so as to improve the efficiency of the production system and the quality of the end-product.

The residual stress is indeed an indicator of the crystal quality and it is a critical quantity to be monitored and kept under control for an optimal production (growth and machining); furthermore, it is strictly related to the durability and to the functional behavior (light production and transport).

Therefore, in this work, non-invasive techniques have been developed and validated for the assessment of the residual stress conditions of the birefringent transparent material. Metrologic performance as well as reliability and accuracy of the developed methods have been validated by experimental tests.
The methods developed are based on the photoelastic behavior of the birefringent material and the Conoscopy which belongs to the optical crystallography background.

The development of a laser Conoscopy, has overcome the limitations about the sensitivity and the spatial resolution of the classical diffuse light polariscope technique.
The method gives the possibility to control the conic probe volume confining the light in a precise part of the crystal volume with known dimensions.
Since the fringe pattern is due uniquely by the probed volume, the sensitivity and the spatial resolution are enhanced as the volume is reduced. Extremely detailed information about the crystal state can be achieved by the developed technique even if the measurement environment is more critical; the condition of the samples surfaces and the quality of the optics highly affect the quality of the fringe images patterns acquired.
Tests, carried out on a uniaxial crystal, have validated the reliability and the accuracy of the pointwise methodology.

By the same method, the possibility to have a complete characterization have been improved measuring in different directions with respect to the optic axis or the bisector of the optic axes. In fact, by inspecting the uniaxial crystal orthogonally to the bisector of the optic axes, different fringe patterns are acquired not yet extensively studied in literature at our best knowledge. A measurable quantity has been determined by the mathematical model, which gives an indication of the variation of the stress state over the crystal in a reliable way.

Precise algorithms have been developed dedicated to the analysis of the fringe patterns acquired; a great effort has been placed in this development to reduce the increased noise of the fringe images.

The set of developed methods is completed by a new technique named Sphenoscopy, which provides reliable inspection of the crystal in a faster and simplified way whatever orientation of the crystallographic and optic axes.
This technique is a modified conoscopy, which makes use of a wedge-shaped probe volume instead of the conic one.
That volume inspects a larger zone with respect to the pointwise conoscopy and allows to inspect stress state along a line, rather than at a single point. The technique has been tested and compared with the conoscopy; the results are less detailed than the conoscopic one but compatible and still reliable, suitable for a fast inspection. All these activities are based on a strong theoretical approach that has led to a development as well to the modeling of the phenomena.

The impact of the developed techniques has resulted to be interesting by the number of activities in which they have been involved in different environments, both research and industry.

The methods have been exploited in the CERN laboratories and by industries like Saint Gobain Recherche (F) and for analysis of Crytur (CZ) samples.

6.2 Future improvements and potential development

The proposed methods are susceptible of improvements.
The observation along the orthogonal position with respect to the optic axis (or the bisector of the optic axes) needs a deeper understanding of the piezo-optic behavior, developing and improving the predictive models.
In this sense samples with suitable geometries and optic orientation would help to arrange dedicated tests so to achieve a complete characterization of the piezo-optic properties.
Different shape and dimensions (bulk, pixels, prismatic and cylindrical fibers also with sub millimetric section) of the crystalline birefringent materials are requested by the applications; suitable techniques for the purpose of the characterization are under developement. E.g. the photoelastic index matching techniques and scattered light methods are promising in order to accomplish to these needs.
From the image processing point of view, the existing tools have to be optimized to become suitable for an accurate and comfortable analysis of the images carried out by the developed techniques (in particular for the sphenoscopy and the observation orthogonal to the optic axis).
In conjuction with the optical methods, ultrasound techniques are good candidates not only for a complete structural characterization but also to intervene on the crystal function properties (e.g. the radiation hardness recovery).
In this direction, some tests have been already carried out and are still ongoing.

References

[1]. P. Lecoq, A. Annenkov, A. Gektin, M. Korzhik, C. Pedrini, Inorganic Scintillators for Detector Systems, Physical Principles and Crystal Engineering, Series: Particle Acceleration and Detection, XII, 2006, ISBN 978-3-540-27768-2

[2]. Lecoq P. et al. (2006).Inorganic Scintillators for Detector Systems. ISBN-10 3-540-27766-8 Springer Berlin Heidelberg New York.

[3]. G. Schwarz and A. J. Bearden, "Scintillation crystals," Am. J. Phys. 34, iii (1966).

[4]. D. Rinaldi, M. Lebeau, N. Paone, L. Scalise, and P. Pietroni, "Quality control and characterization of scintillating crystals for high energy physics and medical applications," in Wide Spectra of Quality Control, edited by I. Akyar (InTec, 2011), ISBN: 978-953-307-683-6, available from: http://www.intechopen.com/books/wide-spectra-of-quality-control/quality-control-and-characterization-of-scintillating-crystals-for-high-ener gy-physics-and-medical-a.

[5]. W.Bradsley, D.T.J. Hurle, Crystal growth: a tutorial approach, J.B. Mullin (eds.) North-Holland Publishing Company, 1979

[6]. C.L.Melcher, J.S.Schweitzer, C.A.Peterson, R.A.Manente, H.Suzuki,Schlumberger-Doll Research, Ridgefield, CT06877-41018,USA, Crystal growth and scintillation properties of the rare earth oxyoorthosilicates.

[7]. CMS -The Electromagnetic Calorimeter Project, Technical Design Report, CERN/LHCC 97-33 (15 December 1997)

[8]. M. Nikl, "Scintillation detectors for x-rays," Meas. Sci. Technol. 17, R37 (2006)

[9]. Thomas F. Budinger, Instrumentation, Positron-Emission Thomography (PET)

[10]. Ziad Nahas, Mark S. George, Jeff P. Lorberbaum, S. Craig Risch, Kenneth M.Spicer, SPECT and PET in Neuropsychiatry

[11]. Dally J. W., Riley W. F., Experimental Stress Analysis, 2nd edition, McGraw-Hill Book Company, Singapore, 1987

[12]. H. Aben, J. Anton, and A. Errapart, "Modern photoelasticity for residual stress measurement in glass," Strain 44(1), 40–48 (2008).

[13]. Walhstrom E.E., Optical Crystallography, Wiley, New York, 1960

[14]. Wood E. A., Crystal And Light, Van Nostrand Company, New Jersey, 1964

[15]. J. F. Nye, Physical Properties of Crystals, Clarendon Press, Oxford (1985).

[16]. Y. I. Sirotin and M. P. Shaskolskaya, Fundamentals of Crystal Physics, Mir Publishers, Moscow (1982)

[17]. Born M., Wolf E., Principles Of Optics, 6th edition, Pergamon press, New York, 1975

[18]. J. A. Haigh, Y. Kinebas, and A. J. Ramsay, Applied Optics 53, 2, 184 (2014), Inverse conoscopy: a method to measure polarization using patterns generated by a single birefringent crystal

[19]. T. Y. Chen and C. E. Taylor, "Computerized fringe analysis in photomechanics," Exp. Mech. 29(3), 323–329 (1989).

[20]. Rinaldi, D., Pietroni, P., Daví, F.: Isochromate fringes simulation by Cassini-like curves for photoelastic analysis of birefringent crystals. Nucl. Instrum. Methods Phys. Res., Sect. A, Accel. Spectrom. Detect. Assoc. Equip. 603, 294–300 (2009)

[21]. Caciuffo, R., Melone, S., Fisica generale II volume, ottica ed elettromagnetismo, Masson 1996

[22]. Khorasani, S., Rashidian, B., Energy approach to the propagation of light waves in anisotropic crystals, SPIE Conference on Design, Fabrication and Characterization of Photonic Davices, Singapore 1999- SPIE vol. 3896
[23]. N.V. Perelomova, M.M. Tagieva, Problems in crystal physics with solutions, Edited by M.P. Shaskol'skaya translated from the Russian by V.I. Kisin, Mir Publisher Moscow, pag. 115-135,.pag.170-179, pag.304-329.
[24]. Wood E. A., Crystal and Light, Van Nostrand Company, New Jersey, 1964
[25]. P.A. Bertin, Memoire sur la surface isocromatique, Theorie generale des franges des lames cristallisees, Annales de Chimie et de Physique [3eme serie] LXIII (1861), 57-92
[26]. F. Davì, Journal of the Optical Society of America A 32(12):2323-2337 · December 2015
[27]. F. Davì and D. Rinaldi, "Mechanical and optical properties of anisotropic single-crystal prisms," J. Elasticity 120(2), 197–224 (2015)
[28]. K. Ramesh, Digital Photoelasticity—Advanced Techniques and Applications, Springer-Verlag, Heidelberg, New York, Tokyo (2000)
[29]. J. E. Shigley, C. R. Mischke, and R. G. Budynas, Mechanical Engineering Design (McGraw-Hill, New York, 2004), ISBN 0-07-252036-
[30]. A. S. Jayatilaka, Fracture of Engineering Brittle Materials (Applied Science Publishers, 1979).
[31]. Cocozzella N., Lebeau M., Majni G., Paone N., Rinaldi D. (2001). Quality inspection of anisotropic scintillating lead tungstate (PbWO4) crystals through measurement of interferometric fringe pattern parameters. Nuclear Instruments and Methods in Physics Research Section A (NIM A) 469 3 pp.331-339A.
[32]. Ciriaco, F. Davì, M. Lebeau, G. Majni, N. Paone, P. Pietroni, and D. Rinaldi, "PWO photo-elastic parameter calibration by laser-based polariscope," Nucl. Instrum. Methods Phys. Res., Sect. A 570, 55–60 (2007).
[33]. L. Montalto, N. Paone, D. Rinaldi, and L. Scalise, "Inspection of birefringent media by photoelasticity: From diffuse light polariscope to laser conoscopic technique," Opt. Eng. 54(8), 081210 (2015)
[34]. L. Montalto, N. Paone, L. Scalise, and D. Rinaldi, "A photoelastic measurement system for residual stress analysis in scintillating crystals by conoscopic imaging," Rev. Sci. Instrum. 86, 063102 (2015).
[35]. L.Montalto, D.Rinaldi, L.Scalise, N.Paone1 F.Davì, "From Conoscopy to Sphenoscopy: new experimental methods in crystals inspections" FOTONICA 2016 18° Convegno Nazionale sulle Tecnologie Fotoniche Roma, 6-8 giugno 2016
[36]. Pier Paolo Natali, Luigi Montalto, Fabrizio Davì, Nicola Paone, Daniele Rinaldi, Lorenzo Scalise, Optimization of the photoelastic parameters for the stress evaluation in scintillating anisotropic media, International instrumentation and measurement technologies conference 2017, submitted.
[37]. Parker, J.R., Algorithms for image processing and computer vision
[38]. Imaq Vision Concepts Manual, National Instruments
[39]. Doeblin, E., Measurement system: application and design, ed Mc Graw Hill.
[40]. L. Montalto, D. Rinaldi, L. Scalise, N. Paone, and F. Davì, Photoelastic sphenoscopic analysis of crystals, Review of Scientific Instruments 87, 015113 (2016); doi: 10.1063/1.4940196D
[41]. D. Rinaldi, A. Ciriaco, M. Lebeau, N. Paone, Quality control on pre-serial Bridgman production of PbWO4 scintillating crystals by means of photoelasticity, Nuclear Instruments and Methods in Physics Research A615(2010)254–258
[42]. Stefan Gundacker, Etiennette Auffray, Kristof Pauwels, Paul Lecoq, Measurement of intrinsic rise times for various L(Y)SO and LuAG scintillators with a general study of prompt photons to achieve 10

ps in TOF-PET, Physics in Medicine and Biology 61(7):2802-2837 · April 2016 DOI: 10.1088/0031-9155/61/7/2802

Acknowledgments

This work was not possible without the effort of special people which have contributed in different way to achieve the results.

Thanks to Prof. Nicola Paone, Prof. Daniele Rinaldi and Dr. Paul Lecoq for the possibility they gave to me to improve myself and for believing in the ideas.

Prof. Fabrizio Davì and Prof. Lorenzo Scalise for the continuous support.

Acknowledgments go to the Mechanical and Thermal Measurements group and to the Experimental Physics group of Università Politecnica delle Marche for the nice and fruitful working environment.

I think I will never forget Giampiero, Claudio, Antonio, Bud, Lorenzo, Federico, Barbara, Giuseppe, Pier Paolo, Alfonso and Edoardo, always close to me.

This work has been carried out in the Crystal Clear Collaboration and take part in the COST ACTION FAST TD1401, this has given me the opportunity to meet people who have enlarged my knowledge and improved my professional and personal experience.
Thanks to Prof. Loudos, Prof. Ziemons. Prof. Tsoumpas and Dr. Etiennette Auffray for the attention, the support and the kind collaboration.

Special thanks to the CERN people: thanks to Marco L., Marco P., Matteo, Gianluca and Kristof.

My Mom and Dad and my family always strong, thank you.